

FACILITY FORM 802

N71-16586  
(ACCESSION NUMBER)

(PAGES)

NASA CR-116247  
(NASA CR OR TMX OR AD NUMBER)

(THRU)

(CODE)

(CATEGORY)

# EXPERIMENTAL STUDY OF VISCOUS LOW-DENSITY NOZZLE FLOWS

Dietmar E. Rothe

**CAL No. AI-2590-A-2**

Prepared for:

HEADQUARTERS

NATIONAL AERONAUTICS AND SPACE ADMINISTRATION  
WASHINGTON, D.C.

PROGRAM MANAGER:

Frank E. Compitello

NASA HEADQUARTERS

FINAL REPORT

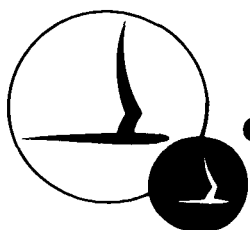
Contract No. NASW-1668

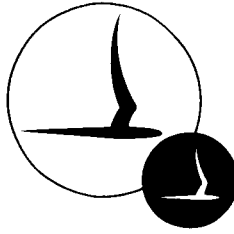
June 1970

## CASE FILE COPY

**CORNELL AERONAUTICAL LABORATORY, INC.**

OF CORNELL UNIVERSITY, BUFFALO, N. Y. 14221





CORNELL AERONAUTICAL LABORATORY, INC.  
BUFFALO, NEW YORK 14221

EXPERIMENTAL STUDY OF  
VISCOUS LOW-DENSITY  
NOZZLE FLOWS

FINAL REPORT  
CAL REPORT NO. AI-2590-A-2  
CONTRACT NO. NASW-1668  
JUNE 1970

Prepared for:  
HEADQUARTERS  
NATIONAL AERONAUTICS AND SPACE ADMINISTRATION  
WASHINGTON, D.C.

PROGRAM MANAGER: Frank E. Compitello  
NASA HEADQUARTERS

PREPARED BY:

*DE Rothe*

Dietmar E. Rothe

APPROVED BY:

*Charles E. Treanor*

Charles E. Treanor, Head  
Aerodynamic Research Department

## FOREWORD

The research reported herein constitutes an experimental follow-up to theoretical work performed in an earlier phase of the same research program sponsored by the NASA under Contract No. NASW-1668. The initial theoretical investigation was conducted by Dr. William J. Rae and has been reported in CAL Report No. AI-2590-A-1. Technical direction of this program was provided by Mr. Frank E. Compitello of NASA Headquarters.

Experiments described in this report were performed in a low-density flow facility which was designed, built and instrumented at the Cornell Aeronautical Laboratory in a separate internally funded project.

The contributions made by Drs. W. J. Rae and P. V. Marrone through informal discussions are gratefully acknowledged.

## ABSTRACT

Performance predictions for attitude control jets of satellites and manned spacecraft suffer from the lack of well-substantiated theoretical and experimental data in the fully viscous nozzle-flow regime. This paper presents an experimental investigation of the internal and external flow for nozzle Reynolds numbers in the general range between  $10^2$  and  $10^3$  with nitrogen as the test gas. Electron-beam techniques are used for measuring gas density and rotational temperatures at selected points throughout the flow. Discharge coefficients are also measured. In addition, some effects of ambient pressure on the external flow structure are studied by flow visualization experiments. At the lower Reynolds numbers studied, experimentally determined temperatures indicate the existence of a supersonic "bubble" inside the nozzle expansion-cone, with a subsequent shock-free viscous transition to subsonic flow. These results substantiate the theoretical prediction of this phenomenon, first made by Rae in an earlier phase of this program.



## TABLE OF CONTENTS

<u>Section</u>	<u>Page</u>
	ii
	iii
I	1
II	4
III	9
	9
	10
	12
	12
	14
	18
IV	22
	23
	25
	26
	28
	31
	35
V	37
	39
	43
	47
	85

## LIST OF TABLES AND ILLUSTRATIONS

<u>Table</u>		<u>Page</u>
1	Values of $\text{Log } 2K'G( \lambda_o/\lambda )^4$ for the R-Branch of the 0-0 Band of the First Negative System of $\text{N}_2^+$ . . . . .	43
2	Nozzle Geometry and Operating Conditions for Discharge Coefficients in Fig. 38 . . . . .	46
<u>Figure</u>		<u>Page</u>
1	Rotational Fine-Structure in the R-Branch of the 0-0 Band . . . . .	47
2	Semi-Log Plot of Normalized Line Intensities . . . . .	48
3	Low-Density Flow Facility with Electron Gun . . . . .	49
4	Low-Density Flow Facility . . . . .	50
5	Mass Flow Capability of Low-Density Tunnel for Nitrogen . . . . .	51
6	Outline of Experimental Arrangement . . . . .	52
7	Stagnation Chamber with Mounting Flange . . . . .	53
8	Optical Imaging and Scanning System (Inside View) . . . . .	54
9	Optical Imaging and Scanning System (Rear View) . . . . .	55
10	Low-Density Tunnel with Electron Gun and Optical Instrumentation . . . . .	56
11	Free Jet Plumes of Ar, He and $\text{CO}_2$ . . . . .	57
12	Nitrogen Free Jets . . . . .	58
13	Radial Density Profiles in Free Jet Plume . . . . .	59
14	Electron-Beam Measurements of Temperature and Density along Centerline of a Free Jet . . . . .	60
15	Graphite Nozzles . . . . .	61
16	Minimum Test Section Pressures for the Two Nozzles . . . . .	62
17	Photograph of Electron Beam Inside Nozzle . . . . .	63
18	Determination of Radial Density Profiles Inside Nozzle . . . . .	64
19	Measured Gas Temperatures along Nozzle Axis . . . . .	65
20	Centerline Temperature just Downstream of Nozzle Exit as a Function of Reynolds Number . . . . .	66

# LIST OF TABLES AND ILLUSTRATIONS (Cont'd)

<u>Figure</u>		<u>Page</u>
21	Centerline Densities at Maximum Nozzle Pressure Ratios. . . . .	67
22	Centerline Pressures Derived from Measured Densities and Temperatures . . . . .	68
23	Measured Radial Density Profiles in the 5mm Nozzle at B=110. . . . .	69
24	Measured Radial Density Profiles in the 5mm Nozzle at B=175. . . . .	70
25	Measured Radial Density Profiles in the 5mm and 2.5mm Nozzles at B=590 . . . . .	71
26	Measured and Calculated Radial Density Profiles in the 2.5mm Nozzle at B=1230 . . . . .	72
27	Radial Temperature Profiles for Two Different Reynolds Numbers . . . . .	73
28	Radial Pressure Profiles for Two Different Reynolds Numbers . . . . .	74
29	Experimental Variation of Normalized Temperature, Density and Pressure with Radial Distance near Nozzle Exit; B=590, $p_o/p_\infty = 310$ . . . . .	75
30	Gas Properties along Nozzle Wall for B = 590, $p_o/p_\infty = 310$ . . . . .	76
31	Flow-Visualization Photographs Showing Flow Separation at Low $p_o/p_\infty$ . . . . .	77
32	Density Profiles in Plume of 5mm Nozzle for B = 590 and $p_o/p_\infty = 310$ . . . . .	78
33	Density Profiles in Plume of 5mm Nozzle for B = 1550 and $p_o/p_\infty = 325$ . . . . .	79
34	Maximum Nozzle Pressure Ratios for the Two Nozzles as a Function of Reynolds Number . . . . .	80
35	Flow-Visualization Photographs for 2.5mm Nozzle at Various Values of B and $p_o/p_\infty$ . . . . .	81
36	Jet Temperatures Just Downstream of Nozzle Lip as a Function of Ambient Pressure . . . . .	82
37	Effect of Ambient Pressure on Centerline Temperatures .	83
38	Measured Discharge Coefficients Compared with Previous Data . . . . .	84

## LIST OF SYMBOLS

### Roman Symbols

$A$	cross-sectional area of nozzle
$B$	nozzle Reynolds number ( $\rho_0 \hat{u} r_*/\mu_0$ )
$C_D$	nozzle discharge coefficient
$G$	function of $K'$ and $T_R$ - see Eq. (4)
$H$	total enthalpy
$I$	intensity of spectral band or line
$J$	electron beam current
$J_i$	electron beam current inside nozzle
$K'$	rotational quantum number in $B \ ^2\Sigma_u^+$ state of $N_2^+$
$M$	Mach number
$m$	molecular weight
$p$	gas pressure
$R$	universal gas constant
$Re_*$	throat Reynolds number ( $\rho_* u_* r_*/\mu_*$ )
$r$	radial distance
$r_L$	longitudinal radius of curvature at throat
$r_*$	throat radius
$S$	entropy
$T$	gas temperature
$T_R$	rotational temperature
$t$	time variable
$u$	flow velocity

## LIST OF SYMBOLS (Cont'd)

$\hat{u}$	adiabatic escape speed ( $\sqrt{2H'_0}$ )
$\dot{V}$	volumetric pumping speed of low-density tunnel
$Z_r$	rotational collision number
$z$	distance along axis of nozzle ( $z=0$ at throat)
$z'$	distance along axis of nozzle plume ( $z'=0$ at the nozzle exit plane)
$z_M$	distance between orifice and Mach disc in a free jet

### Greek Symbols

$\gamma$	specific heat ratio of gas
$\sigma$	shock thickness
$\theta_R$	characteristic rotational temperature
$\theta_1$	wall angle of subsonic section of nozzle
$\theta_2$	wall angle of supersonic section of nozzle
$\lambda$	wavelength of light
$\mu$	viscosity
$\nu_{col}$	molecular collision frequency
$\rho$	gas density
$\Omega$	function of temperature - see Eq. (12)

### Subscripts

$o$	stagnation chamber properties, reference value
$*$	values at throat of nozzle
$\infty$	ambient conditions in text section
$c$	gas properties on centerline of flow

## LIST OF SYMBOLS (Cont'd)

$\bar{E}$  conditions on centerline just outside of nozzle exit  
w gas properties at the wall

## I. INTRODUCTION

Low-thrust rocket engines are required for providing the small corrections necessary to maintain proper attitude and to make minor changes in the trajectory of orbiting satellites and deep-space planetary probes. Thrust levels are usually a fraction of a pound-force and may in some instances be as low as  $10^{-6}$  lbf ( $\approx 1/2$  dyne). Small nozzle scale and low reservoir pressures combine to give throat Reynolds numbers in the range between  $10$  and  $10^4$ . At the lower end of this range the viscous boundary layer is quite thick and tends to fill the entire cross-section of the nozzle. Under these conditions an inviscid analysis followed by a boundary layer correction is no longer adequate, especially when transition-flow characteristics, such as slip at the wall, have to be taken into account. Difficulties in predicting the thrust and mass-flow levels that will occur in the vacuum of the space environment make the flight rating of these thrusters a very lengthy and expensive process. Frequently the uncertainty in nozzle performance causes a penalty in greater system complexity.

An understanding of low-Reynolds-number flows through supersonic nozzles is also required in the design of low-density wind tunnels. Nozzles may be relatively large in this case, but gas densities are often correspondingly low to provide the free-molecule or transition-flow conditions required for the testing of space vehicles (e. g. the proposed space shuttle) which spend part of their mission in the outer fringes of the atmosphere.

Few experimental data exist with respect to nozzle performance at Reynolds numbers less than  $10^4$ . Available information is to a major part limited to gross characteristics such as thrust and discharge coefficients and contributes relatively little to an understanding of the flow structure itself. Discharge coefficients, for example, have been determined by Milligan<sup>1</sup> at throat Reynolds numbers between  $10^{-1}$  and  $10^3$  and recently by Massier et al.<sup>2</sup> at Reynolds numbers between  $10^3$  and  $10^6$  for a few isolated geometries. A relatively detailed survey of static and total pressures throughout the flow in a nozzle, operating at a Reynolds number of approxi-

mately  $10^3$ , has been reported by Yevseyev<sup>3</sup>. His work also includes a study of the effects of back pressure on the internal flow. A general review of microrocket technology prior to 1966 is given by Sutherland and Maes<sup>4</sup>.

Among several theoretical methods, which have been applied to low-density nozzle flows, the slender-channel formulation has been found to give a reliable description of the flow at Reynolds numbers applicable to micro-thrust rockets. The slender-channel equations were first used by Williams<sup>5</sup> in a similar-solutions analysis and were later applied by Rae<sup>6</sup>, who obtained general numerical solutions for several realistic nozzle configurations. The results of Rae's calculations, which were performed in an earlier phase of the present program, are generally consistent with the experimental pressures and Mach numbers reported by Yevseyev<sup>3</sup> at a Reynolds number of  $10^3$ . The series of experiments described in the present paper was initiated for the purpose of substantiating some of the predictions made by Rae<sup>6</sup> at lower Reynolds numbers, and for providing new data which may be used as a basis for formulating an improved version of this theory. One of the more startling features of this theory is the prediction of a closed supersonic region embedded in a viscous subsonic flow at a Reynolds number of 100. A confirmation or refutation of the reality of such a supersonic "bubble" constitutes a critical test of the slender-channel formulation. The range of experimental conditions was chosen to make this test possible.

An electron-beam fluorescence probe was used in the present experimental program as the primary diagnostic tool for determining gas densities and temperatures throughout the flow field. The investigation was carried out in a steady-flow low-density tunnel at nozzle Reynolds numbers in the range  $100 < B < 1500$ . For the sake of easy comparison with Rae's calculations, the Reynolds number  $B$  used here is identical with his and is defined by

$$B = \rho_0 \hat{u} r_* / \mu_0, \quad (1)$$

where  $\rho_0$  and  $\mu_0$  are gas density and viscosity in the stagnation chamber. The symbol  $\hat{u}$  represents the adiabatic escape speed ( $\hat{u} = \sqrt{2H_0}$ ), and



$r_*$  is the throat radius. For a diatomic gas ( $\gamma = 7/5$ ),  $B$  is related to the more commonly used throat Reynolds number,  $Re_*$ , based on flow conditions in the throat and the throat radius, by

$$B \approx 3.5 Re_* . \quad (2)$$

In the following section the electron beam technique for determining static temperatures and densities in nitrogen is briefly reviewed. (This is not meant to be a complete survey of previous work in this field.) The instrumentation and experimental procedure are described in Section III. Results are presented and discussed in Section IV.

## II. ELECTRON BEAM TECHNIQUE

When a well-collimated, high-energy, low-current electron beam is passed through a gas a minute fraction of the gas molecules is excited to higher-lying electronic states through inelastic collisions. Spontaneous transitions to lower energy levels gives rise to a fluorescence, which is largely confined to the volume pervaded by the electron beam, due to the short lifetimes of the excited states. At low pressure levels (  $< 0.5$  torr) collisional quenching effects are unimportant, and the radiation emitted from a small volume of gas in the electron beam is directly proportional to the local number density of molecules and, hence, can be used to determine mass densities at a point in a gasdynamic flow. This method was first proposed and used by Schumacher and Gadamer<sup>7</sup>, and has since found acceptance as a routine technique for measuring gas densities in low-density aerodynamic research.

At low pressures the spectrum of electron-beam excited nitrogen consists primarily of the bands of the first negative system of  $N_2^+$ , which are the result of transitions from the  $B^2\Sigma_u^+$  state to the ionic ground state,  $X^2\Sigma_g^+$ . The most intense band of this system is the 0-0 vibration-rotation band, the bandhead of which lies at a wavelength of  $3914 \text{ \AA}$ . It is this band which was analyzed spectrometrically in the present study to derive gas densities and temperatures. The rotational fine-structure in this emission band is indicative of the relative number distribution of excited molecules among the rotational energy levels of the  $B^2\Sigma_u^+$  state. If the statistical rules governing the excitation process from the neutral ground state to the  $B^2\Sigma_u^+$  state are understood, the original undisturbed population of the rotational energy levels in the ground state can be derived.

When a gas molecule absorbs a quantum of energy from a passing electron of kilovolt energy, the process of excitation, due to the rapidly changing electro-magnetic field of the moving electron, is not unlike the excitation produced by the absorption of a photon. Consequently, it may be assumed that the optical selection rules can be applied to the electron-beam

excitation process. This assumption was employed by Muntz<sup>8</sup>, who first suggested that the electron beam may be used to determine gas temperatures in nitrogen flows. He showed that the method gives accurate temperature measurements in the range between 300 °K and 400 °K. Experiments performed subsequently in expanding flows of nitrogen by Robben and Talbot<sup>9</sup>, Marrone<sup>10</sup>, Ashkenas<sup>11</sup>, and Petrie and Boiarski<sup>12</sup> have shown that even very low temperatures can be determined in supersonic flows by the electron beam method, provided the following conditions exist:

1. The flow is expanding at a rate slow enough and at densities high enough for the rotational degrees of freedom to remain in equilibrium with translational random energies.
2. The radiation analyzed derives from excited molecules which have been produced by collisions with high-energy electrons only.

If condition 1 is satisfied, a Boltzmann distribution is generally observed for the rotational energies of the molecules. However, under extreme nonequilibrium conditions, as found in shock compressions and low-density free jet expansions, pronounced non-Boltzmann distributions have been observed<sup>10, 13</sup> for the rotational degrees of freedom.

The second condition is necessary to exclude the effects of low energy secondary electrons. For excitation by low-energy electrons ( $< 200$  eV) the optical selection rules are known to be violated (see e. g. Polyakova et al.<sup>14</sup>), so that the method of interpretation used by Muntz<sup>8</sup> would indicate an apparent non-Boltzmann distribution of rotational energies. Since a fraction of the electron beam luminescence is caused by low-energy secondaries (Harbour et al.<sup>15</sup>), produced in ionizing collisions of primaries with gas molecules, a small apparent deviation from Boltzmann behavior is generally observed. This is most pronounced for the rotational lines corresponding to higher rotational quantum numbers ( $K > 10$ ). If this effect is ignored the measured rotational temperatures are generally too high. The discrepancy is of the order of 10 K° and is approximately constant over the temperature range of interest here. Petrie and Boiarski<sup>12</sup> have studied this

effect under conditions where rotational freezing was absent, and have found that, if care is taken to observe the center of the electron beam only, and if the low-intensity lines in the tail of the band are excluded from the analysis, then the discrepancy does not exceed 5 K° in the temperature range from 20°K to 300°K. Under these conditions, the effect of secondary electrons on the measured temperatures is negligible at room temperatures and becomes important only at extremely low temperatures. At static temperatures above 50°K the error amounts to less than 10%.

The change with temperature of the rotational fine-structure in the R-branch of the 0-0 band of  $N_2^+(1-)$  is illustrated in Fig. 1, which shows two records obtained during the present experimental program with a scanning spectrometer described in the next section. The wavelength range scanned is only about 20 Å, which gives an indication of the spectral resolution required ( $\approx 0.5$  Å). The  $K'$  numbers are the rotational quantum numbers of the excited molecules in the  $B^2\Sigma_u^+$  state. Even-numbered lines have one half the intensity of the odd-numbered lines, due to the different statistical weights of the rotational levels. The decrease in the population of the higher rotational states with decreasing temperature is clearly evident in Fig. 1. At 250°K lines of maximum intensity correspond to  $K' = 6$  and 7, whereas at 80°K this maximum has shifted to lines  $K' = 3$  and 4. Also, at the lower temperature a much faster drop-off of line intensity is observed in the tail of the band.

Under equilibrium conditions the rotational temperature,  $T_R$ , is defined by the ratio of any two line intensities (e.g.  $K' = 3$  and  $K' = 9$ ). More accurate temperature determinations are obtained, however, by making use of all the line intensities in a procedure described by Muntz<sup>8</sup>. This method of data reduction also provides information about a possible non-Boltzmann distribution of rotational energies. The procedure followed throughout the present experiments is similar to that of Muntz and is described hereunder.

For the R-branch of the 0-0 band the line intensity,  $I(K')$ , for a given rotational temperature,  $T_R$ , is given<sup>8</sup> by

$$I(K') = (\text{constant}) 2 K' G(K', T_R) (\lambda_o/\lambda)^4 e^{-K'(K'+1) \theta_R/T_R}, \quad (3)$$

where  $\lambda$  is the wavelength of the line, and  $\lambda_0$  is a reference wavelength, here taken to be that of the rotational line corresponding to  $K' = 1$  (i. e.  $\lambda_0 = 3909.7$ ). The factor  $\Theta_R$  in the exponent is the characteristic rotational temperature of the nitrogen molecule in the 0th vibrational level. The numerical value of  $\Theta_R$  is  $2.87^\circ\text{K}$  (see e. g. Herzberg<sup>16</sup>). The function  $G(K', T_R)$ , which includes the Hönl - London rotational transition probabilities, may be expressed as

$$G(K', T_R) = \frac{(K'+1) e^{-2(K'+1) \Theta_R/T_R} + K' e^{2K' \Theta_R/T_R}}{2K'+1} \quad (4)$$

Equation (3) is valid only for temperatures below approximately  $800^\circ\text{K}$ , to preclude any appreciable population in all but the lowest vibrational level. A convenient form of Eq. (3), which indicates more directly the method of data reduction, is obtained by rewriting it as

$$\log_{10} \frac{I(K')}{2K'G(\lambda_0/\lambda)^4} = - \frac{1}{2.3} \frac{\Theta_R}{T_R} K'(K'+1) + \text{const.} \quad (5)$$

To derive a rotational temperature from the recorded spectrum, relative line intensities were first obtained by measuring the heights of the lines in the band. For even-numbered lines the intensities were multiplied by a factor of two. The relative line strengths were then normalized by dividing each line intensity by its corresponding value of  $2K'G(\lambda_0/\lambda)^4$ . Logarithmic values of this function were calculated with the aid of a computer for the first 21 lines in the band and over a temperature range from  $2^\circ\text{K}$  to  $800^\circ\text{K}$ . A table of these calculated values can be found at the end of this report (Table 1). Since  $G$  is itself a function of  $T_R$ , a value of  $T_R$  was first estimated from the ratio of two of the line intensities. This temperature was sufficiently accurate, so that the correct normalization factors could be determined without further iteration. When the logarithms of the normalized line intensities are plotted against  $K'(K'+1)$ , the pattern of points defines a straight line for a Boltzmann distribution of rotational energies (Fig. 2). The inverse slope of this line is proportional to the rotational temperature (see Eq. 5).

So as to minimize the effect of secondary electrons on the temperature determination, all line intensities in the tail of the band which measured less than 10% of the maximum line intensity were omitted in the data reduction for reasons discussed earlier. The cut-off point at 10% maximum intensity was an arbitrary choice, but was consistent with the signal-to-noise ratio for most of the recorded data. Lines beyond the cut-off point were generally affected by the random noise to the extent that intensities could no longer be determined with sufficient accuracy to be useful in defining a rotational temperature. For example, the data analysis was restricted to the first 13 lines at 200°K and to the first 7 lines at 50°K. The information thrown away in the tail of the band pertains to a small fraction of the total rotational energy in the gas only, so that the temperatures calculated are still representative of the state of rotational excitation.

Within the limits of the described data analysis no deviation from Boltzmann behavior was observed. Random experimental errors varied from  $\pm 1\%$  to  $\pm 5\%$  and were estimated from a statistical analysis of the scatter of points around the straight-line plot.

### III. EXPERIMENTAL ARRANGEMENT AND PROCEDURE

All experiments were performed in the test section of a steady-flow low-density tunnel, which was designed and assembled for the purpose of testing low-mass-flow devices of the type discussed in this report. Measurements of gas density and temperature were obtained by the electron beam technique described in the previous section. To generate the electron beam, an existing electron gun system, which had been used in a previous set of experiments,<sup>17, 18</sup> was modified and mounted on top of the test section of the new facility.

#### 1. Low-Density Tunnel

Two views of the low-density tunnel and the electron gun are shown in Figs. 3 and 4. The test section is rectangular and is 36 cm wide, 40 cm high and 100 cm long. It is made from mild steel, which helps to shield the interior from possible transient magnetic fields originating from electrical apparatus located elsewhere in the laboratory. Magnetic shielding aids in maintaining proper beam alignment during the experiments. The test section has four circular access ports (diameters are 15, 20, 30 and 30 cm), which can be used for observation windows or for mounting instrumentation.

The mass flow capability of the tunnel is provided by an Edwards 18B4 oil-vapor booster pump, which has an unbaffled pumping speed for air of 3000 l/s at 1  $\mu$ Hg and of 1500 l/s at 50  $\mu$ Hg. The booster pump is backed by a 60 l/s rotary pump. The test section may be isolated from the booster pump by a 30 cm water-cooled right-angle isolation valve. The valve body forms an integral part with a 30 cm diameter duct connecting the test section to the booster pump (Fig. 4). The valve can also be locked in any arbitrary partially open position to throttle the mass flow through the tunnel. A freon-refrigerated chevron baffle is used on top of the booster pump to condense pump fluid vapors in order to prevent them from entering the test section. The flow impedance caused by the baffle and the valve reduces the effective pumping speed of the tunnel to approximately 1500 l/s at 1  $\mu$ Hg and to 1000 l/s at 50  $\mu$ Hg test section pressure.

The experimentally determined mass flow characteristics of the tunnel for nitrogen are given in Fig. 5. A calibrated flow meter (see Sec. III, 2) was used for determining these values. At a test section pressure of  $10 \mu \text{ Hg}$  the unthrottled mass flow rate for nitrogen is  $1 \text{ g/min}$ . The maximum mass flow that can be handled by this facility is approximately  $5 \text{ g/min}$  at a test section pressure of  $70 \mu \text{ Hg}$ .

Gas pressures in the test section can be measured accurately by a liquid-nitrogen-trapped mercury McLeod gauge (CVC-100A). In addition, a Varian "Millitorr MIG-10" high-pressure ionization gauge with a range of  $10^{-5}$  to 1 torr is mounted on the side of the test section for providing approximate but instantaneous readings of the test section pressure. A large dial-type 0-20 torr diaphragm gauge serves as an indicator for ensuring that the pressure in the backing line of the booster pump stays below the limiting pressure of 2 torr.

The preceding description refers to the basic vacuum chamber and associated pumps. Additional apparatus and instrumentation, assembled specifically for the present experiments, is discussed in sequence in the following subsections. A general outline of the experimental arrangement is presented in Fig. 6. Grouped around the test section are three subsystems: the stagnation chamber, SC, with nozzle, N, and gas metering system, F; the electron gun, G, projecting an electron beam, B, vertically through the test section; and finally an optical mirror system, O, and two spectrometers,  $S_1$  and  $S_2$ , for analyzing the beam luminescence. In the following paragraphs it will be helpful to refer back to the general outline in Fig. 6.

## 2. Stagnation Chamber and Flow Meter

The stagnation chamber and nozzle holder, SC (Fig. 6), projects into the test section through one of the side ports. It consists of a 5 cm diameter stainless steel tube, which telescopes into a larger tube mounted on a movable flange (Fig. 7). With this arrangement the stagnation chamber can be aligned laterally and axially for positioning the nozzle relative to the electron beam. It can also be translated at a uniform rate in the axial direction by means of a lead-screw assembly driven by a synchronous motor.



A second motor-driven slide assembly (Fig. 7), which moves at the same rate as the nozzle, has been built as a camera platform for the purpose of flow visualization.

The structure of low-density nozzle plumes or free jets can be photographed by moving the electron beam relative to the flow field in a plane defined by the beam and the flow axis, while taking a time exposure of the beam luminescence. Since the beam luminescence is everywhere proportional to the gas density, a density map of a two-dimensional flow section is recorded on the film. The technique has been described in an earlier paper.<sup>19</sup> With the present arrangement, the nozzle and the camera, C (Fig. 6), which observes the electron beam through the glass window, W, are moved at uniform and equal velocities relative to the stationary electron beam.

The gas flow into the stagnation chamber and through the nozzle can be adjusted by a fine-control needle valve, V, and can be measured with a calibrated flow meter, F (Fig. 6). The latter is a Fischer-Porter "Tri-Flat" flow rater and consists of a graduated tapered glass tube and an interchangeable 3.2 mm diameter spherical float (sapphire, stainless steel, or tantalum). Float materials of different specific weights are used for different mass flow ranges.

In the experiments the flow meter has been used with nitrogen (Matheson, High Purity grade) at a pressure,  $p_f$ , of 20 psia (1034 torr). Mass flow rates of nitrogen through the nozzle are determined from calibration curves supplied by the manufacturer for this flow meter. Quoted accuracy of the calibration is  $\pm 2\%$  of full-scale deflection. Full-scale readings correspond to mass flow rates of 3.3 g/min with the tantalum float and 1.4 g/min with the sapphire float. Stagnation chamber pressures,  $p_o$ , in the range between 0 and 20 torr are measured with a mechanical diaphragm gauge connected to the stagnation chamber.

### 3. Electron Gun System

The electron gun employed in the present experiments has been described in Ref. 17. For completeness, a brief description of this unit is repeated here.

The 15kV electron beam is produced by a standard cathode-ray gun (Superior Electronics, SED-110) with an indirectly heated alkaline-earth cathode and electrostatic focusing lenses. The gun is housed in a stainless-steel chamber maintained at a vacuum of approximately  $10^{-6}$  torr by a liquid-nitrogen trapped oil-vapor diffusion pump. From the gun chamber the electron beam passes through a small aperture into an intermediate-pressure chamber, IC (Fig. 6), and from there through a second aperture into the test section. A continuously pumped intermediate-pressure chamber is required to maintain a satisfactory vacuum in the gun chamber, when the test section pressure is above  $10^{-3}$  torr. The upper aperture consists of a 2 mm diameter hole in a 6 mm thick copper plate; the lower aperture is a 1 mm hole in a similar plate. Alignment of the electron beam with respect to the apertures is achieved by shifting and tilting the electron gun mechanically.

After passing vertically through the test section the electron beam is terminated in a collector cup at the bottom of the test section. The beam collector consists of a hollow copper block lined with a graphite insert. The copper block is electrically insulated from ground by a boron-nitride support, so that the beam current can be measured with a micro-ammeter. Beam currents between 100 and 200  $\mu$ A can be obtained with this gun.

The electron beam may be passed through different regions of the flow by moving the nozzle, N, with respect to the electron beam. Keeping the electron beam fixed in the laboratory frame of reference has the advantage that the optics need not be re-aligned, when the point of observation is moved to a new position in the flow field.

### 4. Optical Instrumentation

The electron beam fluorescence is analyzed by two separate spectrometers,  $S_1$  and  $S_2$ , which view the beam from the downstream direction (Fig. 6). The optical system, O, can be adjusted to form an image of the electron beam in the entrance-slit plane of either instrument. The slits are

masked, so that light originating in a small volume of the beam only can enter. A test section window made of quartz is used to assure uniform transmission of light in the near ultraviolet.

The optical imaging system consists of three mirrors, two plane diagonals,  $M_1$  and  $M_2$ , and a spherical collimator,  $M_3$ , mounted vertically above the diagonals. Mirror  $M_2$  can be turned through  $90^\circ$  around a vertical axis, and mirror  $M_1$  can be rotated around a horizontal axis by a motor-driven linkage. The mirror arrangement and linkage design are shown in more detail in Figs. 8 and 9.

Rotational temperature determinations are made with diagonal mirror  $M_2$  in the position shown in Fig. 6. In this position the spherical mirror,  $M_3$ , produces a real, full-size image of the beam at the slit of a  $3/4$  m grating spectrometer,  $S_1$ , which has a Czerny-Turner arrangement of mirrors and a  $f/6.5$  aperture. The rotational fine-structure of the  $N_2^+$  band is determined with this instrument, which is used in second order, where the linear dispersion is  $5 \text{ \AA/mm}$ . The entrance slit is  $0.030$  mm wide and  $1$  mm high and is parallel to the beam image. The slit opening defines the spatial resolution for this type of measurement. To analyze the molecular band structure the spectrum is scanned across the  $0.1$  mm wide exit slit by rotating the diffraction grating. An EMI-6256S quartz-window photomultiplier with a modified S-13 response serves as the detector. The photomultiplier signal is amplified by an electrometer,  $A$ , and recorded with an ink-pen recorder,  $R$ . Approximately 3 minutes are required for a typical scan.

For measuring local gas density, the mirror  $M_2$  is rotated  $90^\circ$  around a vertical axis (Fig. 8), so that the beam image is formed on the slit of a low-dispersion ( $33 \text{ \AA/mm}$ ) Ebert-type grating spectrometer,  $S_2$ . This arrangement of mirrors  $M_1$  to  $M_3$  produces a horizontal image perpendicular to the  $S_2$  spectrometer slit. With this image orientation the density measurements are independent of beam spreading due to small-angle scattering. The entrance slit is  $0.5$  mm wide and  $10$  mm long. Here the resulting spatial resolution is determined by the electron beam diameter ( $\approx 1$  mm) in the horizontal dimensions and by the  $0.5$  mm slit width in the vertical

direction. The exit slit is 2 mm wide, so that the entire  $N_2^+(0,0)$  band falls within the flat portion of the trapezoidal slit function. For temperatures below 300°K essentially all molecules are in the vibrational ground state, and the integrated band intensity serves as an accurate measure of gas density. Band intensities are measured with a 1P28 photomultiplier and are recorded as before.

The point of observation can be moved up and down the electron beam by rotating the diagonal mirror  $M_1$  around a horizontal axis. This permits densities and temperatures to be determined at off-axis points in the flow. Rotation of this mirror is controlled by a linkage and a motor-driven micrometer (Fig. 9), such that the micrometer reading corresponds directly to position along the electron beam. Radial density profiles through the flow field are obtained by moving the point of observation along the beam at uniform speed, while recording the total band intensity as a function of time.

Figure 10 gives an overall view of the experimental setup. The low-density tunnel with the electron gun and associated pumps fills much of the central portion of the photograph. On the left are the optical spectrometers and recording instruments. The flow meter and pressure gauges are visible on the right.

## 5. Preliminary Tests

A series of experiments was performed to test and calibrate the electron beam probe and the optical instrumentation in a known flow field. Such a flow is an underexpanded free jet expanding from a sonic orifice. Free jet structure is relatively well understood from previous theoretical<sup>20, 21</sup> and experimental<sup>22, 23, 24, 10</sup> work.

A free jet exhausting into an ambient gas at non-zero pressure is characterized by a closed pattern of shock waves, which surround the expansion plume and isolate it from the effects of the ambient pressure. The shock pattern consists of a barrel-shaped shock enveloping the jet and a plane shock which is normal to the streamlines and terminates the expansion. This normal shock is generally referred to as the Mach disc. The

distance,  $z_M$ , between the sonic orifice and the Mach disc has been found<sup>21, 22, 23</sup> to be proportional to the orifice radius,  $r_*$ , and to the square root of the pressure ratio across the orifice, and is given by the empirical law

$$z_M = \frac{4}{3} r_* (p_o/p_\infty)^{\frac{1}{2}}, \quad (6)$$

regardless of the specific heat ratio,  $\gamma$ , of the gas.

For a given pumping capacity of the tunnel, the pressure ratio,  $p_o/p_\infty$ , which can be maintained across the orifice, is indirectly proportional to the orifice area. When the mass flow equations describing tunnel performance are combined with Eq. (6), then the distance  $z_M$  is found<sup>23</sup> to be proportional to the square root of the volumetric pumping speed,  $V$ , of the tunnel, independent of orifice size. The derived relation is

$$z_M = \frac{4}{3\sqrt{\pi}} \left( \frac{\gamma R T_o}{m} \right)^{-\frac{1}{4}} \left( \frac{\gamma+1}{2} \right)^{(\gamma+1)/4(\gamma-1)} \dot{V}^{\frac{1}{2}}, \quad (7)$$

where  $R$  is the universal gas constant and  $m$  is the molecular weight of the test gas. In this equation the dependence of  $z_M$  on  $\gamma$  is very weak. A change in the value of  $\gamma$  from 1.3 to 1.67 produces only a 4% variation in  $z_M$ . If, furthermore, the volumetric pumping speed of the tunnel is inversely proportional to the square root of the molecular weight (a good approximation for most pumping systems), then  $z_M$  becomes essentially independent of the gas used and can be considered a figure of merit of the particular facility.

In the preliminary tests, free jet plumes of argon, helium, carbon-dioxide and nitrogen were produced with a sharp-edged 5 mm diameter orifice. Flow visualization photographs, acquired by the technique described in Subsection 2, are shown in Figs. 11 and 12. Jets in Figs. 11 and 12A were obtained with the maximum available pumping speed of the tunnel and with a stagnation pressure of 9.8 torr. For Ar,  $N_2$  and  $CO_2$  the observed value of  $z_M$  is approximately 67 mm. This figure is consistent with Eq. (7) and the pumping speeds determined with the flow meter ( $\approx 1600$  l/s for  $N_2$  and correspondingly less for Ar and  $CO_2$ ).

If the inverse proportionality of  $\dot{V}$  to the square root of the molecular weight were exact, then the pumping speed for helium should be 3.2 times that for argon. For the type of diffusion pump used in the present facility, the actual pumping speed for helium is only about 2.2 times the volumetric pumping rate for argon. Consequently, in the helium jet (Fig. 11, center) the Mach disc lies closer to the orifice than for the other jets. Furthermore, the barrel shock and Mach disc are considerably more diffuse for helium due to the higher value of its viscosity at similar temperatures.

Whereas the distance to the Mach disc is insensitive to  $\gamma$  for a given pumping capacity, the Mach disc diameter is not. The latter approximately doubles as  $\gamma$  decreases from 1.67 for argon to 1.28 for  $\text{CO}_2$  (Fig. 11). A corresponding widening of the plume and an increase in the angle of inclination of the jet boundary at the orifice are also evident from the photographs. This behavior is consistent with calculations performed by Love et al.<sup>21</sup> using the method of characteristics.

The free jets of Fig. 12 were all obtained with nitrogen as the test fluid. A comparison between Figs. 12A and 12B demonstrates the change occurring in the free jet structure when the jet Reynolds number is decreased by a factor of 1/2 with no appreciable change in the orifice pressure ratio. Owing to the increased importance of viscous effects in Fig. 12B the shock pattern has become so diffuse that the Mach disc is no longer recognized as a separate feature. The general size and shape of the expansion cell has remained the same, however. It was shown in Ref. 24 that the dimensionless Mach disc thickness  $\delta/z_M$  is proportional to  $(p_0/p_\infty)^{-\frac{1}{2}}$  for a given gas and a fixed orifice size and stagnation temperature. Consequently, the shock thickness for the jet in Fig. 12B is approximately twice that for the jet in Fig. 12A.

When the jet Reynolds number is kept constant (constant  $p_0$ ), but the pressure ratio across the orifice is decreased from 323 to 100, the appearance of the free jet changes from that of Fig. 12B to the configuration of Fig. 12C. In accordance with Eq. (6) the size of the expansion cell of Jet C has decreased to 0.56 times the size of jet B (or A). At the same time the thickness of the shock envelope has decreased by an additional factor of

0.56 because of the change in the quantity  $(p_0/p_\infty)^{-\frac{1}{2}}$ . The definition of the barrel shock and Mach disc is thereby increased almost to the level of the definition present in Fig. 12A.

By scanning along the electron beam with the rotating mirror, a series of radial density profiles through the plume of a nitrogen free jet was obtained. The conditions for this jet ( $p_0 = 9.2$  torr,  $r_* = 2.5$  mm) were similar to those for the jet depicted in Fig. 12A. The experimental density profiles have been arranged in Fig. 13 in a sequence of increasing distance,  $z$ , from the orifice. The first and last profiles are 1.5 cm and 10 cm from the orifice, respectively. The width of each profile represents a distance of 10 cm measured diametrically through the plume. Between  $z/r_* = 6$  and  $z/r_* = 12$  the most notable features of the free jet are the rapid decrease in axial density and the gradual development of the barrel shock. For distances larger than  $12r_*$  the central density is below the ambient density (equivalent to  $29\mu\text{Hg}$ ) until the flow passes through the Mach disc, the center of which lies between  $26r_*$  and  $27r_*$ . Profiles for  $z/r_* > 28$  describe the region downstream of the Mach disc. In this region the most prominent feature is the reflected barrel shock, which gradually dissolves with increasing distance from the Mach disc due to the viscous nature of the flow.

Densities and temperatures determined at points along the axis of this free jet are compared with isentropic theory in Fig. 14. The thermodynamic variables have been normalized here by the corresponding stagnation chamber properties. The densities given represent the center points of the set of radial density profiles in Fig. 13. The extreme points of each radial density scan lie outside of the free jet and serve as calibration points, since the ambient density is known from the measured pressure and temperature in the test section. Densities elsewhere along the profile are taken to be proportional to the photomultiplier signal, which in this case represents the integrated band intensity. For  $z/r_* < 16$  the measured centerline densities are in excellent agreement with isentropic theory. The isentropic curves are based on Owen and Thornhill's<sup>20</sup> method of characteristics calculations in the far field and on measurements reported by Ashkenas and Sherman<sup>23</sup> near the orifice. For large values of  $z/r_*$  the density is expected to fall off

as  $z^{-2}$  (see Ref. 23). At  $z/r_* > 16$  the experimental densities deviate from the isentropic curve because of the flow going through the Mach disc there. Close to the orifice the agreement is good to distances as small as  $z/r_* = 2$ . The local pressure at this point is approximately 0.5 torr. Hence, it may be concluded that the band intensity is approximately proportional to gas density up to pressure levels of several hundred microns. At higher pressures quenching effects become important (Brocklehurst and Downing<sup>25</sup>), and suitable corrections should be applied.

Measured temperatures deviate from the isentropic curve in a region where the density still decreases as the inverse square of distance. The present measurements agree closely with data by Marrone<sup>10</sup> (dotted curve) for a similar Reynolds number ( $p_o r_* = 20$  torr-mm compared with 23 torr-mm for the present jet). The observed deviation may be interpreted as rotational freezing in the rapidly expanding free jet. The question of the possibility of rotational freezing in nozzle flows will be discussed in Section IV. Nonequilibrium effects of this type are not expected, because the nozzle flows investigated expand at a considerably slower rate than this free jet.

The results of the preliminary experiments have demonstrated the usefulness of the flow visualization technique; and the method for obtaining radial density profiles, by scanning along the electron beam with a rotating mirror, has proven to be a workable procedure. The agreement of measured densities and rotational temperatures with theory and previous experiments has shown that the present arrangement of the optical instrumentation and the method of data reduction are suitable for obtaining accurate values of these quantities at selected points throughout an expanding supersonic flow.

## 6. Nozzles and Their Interaction with the Electron Beam

### Nozzle Construction

For the study of low-density viscous nozzle flows two supersonic nozzles with different throat diameters were fabricated (Fig. 15). Both nozzles are machined from black graphite to reduce optical reflections. The low



atomic number of carbon also helps to minimize backscattering of beam electrons and emission of secondary electrons, when the beam is terminated on or in the nozzle. The internal contours of the nozzles are geometrically similar, and the throat diameters are 5.1 mm and 2.5 mm. Each nozzle has a conical subsonic portion with a  $30^\circ$  half-angle and a diverging supersonic expansion cone with a  $20^\circ$  half-angle. A relatively sharp throat is used with a longitudinal radius of curvature equal to  $1/4$  the throat diameter (or  $r_*/2$ ). The area ratio at the exit is 66.

Small holes are drilled through the top wall of each nozzle to permit the electron beam to enter the nozzle interior. The hole diameters decrease towards the throat and are less than two local molecular mean free paths for the majority of the present tests. Hence, the flow disturbance caused by these holes is considered negligible. The nozzles are built from two halves, which are electrically insulated from each other and from ground, so that the portion of the electron current intercepted by each half can be measured separately. This feature makes it possible to optimize the alignment of a given hole with respect to the electron beam and to determine the beam current inside the nozzle.

### Reynolds Number Regimes

Flow visualization studies of the external plume structure have indicated that the flow inside the nozzle is adversely affected if the ambient test section pressure exceeds the jet pressure at the nozzle exit. Because of pumping limitations, the 5 mm nozzle could only be used at Reynolds numbers,  $B$ , below 600, if adverse effects due to the ambient pressure were to be avoided. For a fixed stagnation temperature, the mass flow through the nozzle is proportional to  $p_o r_*^2$  or  $Br_*$ . Hence, for a specified mass flow (and a corresponding test section pressure) the nozzle Reynolds number is inversely proportional to nozzle size. Therefore, if the mass flow is to be kept constant,  $r_*$  must be decreased in order to increase  $B$ . Conversely, for a specified value of  $B$ , the smaller nozzle can be operated at a lower test section pressure. For this reason the 2.5 mm nozzle was used for all data above  $B = 600$ . Minimum test section pressures as a function of stagnation chamber pressure are given in Fig. 16 for the two nozzles.

### Wall Heating

Figure 17 is a photograph of the electron beam traversing the inside of the 5 mm nozzle through the outermost hole. Since, under these circumstances, all the kinetic energy of the electron beam (1.5 W) is intercepted by the nozzle surfaces, the local wall temperature may increase by as much as  $100^{\circ}\text{K}$  (calculated value) if exposed continuously to the beam. To prevent hot nozzle walls from influencing the measurements, only one density scan or temperature determination was performed at a time. The electron beam was then immediately turned off (or the nozzle was moved out from under it), and a high mass flow ( $> 1 \text{ g/min}$ ) of nitrogen was passed through the nozzle for a minimum period of 10 minutes, to bring the wall temperatures back to the adiabatic equilibrium values before proceeding with the next measurement. The 10 minute interval was found to be more than adequate, since variations in the cooling time produced no change in the gas temperatures measured near the wall.

### Current Measurement

The electron current entering the nozzle interior was generally less than half the original beam current leaving the gun, because a fraction of the beam was stripped off at the hole in the top wall of the nozzle. A knowledge of the electron current at the point of measurement is not necessary for temperature determinations. However, in order to convert beam intensity to gas density an effective value of the local beam current must be known. This requirement poses a problem for the measurement of gas densities inside the nozzle. Due to backscattering and secondary emission of electrons at the nozzle surfaces, the current indicated by the bottom half of the nozzle is generally not equal to the effective number flow of high energy electrons through the volume of observation. For the same reason, the sum of currents intercepted by both nozzle halves was found to be lower than the original beam current (measured with the collector cup). The discrepancy varied with beam position in the nozzle, but was never more than 20% of the undisturbed beam current.

## Calibration and Data Reduction

To relate measured currents and beam intensities to local gas densities, a separate calibration study was made under uniform density conditions. In these experiments the test section and stagnation chamber were filled with nitrogen to a specific pressure level (between 10 and 100  $\mu$  Hg), and the total beam current was measured with the Faraday cage. The nozzle was moved into position for the electron beam to enter one of the holes in the nozzle wall. The beam luminosity (0-0 band of  $N_2^+$ ) was recorded as a function of distance along the beam. At the same time the currents intercepted by the nozzle halves were measured. This procedure was repeated for each hole and for several density levels. A sample of such a constant-density scan obtained at a pressure of 50  $\mu$  Hg is presented in Fig. 18A.

The recorded profile indicates that the luminosity along the beam varies with position. The increased radiation near the points where the beam is intercepted, at the top outside and the bottom inside walls, is caused by backscattered and secondary electrons with energies above the 19 eV required to excite the first negative system of  $N_2^+$ . The shape of the internal luminosity profile was found to be relatively insensitive to gas density, which indicates that the electrons involved in the excitation process have considerably higher energies than 19 eV.

This situation made it possible to obtain density profiles for nozzle flows by dividing the recorded intensity profile by the constant-density luminosity curve (Fig. 18B). All density cross-sections determined in this way were symmetrical with respect to the nozzle centerline; a fact, which substantiates the validity of this procedure. Having established the relative shape of a density profile, an absolute value of the centerline density was then determined by relating it to the known ambient density outside the nozzle. The procedure makes use of the measured current ratio and the constant-density calibration of luminosity versus measured beam current. A detailed description of this procedure is indicated in the equation on top of Fig. 18B. The last term of this equation converts  $\rho_c / \rho_\infty$  to  $\rho_c / \rho_0$ . If the measured

current,  $J_i$ , inside the nozzle were equal to the effective beam current there, the product of the first and third terms would give the correct value of  $\rho_c/\rho_o$ . The second term is a correction for the measured current ratio,  $J_\infty / J_i$ , and is obtained from the constant density calibration. This term was always close to unity and ranged from 0.85 for the outermost hole to 1.15 for the hole nearest the throat. In this method of data reduction it is assumed that the gas flow does not influence the current measurements. In practice some such influence may exist, however, since the measured currents include small contributions due to charges collected from the beam-created plasma cloud, the spatial distribution of which is a function of flow velocity.

Based on the uncertainties in the measured currents, the remaining error in the absolute values of the experimental densities is estimated to be less than  $\pm 10\%$ . The relative densities within a given flow cross-section are subject to a smaller uncertainty ( $< 5\%$ ) and are limited only by the finite spatial resolution of the probe.

#### IV. RESULTS AND DISCUSSION

Temperature and density measurements were made throughout the flow inside the test nozzles, using nitrogen at a stagnation temperature of  $T_0 = 300^\circ\text{K}$ . A range of nozzle Reynolds numbers ( $100 < B < 1500$ ) was obtained by varying the pressure,  $p_0$ , in the stagnation chamber. The stagnation chamber pressures required for a specific value of  $B$  are given by

$$p_0 = B/166 \text{ torr, for the 5 mm nozzle,} \quad (8)$$

and by

$$p_0 = B/83 \text{ torr, for the 2.5 mm nozzle.} \quad (9)$$

A representative selection of these measurements is presented in Figs. 19 to 30. In the first series of tests care was taken to ensure that the ambient pressure ( $p_\infty = 2$  to  $10 \mu\text{Hg}$ ) was always lower than the jet pressure at the nozzle exit, so that the plumes were underexpanded.

##### 1. Centerline Temperature

Temperature measurements at points on the centerline of the nozzle show a consistent pattern of change with Reynolds number (Fig. 19). Except for the two lower curves all data in Fig. 19 are experimental. The lower curve represents the ideal expansion, based on inviscid theory and the actual area change in the nozzle. As expected, the departure from inviscid theory becomes greater the smaller the Reynolds number. The experimental error bars in Fig. 19 are random errors only and are based on the signal-to-noise ratio in the rotational spectra.

Two distinctly different types of behavior are observed. For  $B > 500$  the axial temperatures decrease monotonically from throat to nozzle exit. For  $B < 300$ , on the other hand, the temperatures pass through a minimum near  $z = 6r_*$  and then increase again towards the nozzle exit. The temperature increase is the result of thermalization of the flow energy

due to viscous dissipation. It must, therefore, be accompanied by a decrease in velocity and Mach number. For  $B = 110$  the temperatures determined near the exit lie above the sonic conditions for adiabatic flow. If cross-streamline heat conduction is considered to be of relatively minor importance in this region, then the flow emerging from the nozzle may be regarded as subsonic. Hence, the flow in this case expands in the normal manner to supersonic velocities just downstream of the throat ( $M \approx 1.8$  at  $z = 5r_*$ ), but then reverts back to subsonic flow in a viscous shock-free transition. This type of behavior was predicted by Rae<sup>6</sup> for this Reynolds number, and the observation of this phenomenon represents strong support for the validity of the slender-channel formulation.

A direct comparison of experiment with theory is given for  $B = 1230$ . The theoretical curve, which was calculated for the present nozzle geometry with the computer program developed by Rae, indicates agreement between experiment and theory to within 3%. Computational difficulties were experienced with the program when it was applied to the present nozzle geometry and a Reynolds number of  $B = 110$ . At the present time, therefore, only a qualitative substantiation of the slender-channel predictions is possible at this Reynolds number, since the  $B = 110$  solution presented by Rae<sup>6</sup> was computed for a  $15^\circ$  expansion cone.

The temperature rise observed at low Reynolds numbers should not be interpreted as a compression wave, since the experimental density and pressure are decreasing in this region of the expansion (Figs. 21 and 22). It, therefore, cannot be attributed to an upstream effect of the ambient gas. As will be shown later, the basic shape of this temperature profile is not altered by the external gas pressure, as long as the plume remains under-expanded ( $p_0/p_\infty \gtrsim 250$ ). The slowing down of a supersonic channel-flow to subsonic speeds by viscous shear forces alone has not been previously observed. The phenomenon is not altogether new, however, since such a transition takes place in all supersonic compressible boundary layers. In a nozzle it is associated with a frictional choking of the flow, insofar as a decrease in ambient pressure will not increase the mass flow passed by the nozzle, even when the entire flow is subsonic.

Centerline temperatures at the nozzle exit increase with decreasing Reynolds number in the manner shown in Fig. 20. For  $B > 1000$  the value of  $T_E/T_O$  is only slightly greater than the inviscid value. As  $B$  decreases further from 1000 to 100, however,  $T_E/T_O$  increases, from 0.2 to 0.9, and presumably remains close to unity for all values of  $B$  less than 100. This experimental temperature curve suggests subsonic exit Mach numbers for Reynolds numbers below 150.

## 2. Test for Rotational Freezing

The possibility of rotational nonequilibrium occurring in low-density nozzle flows should be considered when the measured rotational temperatures are used to infer translational temperatures in the gas. Previous work,<sup>26, 27</sup> relating to rotational nonequilibrium in free jets of nitrogen expanding from room temperature, has indicated that the point at which rotational freezing occurs can be predicted approximately by assuming a "sudden-freezing criterion" of the form

$$\left| \frac{DT}{Dt} \right| = \frac{1}{2} \frac{T \nu_{col}}{Z_r} ; \quad (10)$$

so that, for steady one-dimensional flow near the axis, the rotational degrees of freedom can be considered in equilibrium if

$$u \left| \frac{dT}{dz} \right| < \frac{T \nu_{col}}{2 Z_r} . \quad (11)$$

Here,  $u$  is the local flow velocity,  $\nu_{col}$  the molecular collision frequency,  $Z_r$  the rotational collision number, and  $T$  the equilibrium temperature calculated by neglecting relaxation effects. The factor of  $1/2$ , which has been included, enables Eq. (10) to correctly predict the onset of rotational freezing observed<sup>10</sup> in free jets. A value of  $Z_r = 5$ , in agreement with ultrasonic absorption experiments<sup>28, 29</sup> and shock wave data<sup>13</sup> for room-temperature nitrogen, has been used here for the rotational collision number.

For nozzle flows the inequality (11) can be rewritten as

$$M \frac{\rho_0}{\rho} \frac{\Omega_0}{\Omega} \left| \frac{d \ln (T/T_0)}{d(z/r_*)} \right| < \frac{5}{8\gamma} \sqrt{\frac{\gamma-1}{2}} \frac{B}{Z_r}, \quad (12)$$

where  $M$  is the local Mach number and the  $\Omega$ 's are slowly varying functions<sup>30</sup> of temperature, describing the deviation of viscosity cross-sections from rigid-sphere cross-sections.

Equation (12) can now be applied to the experimental conditions of the present program to test for the possibility of rotational freezing in the expansions, provided the equilibrium temperatures can be estimated. These are, of course, different from the measured temperature if rotational freezing occurs. If the isentropic curve in Fig. 19 is used to define the temperature gradients, then Eq. (12) indicates the possibility of rotational freezing for  $B < 300$ . This is too severe a test, however, because the actual gradients in the equilibrium temperature are bound to be less than the inviscid gradients.

A more realistic procedure is based on calculating approximate equilibrium temperatures from the measured densities by means of the isentropic law. This method provides a valid test, as can be seen by inspecting the entropic equation of state, a differential form of which is

$$\frac{d \ln T/T_0}{dz} = (\gamma - 1) \left[ \frac{d \ln (\rho/\rho_0)}{dz} + \frac{1}{R} \frac{dS}{dz} \right]. \quad (13)$$

In the expansion, temperature and density gradients are both negative, whereas the entropy gradient,  $dS/dz$ , is positive. Hence, for a given density gradient, the absolute value of the temperature gradient becomes smaller the more entropy there is produced along unit length of streamline. Neglect of the entropy production term, therefore, tends to overestimate the magnitude of the temperature gradient, so that this method provides a conservative test for a possible rotational nonequilibrium. Tests, based on the use of Eq. (13) with  $dS = 0$  indicated that rotational freezing effects are negligible for any of the flows described here.

### 3. Centerline Densities and Pressures

Experimental centerline densities,  $\rho_c$ , corresponding to conditions discussed in Fig. 19 are given in Fig. 21. Again, there is evidence of two



different types of behavior. Densities for  $B > 500$  decrease in the expected manner (note theoretical curve for  $B = 1230$ ) at a slower rate than predicted by inviscid theory. For  $B < 200$  the negative density gradient is considerably steeper and exceeds the inviscid gradient near the nozzle exit. That densities should drop more rapidly in a more viscous flow can be understood by rewriting Eq. (13) in the form

$$\frac{dS}{d(z/r_*)} = \frac{R}{\gamma-1} \left[ \frac{d \ln(p/p_0)}{d(z/r_*)} - \gamma \frac{d \ln(\rho/\rho_0)}{d(z/r_*)} \right]. \quad (14)$$

The rate of entropy production along the centerline can be expected to be greater the lower the Reynolds number because of the increased viscous effects. Equation (14), therefore, predicts that for comparable pressure gradients the density has to decrease faster at the lower Reynolds numbers.

For  $B = 590$ , density measurements were obtained with the 2.5 mm nozzle as well as with the 5 mm nozzle (Fig. 21), and the experimental values of  $\rho_c/\rho_0$  were found to be independent of nozzle size and nozzle pressure ratio ( $p_0/p_\infty$ ). This confirms that the results scale with  $B$ , and that there is no pronounced difference in the flow when  $p_0/p_\infty$  is raised from 300 to 1200. The latter is an indication that the experimental observations apply also to nozzles exhausting into a complete vacuum ( $p_0/p_\infty \rightarrow \infty$ ).

All density measurements were obtained at points where the gas pressure was below 0.3 torr, and no corrections have been applied to compensate for possible collisional quenching of the electron beam luminescence. Density values measured near the throat for  $B = 590$  and 1230 may be approximately 10% low due to collisional quenching. Collisional quenching effects are considered negligible for all other values of  $B$ . Possible random errors in the centerline densities are also of the order of  $\pm 10\%$ , owing to the limited accuracy with which the beam currents were known (Section III).

Centerline pressures were derived from the measured temperatures and densities by making use of the equation of state for a perfect gas. These pressure curves (solid lines) are compared with theory (dotted lines) in Fig. 22. For the low Reynolds numbers the axial pressure profiles appear to converge to an asymptotic limit, at which the normalized pressures become independent of  $B$ . The full significance of this behavior

is not clear at this time. All measurements indicate, however, that this limit at  $B \leq 100$  represents a fully viscous, near-isothermal, subsonic, near-free-molecular duct flow.

#### 4. Off-Axis Measurements

Measured radial density profiles at four different Reynolds numbers and at various axial positions are displayed in Figs. 23 to 26. Experimental densities have been made dimensionless through division by the centerline density at each particular axial position,  $z/r_*$ . Radial distance,  $r$ , is measured in units of the radial distance to the wall,  $r_w$ . At Reynolds numbers of  $B = 110$  (Fig. 23) and  $B = 175$  (Fig. 24) the normalized density profiles are approximately independent of axial position. For the density profiles to be similar in this manner, it is required that at every cross-section  $d \ln(\rho/\rho_0)/d(z/r_*)$  is approximately the same for all streamlines. If the pressure profiles are assumed to be similar as well (certainly true in the slender-channel approximation), then it is evident from Eq. (14) that the rate of entropy production along streamlines is nearly constant over each cross-section. This may be used as a definition of a "fully viscous" flow. For  $B = 110$  the wall densities are approximately 60% of the centerline densities. The corresponding value for  $B = 175$  is 45%.

In contrast to the behavior observed at very low Reynolds numbers, the radial density profiles for  $B = 590$  display a marked dissimilarity (Fig. 25). Near the throat at  $z/r_* = 3.7$  a small inviscid core exists in this case. This inviscid core, however, shrinks to zero by the time the flow reaches the nozzle exit. Here the entropy production along the centerline is only significant near the exit of the nozzle. In contrast, the entropy production along a streamline near the wall is important throughout the length of the nozzle. For similar pressure histories along each streamline, Eq. (14) then predicts that the density at the center should decrease at a slower rate than the density near the wall. This produces dissimilar density profiles in agreement with the observed ones.

Two of the density profiles for  $B = 590$  have been determined with two different nozzles (Fig. 15). At  $z/r_* = 13.7$ , the profile obtained in the 5 mm nozzle (solid curve) is identical with that obtained in the 2.5 mm nozzle (broken curve) when allowance is made for the difference in spatial resolution (Fig. 25). The corresponding profiles at  $z/r_* = 3.7$ , however, show a discrepancy, which cannot be entirely explained by the difference in spatial resolution. It is believed that the discrepancy arises from small differences in the wall contours at the throat for the two nozzles. Since the throat regions were difficult to machine, and since the wall curvature at the throats could not be measured accurately, it is possible that the longitudinal throat radii of the nozzles were not similar.

Experimental and theoretical density profiles shown in Fig. 26 indicate that, at Reynolds numbers above 1000, an inviscid core persists to the nozzle exit. The theoretical curves have been obtained with a computer program based on the slender-channel formulation<sup>6</sup>. At an axial position of  $z = 8.7r_*$ , the theoretical and experimental density profiles show good agreement. At this position, most of the discrepancy between theory and experiment can be explained by the finite spatial resolution of the experimental measurements. Significant differences between the theoretical and experimental profiles exist, however, at other values of  $z/r_*$ . This is an indication that not all peculiarities of low-density nozzle flows are fully taken into account by the theory.

The experimental profile nearest the throat exhibits a density ridge near  $r/r_w = 0.5$ , where the measured density is higher than on the axis (Fig. 26). The density hump may indicate a weak compression wave originating at the throat. This interpretation is supported by the recent observation<sup>31</sup> of internal shock waves in high-pressure conical nozzles with circular-arc throats. At low densities such shock waves would not be expected, but it is possible that a viscous compression wave may be generated at a point where the wall curvature changes too abruptly.

For a limited number of experimental tests, performed in the 5 mm nozzle, static temperatures were determined at off-axis points as well as on

the centerline. The measured temperatures increase monotonically from the centerline value to a gas temperature at the wall which is approximately  $0.8 T_0$  (Fig. 27). This value is in agreement with predictions made by Rae<sup>6</sup> for an adiabatic wall with slip at the boundary. The radial temperature profile for  $B = 175$  (Fig. 27) provides evidence for the near-isothermal character of the flow at very low Reynolds numbers.

Pressures calculated from the experimental temperatures and densities are given in Fig. 28 for  $B = 590$  and  $B = 175$  and at a position  $z = 13.7 r_{*}$ . The normalized temperature profiles are not the exact inverse of the corresponding normalized density profiles, so that the derived pressures are not constant across the flow. In fact, the observed wall pressures are 30% and 40% below the centerline pressures for  $B = 590$  and  $B = 175$ , respectively. This suggests that the basic assumption of zero radial pressure gradients in the slender-channel theory should be revised in order to obtain a more accurate description of the flow.

It may be noted that the radial gradients of density, temperature and pressure do not vanish at the wall. Because the radial coordinate makes an angle of  $20^\circ$  with respect to the normal to the boundary, small negative radial gradients are expected near the wall corresponding to the radial components of the tangential gradients. The radial pressure gradient observed at the wall (Figs. 28 and 29) is consistent with a zero normal pressure gradient. However, the data indicate that there exist nonzero density and temperature gradients in a direction normal to the "adiabatic" wall. This confirms the noncontinuum character of the flow in this Reynolds number regime. The exact density gradients at the wall could not be determined because of the finite spatial resolution of the measurements (horizontal bars in Figs. 23 to 26).

Normalized profiles of density, temperature and pressure obtained at a position close to the nozzle exit are consistent with those determined further upstream. For a Reynolds number of 590 and a nozzle pressure ratio of 310 (Fig. 29), the wall pressure near the nozzle lip is 35% below the axial pressure. It is of interest here that the jet plume for this particular flow was the least underexpanded one of this experimental series. At

the exit, the ambient pressure,  $p_\infty$ , was below the pressure at the center but was above the pressure at the wall. The observed radial pressure distribution is thus evidently not caused by the low ambient pressure, but may have to be considered a characteristic feature of low-Reynolds-number expansions in nozzles. To check for possible flow separation in this case, the gas properties near the wall were determined along the length of the expansion cone (Fig. 30). No evidence of flow separation was detected.

## 5. Effects of Ambient Pressure

Microthrust nozzles find applications in free space, yet have to be tested and flight-rated in the laboratory. Unless a space simulation chamber with an enormous pumping capacity is available, it is difficult to maintain a high vacuum, when even a small steady mass flow ( $10^{-1}$  to  $10^{-3}$  g/s) must be accommodated. It is therefore of interest to determine how low-density nozzle flows are affected by non-zero ambient pressures, and how low this pressure has to be for effective space simulation to be possible. At high Reynolds numbers ( $> 10^5$ ) the supersonic portion of the flow fills almost the entire cross-sectional area at the exit, apart from a thin boundary layer, and the flow in the nozzle and in parts of the plume is effectively isolated from the ambient conditions by shock waves originating at the nozzle lip. Under these conditions the internal flow remains undisturbed, whether the flow is highly underexpanded or slightly overexpanded. However, at low Reynolds numbers the supersonic region is often restricted to a narrow core, and external conditions are able to influence the internal flow through the thick subsonic boundary layer.

A brief survey of this problem was conducted by flow visualization of external plumes and by sample temperature measurements in the nozzle and in the plume. For a given Reynolds number, different pressure ratios,  $p_o/p_\infty$ , were obtained by keeping  $p_o$  constant and changing  $p_\infty$ . The ambient pressure was varied by throttling the booster pump of the tunnel. A series of photographs obtained with the 5 mm nozzle and showing the plume structure for different nozzle pressure-ratios is reproduced in

Fig. 31. The flow was made visible by the method discussed in Section III. Regions of high luminosity represent regions of relatively high gas density. The nozzle is at the right, and the flow is from right to left. The external and internal diameters at the nozzle mouth are 48 mm and 42 mm, respectively. Figure 31A shows a slightly underexpanded jet obtained at  $B = 450$  and  $p_o/p_\infty = 310$ . There is very little structure in this jet. The flow fills the whole nozzle, and the density in the plume drops off gradually in all directions. This type of flow field is representative of all the flows discussed earlier for which temperatures and densities were determined.

At a Reynolds number of  $B = 1550$ , a nozzle pressure ratio of approximately 300 is no longer sufficient to produce an underexpanded plume (Fig. 31B). Here, the relatively high ambient pressure ( $28 \mu\text{Hg}$ ) has caused flow separation inside the nozzle. The supersonic core is enveloped by a barrel-shaped shock wave, which originates in the expansion cone of the nozzle. As seen from the beam luminosity, the region surrounding the barrel shock appears to be occupied by stagnant gas at the ambient pressure. As the ambient pressure is increased ( $p_o/p_\infty$  decreased), the point of flow separation moves further upstream in the nozzle (Fig. 31C and D), and the plume shows a repetitive pattern of expansion diamonds, which shrink in size as  $p_o/p_\infty$  decreases. In Fig. 31D the first diamond is entirely within the nozzle. The work of Love et al.<sup>21</sup> has shown that this pattern of expansion diamonds occurs only when the jet pressure at the plume origin is less than twice the ambient pressure. Hence, it is concluded that, for cases shown in Figs. 31B to 31D, flow separation occurs at a point where the static pressure in the flow has dropped to a value of approximately  $2p_\infty$ . From this point on the presence of the nozzle wall is superfluous and has no influence on the jet plume, since the flow does not follow it.

To obtain more quantitative data of the observed plume configurations, density profiles were recorded for selected positions in two plumes of distinctly different structure. In Figs. 32 and 33 these density

profiles have been arranged in the proper sequence and in line with corresponding positions in a photographic record of the same jets. For both jets the nozzle pressure ratio is just over 300.

At a Reynolds number of 590 (Fig. 32) the jet is underexpanded with respect to the centerline pressure, but slightly overexpanded with respect to the wall pressure at the exit. Nevertheless, there exists no evidence of any shock waves in this plume, and the recorded density profiles have a single peak, which decreases with downstream distance,  $z'$ , from the nozzle mouth ( $z' = 0$ ). These profiles form a consistent extension of the density cross-sections determined just inside the nozzle (Fig. 25).

At a Reynolds number of 1550 (Fig. 33), the density profiles in the plume are doubly peaked and indicate the presence of a barrel-shaped shock, which is representative of an underexpanded free jet (compare with Fig. 13). This barrel shock converges to a single density peak at  $z' = 24r_*$ , where the centerline density is more than twice the density at the nozzle exit (see axial density profile above photograph in Fig. 33). This particular plume has already been discussed in connection with Fig. 31B and is typical of the jets for which high back pressure has caused separation inside the nozzle. It may be noted that in this case the ambient pressure is above the centerline pressure at the exit. Because of the thick subsonic boundary layer there apparently exists no way in which these low-density jets can be overexpanded in the conventional sense. As soon as the ambient pressure exceeds the jet pressure at the nozzle exit, back-pressure effects cause flow separation inside the nozzle to produce a slightly underexpanded free jet with the characteristic barrel-shock configuration. Such barrel shocks have also been observed inside nozzles by Yevseyev<sup>3</sup> under similar conditions.

It has been demonstrated here, that the maximum nozzle pressure ratio,  $p_0/p_\infty$ , which can be achieved in a given low-density facility, is of prime importance for the testing of microthrust nozzles operating in the low-Reynolds number regime. For the tunnel described in Sec. III, 1 and for the nozzles tested here, these maximum pressure ratios have been

plotted as a function of  $B$  in Fig. 34. The advantage of decreasing the nozzle size to obtain higher pressure ratios is immediately evident. A decrease of the throat diameter by a factor of  $1/2$  increases the maximum pressure ratio by a factor of four at a specified Reynolds number.

Besides showing the "external" pressure ratio,  $p_o/p_\infty$ , for the two nozzles, Fig. 34 also gives the experimentally determined "internal" pressure ratios,  $(p_o/p_w)_{EXIT}$  and  $(p_o/p_c)_{EXIT}$ , where  $p_w$  and  $p_c$  represent gas pressures at the wall and on the center of the jet, respectively. Note that these two quantities, measured with two different nozzles and at different values of  $p_o/p_\infty$ , fall on two separate but continuous curves. This gives additional support to the previous observation, that the internal gas pressures near the exit are not affected by the ambient conditions as long as the plume is underexpanded, and that under these conditions the wall pressure at the exit is up to 40% lower than the centerline pressure. Truly underexpanded conditions can be achieved with the 5 mm nozzle only for  $B < 350$ , whereas the 2.5 mm nozzle can be operated at underexpanded pressure ratios up to  $B \approx 2000$ .

Flow-visualization photographs (Figs. 35 A, B, C) of plumes produced by the 2.5 mm nozzle with high nozzle pressure ratios ( $p_o/p_\infty \approx 1000$ ) exhibit again the rather featureless "supersonic" underexpanded plumes, which are quite different from those studied by Love et al.<sup>21</sup> at higher Reynolds numbers. (The lengths of the photographs represent an actual distance of 11.5 cm). The Reynolds number ( $B = 1230$ ) and pressure ratio ( $p_o/p_\infty = 190$ ) for the plume in Fig. 35D are similar to conditions for the jet in Fig. 31C, which was obtained with the 5 mm nozzle. Accordingly, the plumes of these two jets are also very similar, both showing flow separation well inside the nozzle.

When the centerline temperature near the nozzle exit ( $T_E$ ) is monitored as a function of  $p_o/p_\infty$ , the behavior shown in Fig. 36 is observed. The point of observation, E, lay one throat diameter downstream of the nozzle exit. The lower curve in Fig. 36 was obtained at a nozzle Reynolds number of 590. In the region where the plume is underexpanded with respect to the centerline pressure at the exit ( $p_o/p_\infty > 200$ ), no change



in  $T_E$  is observed when  $p_o/p_\infty$  is changed from 1000 to 200. In this range of pressure ratios, the ambient pressure has, therefore, little or no influence on the expansion in the nozzle. As  $p_o/p_\infty$  is decreased further, however,  $T_E$  rises and falls in a cyclic manner, which correlates with the observed plume patterns described above. As the ambient pressure rises, the shrinking diamond pattern moves through the point E. At A this point lies within the first diamond; at B and C it lies inside the second and third expansion cells, respectively. Eventually, as  $p_o/p_\infty$  approaches unity, the flow remains subsonic throughout the nozzle, and  $T_E$  approaches  $T_o$ .

This cyclic behavior is not observed in the fully viscous flow regime. At  $B = 175$  the exit temperature increases monotonically as  $p_o/p_\infty$  is decreased from  $10^3$  to below 10. Most of the change occurs for pressure ratios between  $10^2$  and 10. However, even for underexpanded pressure ratios ( $p_o/p_\infty > 200$ ) a possible small variation of  $T_E$  with  $p_o/p_\infty$  was observed for the two different nozzles. These measurements indicate that there exists a possible upstream influence due to the ambient pressure at very low Reynolds numbers. To investigate this upstream influence, axial temperatures were measured throughout the nozzle at several pressure ratios.

For  $B = 175$  such measurements were performed for pressure ratios ranging over more than an order of magnitude from 90 to 930 (Fig. 37). Most of the adjustment in the axial temperatures, over the "underexpanded" range of pressure ratios, was found to take place outside the nozzle; although some influence is observed at points which lie several molecular mean free paths inside the nozzle. The fundamental shape of the temperature curve remains unaltered, however, so that the profiles in Fig. 19 can indeed be considered as representative for the entire underexpanded range. No measurable change in any of the centerline temperatures was observed for  $B = 590$  as  $p_o/p_\infty$  was varied by a factor of four (Fig. 37).

## 6. Discharge Coefficients

Measured mass flow rates were used to calculate discharge coefficients,  $C_D$ , for the nozzles and flow conditions studied. The discharge

coefficient for a nozzle is defined as the actual mass flow divided by the ideal inviscid mass flow. The values of  $C_D$  obtained are plotted as a function of  $B$  in Fig. 38. These range from 0.9 at  $B = 1000$  to approximately 0.75 at  $B = 100$ . In addition to the present values, the diagram also contains discharge coefficients predicted by Rae<sup>6</sup> and previous experimental values by Massier et al.<sup>2</sup> and by Milligan<sup>1</sup>. There exists an approximate agreement among the data. Specific comparisons are not possible, however, because the nozzle configurations and operating conditions were all different. Table 2 lists the significant parameters which are necessary to define the nozzle geometry and flow conditions. Besides throat diameter, Reynolds number, and pressure ratio, this table specifies wall angles for the subsonic and supersonic sections,  $\theta_1$  and  $\theta_2$ , the longitudinal radius of curvature,  $r_L$ , at the throat, and the maximum area ratio,  $A_E/A_*$ , in the supersonic expansion cone.

It should be noted that previous experimental data were obtained at relatively small wall angles ( $\theta_2 = 10^\circ$ ) and at very low pressure ratios. The pressure ratio for a choked nozzle flow is not expected to affect  $C_D$  at large Reynolds numbers. At  $B < 500$ , however, some influence of  $p_o/p_\infty$  on  $C_D$  would be expected. The deviation of the present data from Milligan's measurements may well be due to the difference in the experimental pressure ratios.

## V. SUMMARY

The electron-beam technique has been extended to the study of internal nozzle flows at Reynolds numbers between 100 and 1500. Point measurements of gas temperature and density were made in nozzles which have a relatively sharp throat and a conical supersonic section with a  $20^\circ$  wall angle. The expanding flows were found to exhibit two different types of behavior, each characteristic of a particular Reynolds number range.

For  $B > 500$  a small inviscid core was found to exist in the flow. This core extends to the nozzle exit at Reynolds numbers approaching 1000. In this range of  $B$ , centerline temperatures decrease monotonically from the throat to the exit, and the axial density and pressure gradients become less steep with lower Reynolds number. Radial density profiles are dissimilar along the length of the nozzle, because the rate of entropy production is less near the axis than it is near the wall.

For  $B < 300$  the flow is fully viscous with no indication of any isentropic core. Centerline temperatures first decrease, but then increase again towards the nozzle exit. The increase in temperature is brought about through conversion of directed flow energy into thermal energy by the action of the viscous shear stresses. Density and pressure, however, decrease in the region where the temperature rises. In fact, at these values of  $B$ , the centerline densities fall off faster with distance than they do at higher Reynolds numbers. Owing to the uniform production of entropy across the flow, the radial density profiles are approximately similar throughout the nozzle. Normalized axial pressure profiles appear to become independent of  $B$  for Reynolds numbers below 100. For  $B \approx 100$ , temperatures measured at the exit indicate subsonic flow, even though supersonic flow exists further upstream. This substantiates the prediction by Rae<sup>6</sup> of a supersonic "bubble" embedded in the expanding flow at this Reynolds number.

Over the entire Reynolds number range studied, significant negative radial pressure gradients were found to exist throughout the nozzle. Under conditions for which the flow near the exit is underexpanded, these gradients

are believed to be insensitive to ambient pressure levels. At  $B = 600$ , experimental wall pressures are approximately 30% lower than pressures near the axis, whereas at Reynolds numbers near 100 the wall pressures are 40% lower. This feature should be taken into account when formulating a new improved version of the theory.

A survey of ambient-pressure effects on the flow in the nozzle showed that flow separation occurs well upstream of the nozzle exit when the external pressure exceeds the static jet pressure near the exit. Under these conditions, the plume resembles that of a slightly underexpanded free jet originating at the point of separation in the expansion cone of the nozzle. When the ambient pressure is less than the nozzle exit pressure, however, the gas properties along the centerline appear to be insensitive to changes in the back pressure. Nozzles destined for space operation must be tested at sufficiently low ambient pressure to ensure underexpanded exit conditions. For  $B < 300$  extremely low ambient pressures may be necessary to eliminate all back-pressure effects.

The experiments discussed here have produced a significant gain in the understanding of viscous flows in nozzles and ducts. Predictions of the slender-channel theory have been substantiated experimentally, and suggestions for improving the theory have been made.

The development of an accurate theory is essential for the optimization of microthrusters, since a much wider range of nozzle geometries and flow conditions can be studied by theory than is practical experimentally. Nevertheless, additional experimental work is warranted in which the effects of different nozzle geometry (wall angle, throat roundness, nozzle length) on the flow are determined. The variations produced in nozzle performance by different gases, by heated or cooled walls, by wall transpiration, by radial swirl, or by species diffusion are also of practical interest.

## REFERENCES

1. Milligan, M. W., "Nozzle Characteristics in the Transition Regime between Continuum and Free Molecular Flow", AIAA Journal, Vol. 2, No. 6, June 1964, pp. 1088-1092.
2. Massier, P. F., Back, L. H., Noel, M. B. and Saheli, F., "Viscous Effects on the Flow Coefficient for a Supersonic Nozzle", AIAA Journal, Vol. 8, No. 3, March 1970, pp. 605-607.
3. Yevseyev, G. A., "Experimental Investigation of Flow of Rarefied Gas", AN SSSR. Izvestiya. Mekhanika, Moscow 1965, No. 3, pp. 165-172. Machine Translation in AF Foreign Technology Div. MT-67-22, March 31, 1967, AD 662502.
4. Sutherland, G. S. and Maes, M. E., "A Review of Microrocket Technology:  $10^{-6}$  to 1 lbf Thrust", Journal of Spacecraft and Rockets, Vol. 3, No. 8, Aug. 1966, pp. 1153-1165.
5. Williams, J. C., "Viscous Compressible and Incompressible Flow in Slender Channels", AIAA Journal, Vol. 1, No. 1, Jan. 1963, pp. 186-195.
6. Rae, W. J., "Some Numerical Results on Viscous Low-Density Nozzle Flows in the Slender-Channel Approximation", AIAA Paper No. 69-654, June 1969, AIAA Fluid and Plasma Dynamics Conf., San Francisco, Calif.; also "Final Report on a Study of Low-Density Nozzle Flows, with Application to Microthrust Rockets", CAL Tech. Report No. AI-2590-A-1, Dec. 1969, Cornell Aeronautical Lab., Inc., Buffalo, New York.
7. Schumacher, B. W. and Gadamer, E. O., "Electron Beam Fluorescence Probe for Measuring the Local Gas Density in a Wide Field of Observation", Canadian Journal of Physics, Vol. 36, No. 6, June 1958, pp. 659-671.

8. Muntz, E. P., "Static Temperature Measurements in a Flowing Gas", The Physics of Fluids, Vol. 5, No. 1, Jan. 1962, pp. 80-90.
9. Robben, F. and Talbot, L., "Measurements of Rotational Temperatures in a Low Density Wind Tunnel", The Physics of Fluids, Vol. 9, No. 4, April 1966, pp. 644-652.
10. Marrone, P. V., "Temperature and Density Measurements in Free Jets and Shock Waves", The Physics of Fluids, Vol. 10, No. 3, March 1967, pp. 521-538.
11. Ashkenas, H., "Rotational Temperature Measurements in Electron-Beam Excited Nitrogen", The Physics of Fluids, Vol. 10, No. 12, Dec. 1967, pp. 2509-2520.
12. Petrie, S. L. and Boiarski, A. A., "The Electron Beam Diagnostic Technique for Rarefied Flows at Low Static Temperatures", Proceedings of the Sixth International Symposium on Rarefied Gas Dynamics, edited by L. Trilling and H. Y. Wachman, Vol. II, Academic Press, New York, 1969, pp. 1685-1701.
13. Robben, F. and Talbot, L., "Experimental Study of the Rotational Distribution Function of Nitrogen in a Shock Wave", The Physics of Fluids, Vol. 9, No. 4, April 1966, pp. 653-662.
14. Polyakova, G. N., Fogel, Ya. M. and Zats, A. V., "Rotational and Vibrational Energy Level Distributions of  $N_2^+$  Ions Produced in Collisions between Electrons and Nitrogen Molecules", Soviet Physics JETP, Vol. 25, No. 6, Dec. 1967, pp. 993-997; translated from J. Exptl. Theoret. Phys. (U.S.S.R.) Vol. 52, June 1967, pp. 1495-1503.
15. Harbour, P. J., Bienkowski, G. K. and Smith, R. B., "Influence of Secondary Electrons on an Electron-Beam Probe", The Physics of Fluids, Vol. 11, No. 4, April 1968, pp. 800-803.

16. Herzberg, G., "Molecular Spectra and Molecular Structure", Vol. I, "Spectra of Diatomic Molecules", Van Nostrand, Princeton, New Jersey, 1950.
17. Rothe, D.E. and McCaa, D.J., "Emission Spectra of Molecular Gases Excited by 10 keV Electrons", CAL Tech. Report No. 165, Dec. 1968, Cornell Aeronautical Laboratory, Inc., Buffalo, New York.  
  
also  
  
McCaa, D.J. and Rothe, D.E., "Emission Spectra of Atmospheric Gases Excited by an Electron Beam", AIAA Journal, Vol. 7, No. 8, Aug. 1969, pp. 1648-1651.
18. Petrie, S.L., "Excitation of the Second Positive System of Molecular Nitrogen by Fast Electrons", CAL Tech. Report No. AG-2258-A-1, Jan. 1969, Cornell Aeronautical Laboratory, Inc., Buffalo, New York.
19. Rothe, D.E., "Flow-Visualization Using a Traversing Electron Beam", AIAA Journal, Vol. 3, No. 10, Oct. 1965, pp. 1945-1946.
20. Owen, P.L. and Thornhill, G.K., "The Flow in an Axially Symmetric Supersonic Jet from a Nearly-Sonic Orifice into a Vacuum", R. & M. 2612, Sept. 1948, Aeronautical Research Council, United Kingdom.
21. Love, E.S., Grigsby, C.E., Lee, L.P. and Woodling, M.J., "Experimental and Theoretical Studies of Axisymmetric Free Jets", NASA Tech. Report R-6, 1959.
22. Bier, K. and Schmidt, B., "Zur Form der Verdichtungsstösse in frei expandierenden Gasstrahlen", Zeitschrift für angewandte Physik, Vol. 13, 1961, pp. 493-500.
23. Ashkenas, H. and Sherman, F.S., "The Structure and Utilization of Supersonic Free Jets in Low Density Wind Tunnels", Proceedings of the Fourth International Symposium on Rarefied Gas Dynamics, edited by J.H. deLeeuw, Vol. II, Academic Press, New York, 1966, pp. 84-105.

24. Rothe, D. E., "Electron Beam Studies of the Diffusive Separation of Helium-Argon Mixtures", *The Physics of Fluids*, Vol. 9, No. 9, Sept. 1966, pp. 1643-1658;
- also
- Rothe, D. E., "Electron Beam Studies of the Diffusive Separation of Helium-Argon Mixtures in Free Jets and Shock Waves", UTIAS Report No. 114, July 1966, University of Toronto, Toronto, Canada.
25. Brocklehurst, B. and Downing, F. A., "Mechanisms of Excitation of Luminescence in Nitrogen Gas by Fast Electrons", *Journal of Chemical Physics*, Vol. 46, No. 8, April 1967, pp. 2976-2991.
26. Knuth, E. L., "Rotational and Translational Relaxation Effects in Low-Density Hypersonic Free Jets", UCLA Report No. 64-53, Nov. 1964, University of California, Los Angeles, California.
27. Lefkowitz, B. and Knuth, E. L., "A Study of Rotational Relaxation in a Low-Density Hypersonic Free Jet by Means of Impact-Pressure Measurements", *Proceedings of the Sixth International Symposium on Rarefied Gas Dynamics*, edited by L. Trilling and H. Y. Wachman, Vol. II, Academic Press, New York, 1969, pp. 1421-1438.
28. Winter, T. G. and Hill, G. L., "High-Temperature Ultrasonic Measurements of Rotational Relaxation in Hydrogen, Deuterium, Nitrogen and Oxygen", *Journal of the Acoustical Society of America*, Vol. 42, No. 4, April 1967, pp. 848-858.
29. Carnevale, E. H., Carey, C. and Larson, G., "Ultrasonic Determination of Rotational Collision Numbers and Vibrational Relaxation Times of Polyatomic Gases at High Temperatures", *Journal of Chemical Physics*, Vol. 47, No. 8, Oct. 1967, pp. 2829-2835.
30. Hirschfelder, J. O., Curtiss, C. F. and Bird, R. B., "Molecular Theory of Gases and Liquids", John Wiley and Sons, New York, 1954, Chapters 8 and 9.
31. Back, L. H. and Cuffel, R. F., "Detection of Oblique Shocks in a Conical Nozzle with a Circular-Arc Throat", *AIAA Journal*, Vol. 4, No. 12, Dec. 1966, pp. 2219-2221.



Table I

TABLE VALUES = LOG(10) OF  $2 \times K \times G \times (\text{LAMBD AO} / \text{LAMBD A})^{**4}$  FOR THE R-BRANCH OF THE (0,0)-BAND OF THE FIRST NEGATIVE SYSTEM OF N<sub>2</sub><sup>+</sup>  
 K=QUANTUM NUMBER LAMBD AO=3909.71 ANGSTROMS  
 $G = (1/(K+1) \times \exp(-2 \times (K+1) \times \text{THETAR/TR}) + K \times \exp(2 \times K \times \text{THETAR/TR})) / (1/2 \times (K+1))$   
 THETAR=2.87 (ROTATIONAL CONSTANT FOR THE GROUND STATE--DEG K) TR=ROTATIONAL TEMPERATURE (DEG K)

K	K*(K+1)	TR=	2	4	6	8	10	12	14	16	18	20	22	24	26
1	2		1.0705	0.4587	0.2860	0.2263	0.2059	0.2008	0.2013	3.2055	0.2100	0.2147	0.2192	0.2236	0.2276
2	6		2.6973	1.4513	1.0408	0.8453	0.6757	0.5757	0.6372	3.6128	0.5959	0.5863	0.5793	0.5746	0.5715
3	12		4.1501	2.2805	1.6579	1.3494	1.1689	1.0539	0.9765	3.9228	0.8843	0.8562	0.8352	0.8193	0.8071
4	20		5.5376	3.0447	2.2139	1.7991	1.5521	1.3901	1.2775	1.1961	1.1356	1.0890	1.0541	1.0262	1.0041
5	30		6.8910	3.7750	2.7363	2.2171	1.9063	1.7003	1.5479	1.4479	1.3667	1.3038	1.2541	1.2143	1.1820
6	42		8.2236	4.4844	3.2380	2.6143	2.2411	1.9925	1.8159	1.6847	1.5840	1.5049	1.4417	1.3904	1.3482
7	56		9.5422	5.1797	3.7256	2.9985	2.5623	2.2718	2.0647	1.9102	1.7908	1.6964	1.6202	1.5574	1.5061
8	72		10.8507	5.8650	4.2031	3.3722	2.8736	2.5414	2.3043	2.1268	1.9894	1.8802	1.7916	1.7186	1.6576
9	90		12.1516	6.5427	4.6730	3.7382	3.1773	2.8035	2.5355	2.3355	2.1813	2.0576	1.9569	1.8737	1.8039
10	110		13.4465	7.2144	5.1370	4.0983	3.4751	3.0597	2.7630	2.5406	2.3678	2.2299	2.1174	2.0241	1.9457
11	132		14.7367	7.8814	5.5963	4.4537	3.7682	3.3112	2.9847	2.7400	2.5498	2.3977	2.2736	2.1705	2.0836
12	156		16.0230	8.5444	6.0516	4.8052	4.0573	3.5588	3.2025	2.9356	2.7280	2.5620	2.4263	2.3135	2.2183
13	182		17.3061	9.2043	6.5037	5.1534	4.3432	3.8031	3.4173	3.1280	2.9030	2.7231	2.5760	2.4536	2.3502
14	210		18.5864	9.8614	6.9531	5.4983	4.6264	4.0447	3.6293	3.3177	3.0754	2.8815	2.7230	2.5910	2.4795
15	240		19.8643	10.5161	7.4001	5.8420	4.9072	4.2843	3.8389	3.5050	3.2454	3.0377	2.8678	2.7263	2.6066
16	272		21.1402	11.1688	7.8450	6.1831	5.1860	4.5212	4.0464	3.6903	3.4133	3.1918	3.0105	2.8595	2.7318
17	306		22.4144	11.8198	8.2882	6.5225	4.7567	4.2522	3.8738	3.5341	3.2595	3.0341	2.8441	2.6910	2.5538
18	342		23.6869	12.4691	8.7298	6.8602	5.1384	4.5906	4.1564	3.8058	3.4742	3.2449	3.0090	2.8420	2.7073
19	380		24.9581	13.1171	9.1701	7.1965	5.2231	4.9306	4.4592	4.0558	3.7074	3.4643	3.2290	3.0496	2.9078
20	420		26.2281	13.7638	9.6091	7.5317	5.4543	4.8603	4.6156	4.2363	3.9074	3.6443	3.4258	3.2470	3.0978
21	462		27.4969	14.4094	10.0469	7.8657	5.6844	5.2231	4.8603	4.4156	4.0594	3.7924	3.5658	3.3770	3.2172
								5.6844	5.0612	4.5938	4.2303	3.9394	3.7015	3.5032	3.3354

K	K*(K+1)	TR=	28	30	32	34	36	38	40	42	44	46	48	50	55
1	2		0.2313	0.2347	0.2378	0.2407	0.2433	0.2458	0.2480	0.2501	0.2521	0.2539	0.2555	0.2571	0.2606
2	6		0.5695	0.5682	0.5675	0.5672	0.5671	0.5673	0.5676	0.5680	0.5685	0.5690	0.5695	0.5701	0.5716
3	12		0.7976	0.7902	0.7843	0.7797	0.7759	0.7729	0.7705	0.7685	0.7669	0.7656	0.7645	0.7637	0.7622
4	20		0.9863	0.9718	0.9600	0.9502	0.9420	0.9352	0.9294	0.9245	0.9204	0.9168	0.9138	0.9111	0.9060
5	30		1.1555	1.1337	1.1154	1.1001	1.0871	1.0760	1.0665	1.0584	1.0513	1.0452	1.0398	1.0351	1.0256
6	42		1.3132	1.2839	1.2591	1.2381	1.2201	1.2046	1.1911	1.1795	1.1693	1.1603	1.1524	1.1454	1.1311
7	56		1.4628	1.4262	1.3950	1.3682	1.3452	1.3251	1.3077	1.2923	1.2789	1.2670	1.2564	1.2470	1.2275
8	72		1.6053	1.5626	1.5251	1.4927	1.4645	1.4401	1.4185	1.3995	1.3827	1.3678	1.3545	1.3426	1.3178
9	90		1.7447	1.6942	1.6506	1.6127	1.5797	1.5507	1.5251	1.5025	1.4824	1.4644	1.4483	1.4338	1.4035
10	110		1.8790	1.8217	1.7722	1.7290	1.6912	1.6579	1.6283	1.6021	1.5786	1.5576	1.5388	1.5217	1.4859
11	132		2.0095	1.9459	1.8905	1.8422	1.7997	1.7621	1.7287	1.6989	1.6722	1.6482	1.6266	1.6070	1.5656
12	156		2.1371	2.0670	2.0060	1.9526	1.9055	1.8638	1.8265	1.7933	1.7634	1.7365	1.7122	1.6901	1.6431
13	182		2.2618	2.1854	2.1189	2.0605	2.0090	1.9632	1.9223	1.8857	1.8527	1.8228	1.7958	1.7713	1.7188
14	210		2.3841	2.3016	2.2296	2.1664	2.1104	2.0606	2.0161	1.9761	1.9401	1.9074	1.8778	1.8508	1.7930
15	240		2.5042	2.4156	2.3383	2.2702	2.2099	2.1562	2.1082	2.0649	2.0258	1.9904	1.9582	1.9288	1.8657
16	272		2.6225	2.5278	2.4451	2.3723	2.3079	2.2502	2.1986	2.1521	2.1101	2.0720	2.0372	2.0055	1.9371
17	306		2.7390	2.6383	2.5503	2.4728	2.4041	2.3427	2.2875	2.2380	2.1931	2.1522	2.1150	2.0809	2.0074
18	342		2.8541	2.7474	2.6541	2.5719	2.4990	2.4338	2.3753	2.3226	2.2748	2.2313	2.1916	2.1552	2.0767
19	380		2.9678	2.8551	2.7566	2.6697	2.5926	2.5237	2.4619	2.4060	2.3553	2.3092	2.2671	2.2285	2.1450
20	420		3.0803	2.9616	2.8579	2.7664	2.6851	2.6125	2.5472	2.4883	2.4348	2.3861	2.3416	2.3008	2.2123
21	462		3.1915	3.0671	2.9581	2.8620	2.7765	2.7002	2.6316	2.5696	2.5134	2.4621	2.4152	2.3722	2.2788

Table I (cont'd)

TABLE VALUES = LOG(10) OF  $2K \cdot G \cdot (L \cdot \lambda \cdot A \cdot D \cdot A \cdot O / \lambda \cdot M \cdot R \cdot U \cdot A) \cdot K \cdot K$  FOR THE R-BRANCH OF THE (0,0)-BAND OF THE FIRST NEGATIVE SYSTEM OF N<sub>2</sub><sup>+</sup>  
 K=QUANTUM NUMBER  $L \cdot \lambda \cdot M \cdot R \cdot U \cdot A = 3309.71$  ANGSTROMS  
 $G = ((K+1) \cdot \exp(-2 \cdot (K+1) \cdot \text{THE TAR/TR})) + K \cdot \exp(2 \cdot K \cdot \text{THE TAR/TR})) / (2 \cdot K + 1)$   
 $\text{THE TAR} = 2.97$  (ROTATIONAL CONSTANT FOR THE GROUND STATE--DEG K)  
 TR=ROTATIONAL TEMPERATURE (DEG K)

K	K*(K+1)	TR=	60	65	70	75	80	85	90	95	100	110	120	130	140
1	2		0.2636	0.2662	0.2684	0.2704	0.2722	0.2737	0.2751	0.2764	0.2776	0.2796	0.2813	0.2827	0.2840
2	6		0.5733	0.5744	0.5757	0.5769	0.5783	0.5791	0.5803	0.5810	0.5818	0.5833	0.5846	0.5858	0.5868
3	12		0.7614	0.7610	0.7609	0.7610	0.7612	0.7615	0.7618	0.7622	0.7625	0.7633	0.7640	0.7647	0.7654
4	20		0.9023	0.8997	0.8978	0.8964	0.8954	0.8947	0.8942	0.8938	0.8936	0.8933	0.8933	0.8934	0.8936
5	30		1.0136	1.0133	1.0093	1.0061	1.0036	1.0017	1.0002	0.9989	0.9979	0.9965	0.9955	0.9949	0.9945
6	42		1.1203	1.1120	1.1055	1.1003	1.0961	1.0928	1.0903	1.0878	1.0859	1.0830	1.0810	1.0795	1.0785
7	56		1.2126	1.2010	1.1917	1.1843	1.1783	1.1733	1.1692	1.1658	1.1629	1.1584	1.1552	1.1527	1.1508
8	72		1.2985	1.2833	1.2711	1.2612	1.2532	1.2465	1.2409	1.2362	1.2322	1.2260	1.2213	1.2177	1.2150
9	90		1.3797	1.3608	1.3456	1.3331	1.3229	1.3143	1.3071	1.3011	1.2959	1.2876	1.2814	1.2767	1.2730
10	110		1.4575	1.4348	1.4163	1.4012	1.3886	1.3781	1.3692	1.3617	1.3553	1.3449	1.3370	1.3309	1.3262
11	132		1.5326	1.5060	1.4843	1.4663	1.4514	1.4388	1.4282	1.4191	1.4113	1.3987	1.3891	1.3816	1.3757
12	156		1.6055	1.5750	1.5499	1.5292	1.5119	1.4971	1.4846	1.4739	1.4647	1.4497	1.4383	1.4293	1.4222
13	182		1.6766	1.6422	1.6138	1.5902	1.5703	1.5534	1.5391	1.5267	1.5160	1.4986	1.4852	1.4747	1.4663
14	210		1.7462	1.7079	1.6761	1.6496	1.6272	1.6081	1.5913	1.5778	1.5656	1.5457	1.5302	1.5181	1.5083
15	240		1.8144	1.7722	1.7371	1.7077	1.6823	1.6615	1.6433	1.6275	1.6138	1.5912	1.5737	1.5599	1.5487
16	272		1.8814	1.8354	1.7970	1.7647	1.7372	1.7137	1.6935	1.6760	1.6607	1.6355	1.6159	1.6003	1.5877
17	306		1.9473	1.8976	1.8559	1.8207	1.7937	1.7650	1.7235	1.7066	1.7066	1.6788	1.6569	1.6396	1.6255
18	342		2.0123	1.9588	1.9138	1.8758	1.8433	1.8153	1.7911	1.7701	1.7516	1.7211	1.6970	1.6778	1.6623
19	380		2.0763	2.0191	1.9710	1.9301	1.8951	1.8649	1.8389	1.8159	1.7959	1.7626	1.7363	1.7153	1.6981
20	420		2.1394	2.0786	2.0273	1.9837	1.9462	1.9138	1.8857	1.8611	1.8394	1.8034	1.7749	1.7519	1.7332
21	462		2.2019	2.1374	2.0830	2.0365	1.9966	1.9621	1.9320	1.9056	1.8824	1.8436	1.8128	1.7879	1.7676

K	K*(K+1)	TR=	150	160	170	180	190	200	210	220	230	240	250	260	270
1	2		0.2851	0.2860	0.2869	0.2875	0.2883	0.2889	0.2895	0.2900	0.2905	0.2909	0.2913	0.2917	0.2920
2	6		0.5877	0.5885	0.5892	0.5893	0.5904	0.5910	0.5915	0.5919	0.5923	0.5927	0.5931	0.5934	0.5937
3	12		0.7660	0.7666	0.7671	0.7676	0.7681	0.7685	0.7689	0.7692	0.7696	0.7699	0.7702	0.7705	0.7707
4	20		0.8938	0.8941	0.8944	0.8947	0.8949	0.8952	0.8955	0.8957	0.8959	0.8962	0.8964	0.8966	0.8968
5	30		0.9943	0.9942	0.9941	0.9941	0.9942	0.9943	0.9944	0.9945	0.9946	0.9947	0.9948	0.9949	0.9951
6	42		1.0777	1.0771	1.0767	1.0764	1.0761	1.0760	1.0759	1.0758	1.0758	1.0758	1.0758	1.0758	1.0758
7	56		1.1494	1.1483	1.1475	1.1469	1.1462	1.1458	1.1455	1.1452	1.1450	1.1448	1.1447	1.1446	1.1445
8	72		1.2128	1.2111	1.2098	1.2087	1.2078	1.2071	1.2065	1.2060	1.2056	1.2052	1.2050	1.2047	1.2045
9	90		1.2700	1.2677	1.2658	1.2642	1.2629	1.2619	1.2610	1.2602	1.2596	1.2591	1.2586	1.2582	1.2579
10	110		1.3224	1.3193	1.3168	1.3147	1.3130	1.3116	1.3104	1.3094	1.3085	1.3077	1.3071	1.3065	1.3060
11	132		1.3709	1.3671	1.3639	1.3613	1.3592	1.3573	1.3558	1.3544	1.3533	1.3523	1.3515	1.3507	1.3501
12	156		1.4164	1.4118	1.4079	1.4047	1.4020	1.3998	1.3978	1.3962	1.3948	1.3935	1.3924	1.3915	1.3907
13	182		1.4595	1.4539	1.4493	1.4455	1.4423	1.4396	1.4372	1.4352	1.4335	1.4320	1.4307	1.4295	1.4285
14	210		1.5004	1.4940	1.4886	1.4841	1.4803	1.4771	1.4743	1.4719	1.4699	1.4681	1.4665	1.4651	1.4639
15	240		1.5397	1.5322	1.5261	1.5209	1.5165	1.5127	1.5095	1.5067	1.5043	1.5022	1.5004	1.4987	1.4973
16	272		1.5775	1.5690	1.5620	1.5561	1.5510	1.5467	1.5431	1.5399	1.5371	1.5347	1.5326	1.5306	1.5290
17	306		1.6140	1.6045	1.5986	1.5899	1.5842	1.5794	1.5752	1.5716	1.5684	1.5656	1.5632	1.5610	1.5591
18	342		1.6495	1.6389	1.6301	1.6225	1.6162	1.6108	1.6061	1.6020	1.5984	1.5953	1.5926	1.5901	1.5880
19	380		1.6841	1.6724	1.6626	1.6543	1.6472	1.6412	1.6359	1.6314	1.6274	1.6239	1.6208	1.6181	1.6157
20	420		1.7178	1.7050	1.6942	1.6851	1.6773	1.6706	1.6648	1.6598	1.6554	1.6515	1.6481	1.6450	1.6423
21	462		1.7509	1.7369	1.7251	1.7152	1.7066	1.6993	1.6929	1.6874	1.6825	1.6782	1.6745	1.6711	1.6681

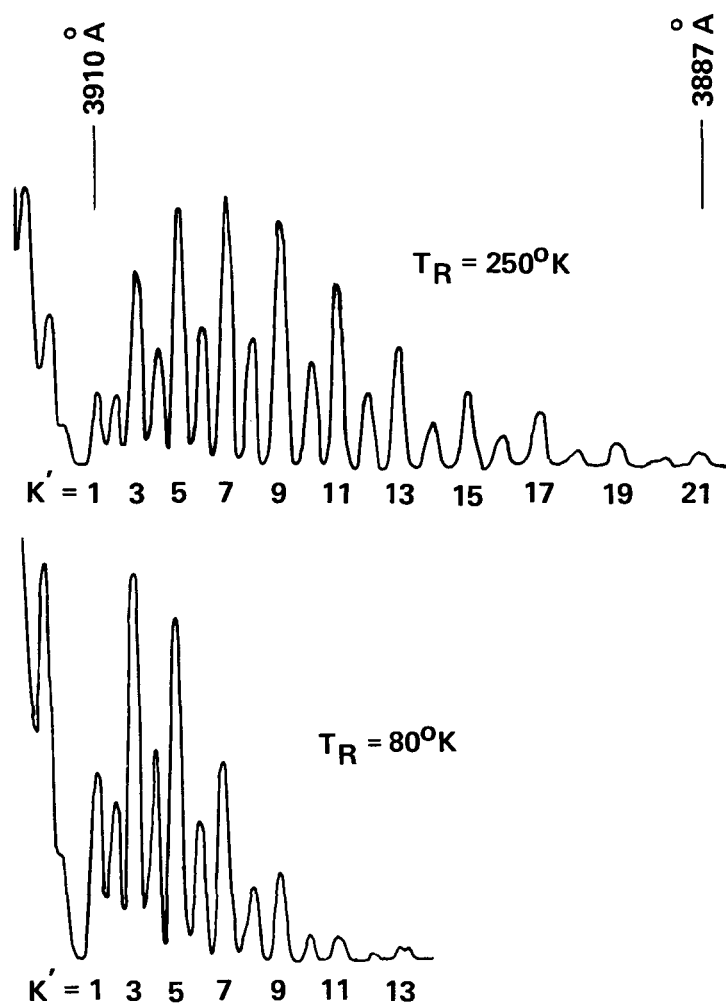
Table I (cont'd)

TABLE VALUES = LOG(10) OF  $2 \cdot K \cdot G \cdot (\text{LAMBDA} / \text{LAMBDA}_0)^{0.4}$  FOR THE 3-BRANCH OF THE (0,0)-BAND OF THE FIRST NEGATIVE SYSTEM OF  $\text{N}_2^+$   
 $K$  = QUANTUM NUMBER     $\text{LAMBDA}_0 = 3909.71$  ÅNGSTRÖMS  
 $G = ((K+1) \cdot \exp(-2 \cdot (K+1) \cdot \text{THEIR}/\text{TR})) + K \cdot \exp(2 \cdot K \cdot \text{THEIR}/\text{TR})) / (2 \cdot (K+1))$   
 $\text{THEIR} = 2.87$  (ROTATIONAL CONSTANT FOR THE GROUND STATE)     $\text{TR} = \text{ROTATIONAL TEMPERATURE (DEG K)}$

$K$	$K \cdot (K+1)$	TR=	280	290	300	350	400	450	500	550	600	650	700	750	800
1	2		0.2923	0.2926	0.2929	0.2940	0.2949	0.2956	0.2961	0.2965	0.2969	0.2972	0.2975	0.2977	0.2979
2	6		0.5940	0.5943	0.5945	0.5955	0.5964	0.5970	0.5975	0.5980	0.5983	0.5986	0.5989	0.5991	0.5993
3	12		0.7710	0.7712	0.7714	0.7724	0.7731	0.7737	0.7741	0.7745	0.7749	0.7751	0.7754	0.7756	0.7758
4	20		0.8970	0.8972	0.8973	0.8981	0.8987	0.8992	0.8995	0.9000	0.9003	0.9006	0.9008	0.9010	0.9012
5	30		0.9952	0.9953	0.9954	0.9960	0.9964	0.9969	0.9972	0.9975	0.9978	0.9980	0.9982	0.9984	0.9986
6	42		1.0758	1.0759	1.0759	1.0762	1.0766	1.0768	1.0771	1.0774	1.0776	1.0778	1.0780	1.0781	1.0783
7	56		1.1445	1.1444	1.1444	1.1444	1.1445	1.1447	1.1449	1.1450	1.1452	1.1454	1.1455	1.1456	1.1458
8	72		1.2043	1.2042	1.2041	1.2038	1.2037	1.2037	1.2037	1.2038	1.2039	1.2041	1.2042	1.2043	1.2044
9	90		1.2576	1.2573	1.2571	1.2564	1.2561	1.2559	1.2559	1.2559	1.2559	1.2560	1.2560	1.2561	1.2562
10	110		1.3056	1.3053	1.3049	1.3038	1.3032	1.3028	1.3027	1.3026	1.3025	1.3025	1.3025	1.3026	1.3026
11	132		1.3495	1.3490	1.3485	1.3470	1.3460	1.3455	1.3452	1.3450	1.3448	1.3448	1.3447	1.3447	1.3447
12	156		1.3899	1.3893	1.3887	1.3866	1.3854	1.3846	1.3841	1.3838	1.3836	1.3835	1.3834	1.3833	1.3833
13	182		1.4276	1.4268	1.4261	1.4234	1.4219	1.4208	1.4202	1.4197	1.4194	1.4192	1.4191	1.4190	1.4189
14	210		1.4628	1.4618	1.4610	1.4578	1.4558	1.4546	1.4537	1.4531	1.4527	1.4524	1.4522	1.4520	1.4519
15	240		1.4960	1.4949	1.4938	1.4900	1.4877	1.4861	1.4851	1.4844	1.4838	1.4835	1.4832	1.4830	1.4828
16	272		1.5275	1.5261	1.5249	1.5205	1.5177	1.5159	1.5145	1.5137	1.5131	1.5126	1.5122	1.5120	1.5118
17	306		1.5574	1.5559	1.5545	1.5494	1.5462	1.5440	1.5425	1.5415	1.5407	1.5401	1.5397	1.5393	1.5391
18	342		1.5860	1.5843	1.5827	1.5769	1.5732	1.5707	1.5690	1.5678	1.5669	1.5662	1.5657	1.5653	1.5649
19	380		1.6135	1.6115	1.6098	1.6032	1.5990	1.5962	1.5942	1.5928	1.5917	1.5910	1.5903	1.5899	1.5895
20	420		1.6399	1.6377	1.6358	1.6284	1.6237	1.6205	1.6183	1.6167	1.6155	1.6146	1.6139	1.6135	1.6129
21	462		1.6654	1.6630	1.6608	1.6526	1.6474	1.6438	1.6413	1.6395	1.6382	1.6371	1.6364	1.6357	1.6352

Table 2  
NOZZLE GEOMETRY AND OPERATING CONDITIONS FOR DISCHARGE COEFFICIENTS IN FIG. 38

AUTHOR	$2r_*(\text{mm})$	$\theta_1$	$r_L/r_*$	$\theta_2$	$A_E/A_*$	$p_o/p_\infty$	B
MILLIGAN (1964) EXPERIMENT	3.25	-25°	0	9°	4.4	2 TO 20	$10^{-1}$ TO $10^3$
RAE (1969) THEORY	—	-20° TO -30°	0.5	15° TO 25°	—	—	$10^2$ TO $10^3$
MASSIER ET AL. (1970) EXPERIMENT	15.2	-10°	4	10°	2.8	> 2	$10^3$ TO $10^6$
PRESENT EXPERIMENT	5.1 2.5	-30°	0.5	20°	66	> 240 > 900	$10^2$ TO $10^3$



**Figure 1 ROTATIONAL FINE-STRUCTURE IN THE R-BRANCH OF THE O-O BAND OF THE  $N_2^+(1-)$  SYSTEM AT TWO DIFFERENT TEMPERATURES.**

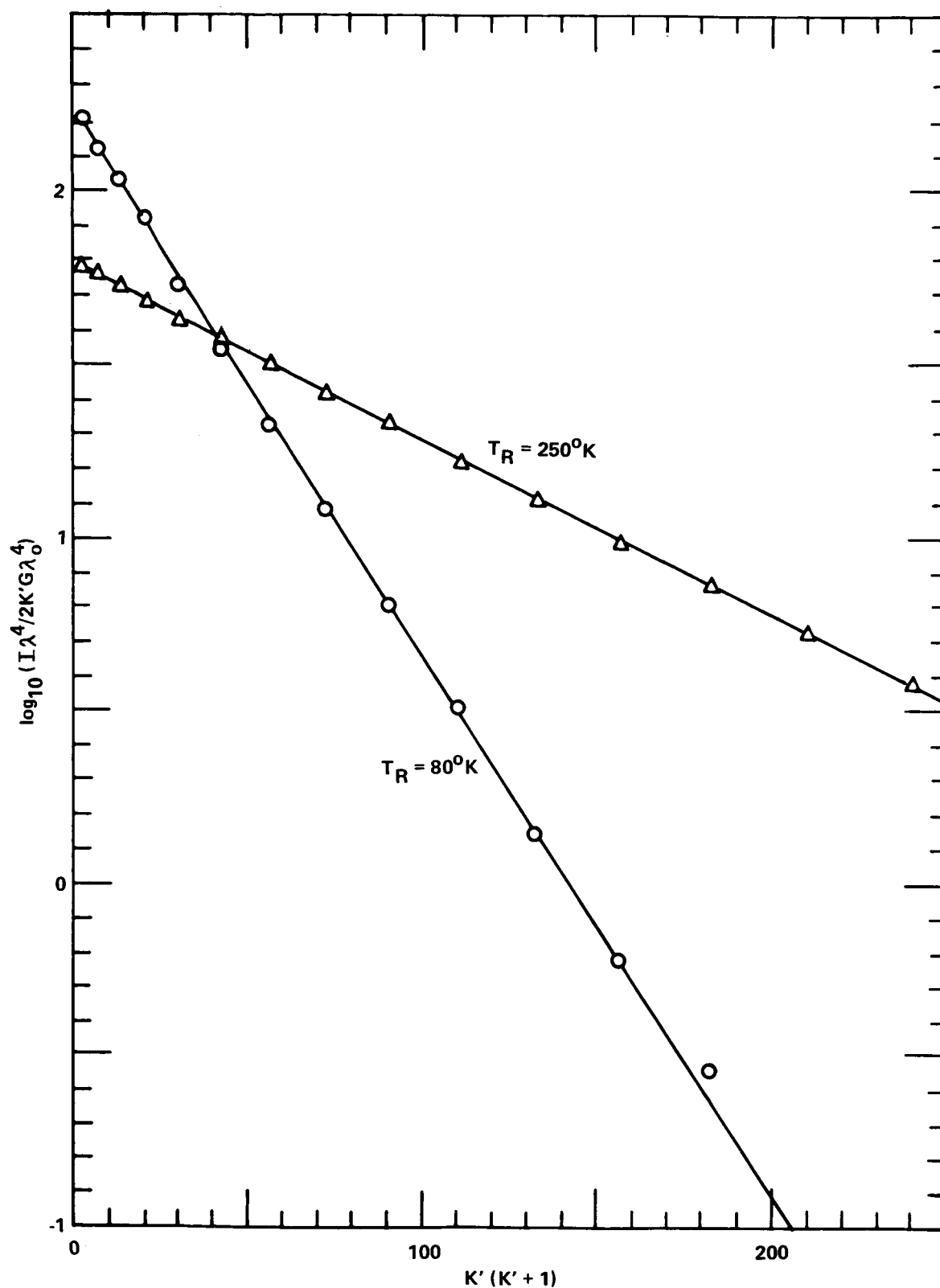


Figure 2 SEMI-LOGARITHMIC PLOT OF NORMALIZED LINE INTENSITIES VERSUS  $K'(K'+1)$ , ILLUSTRATING METHOD OF DATA REDUCTION FOR BANDS SHOWN IN FIG. 1

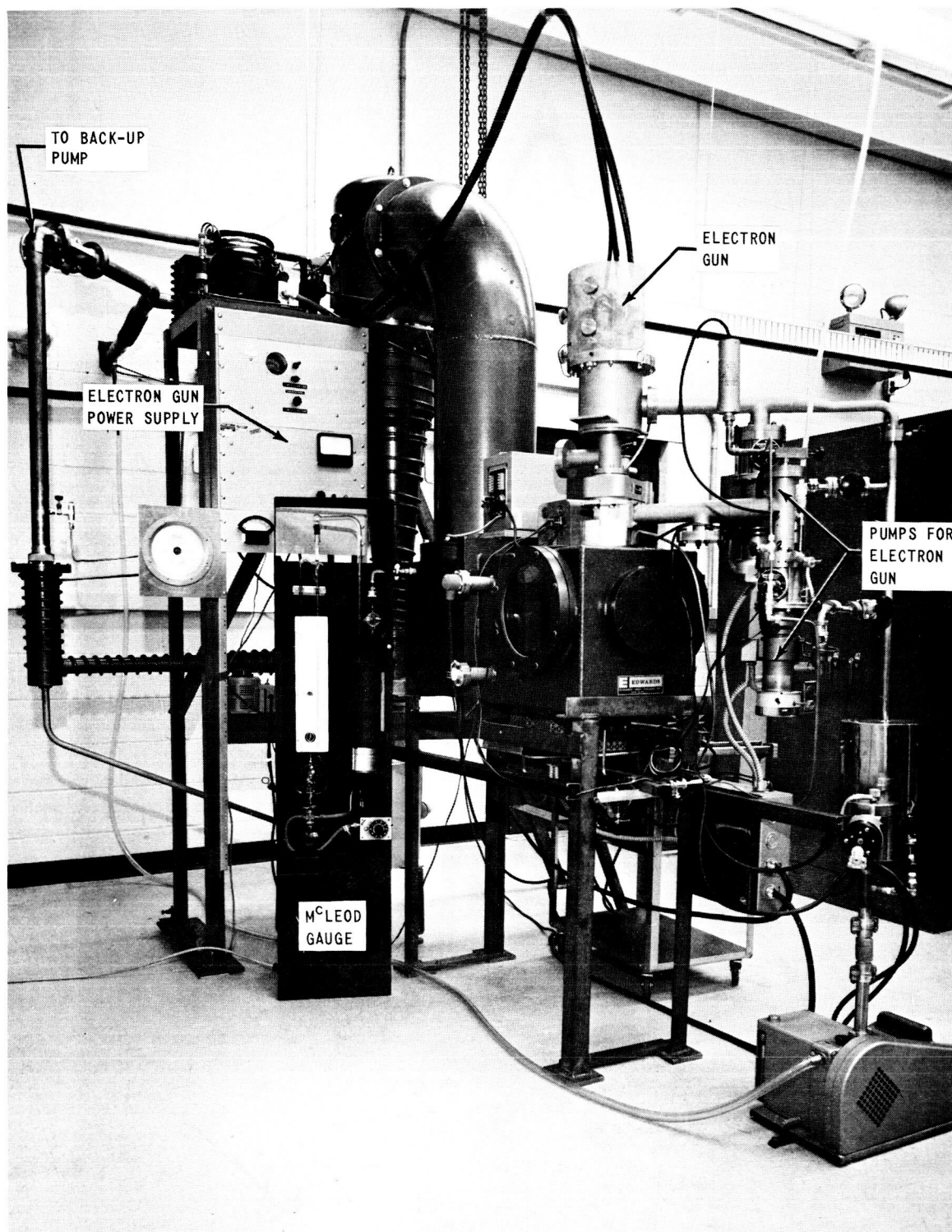


Figure 3 LOW-DENSITY FLOW FACILITY WITH ELECTRON GUN

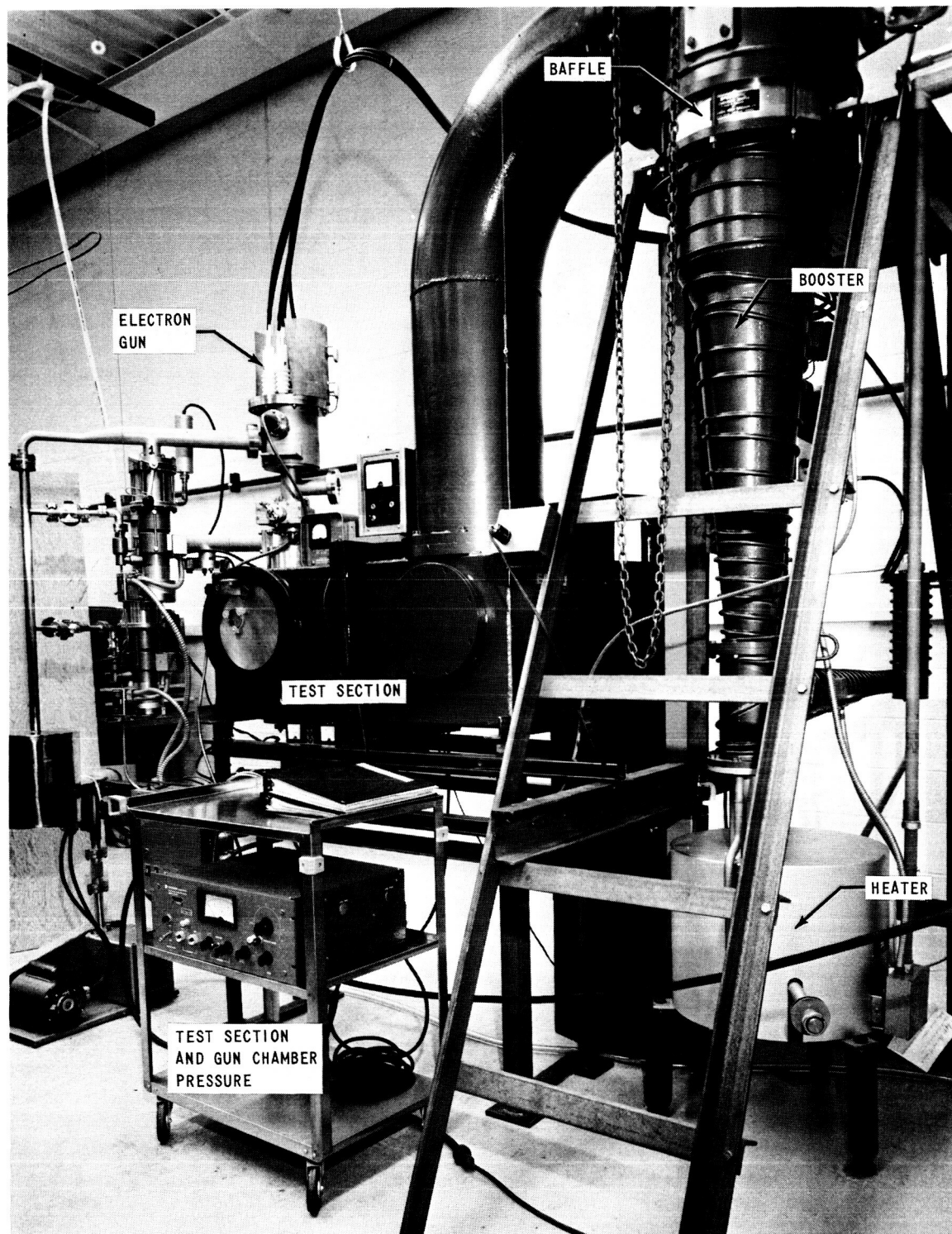


Figure 4 LOW-DENSITY FLOW FACILITY



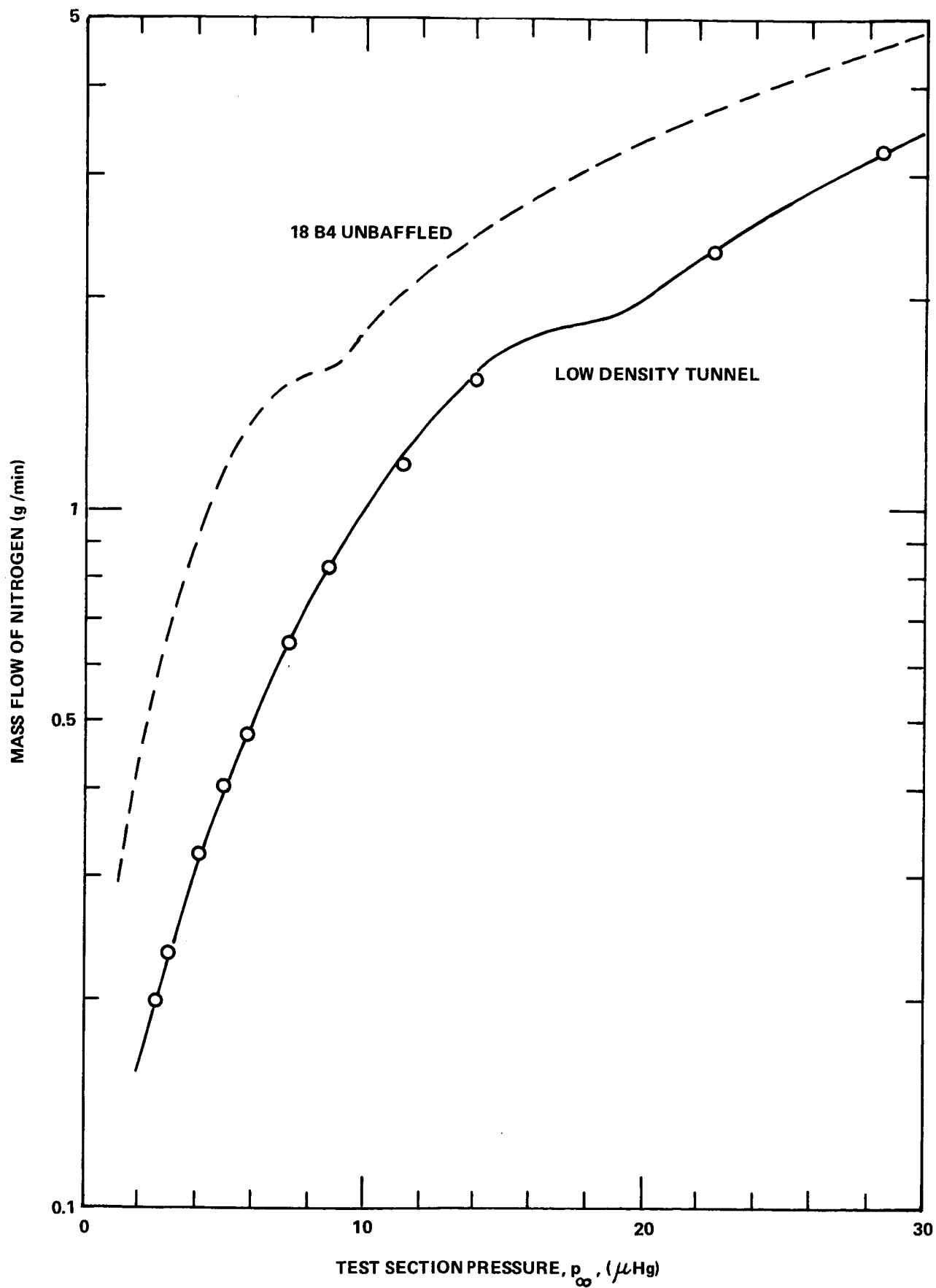


Figure 5 MASS FLOW CAPABILITY OF LOW-DENSITY TUNNEL FOR NITROGEN

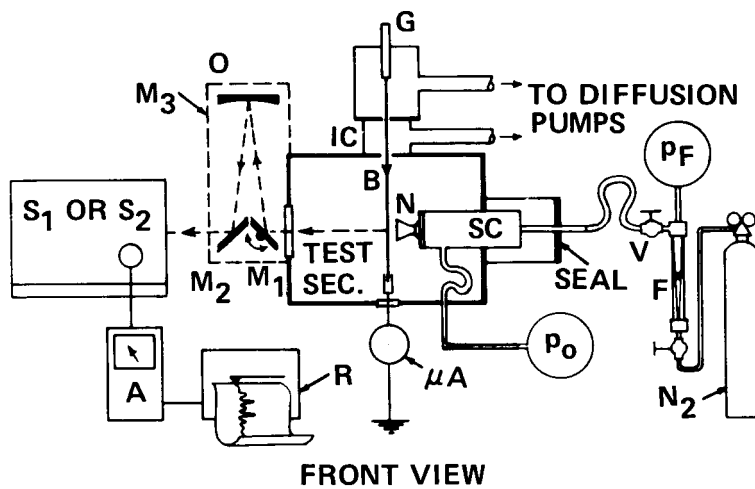
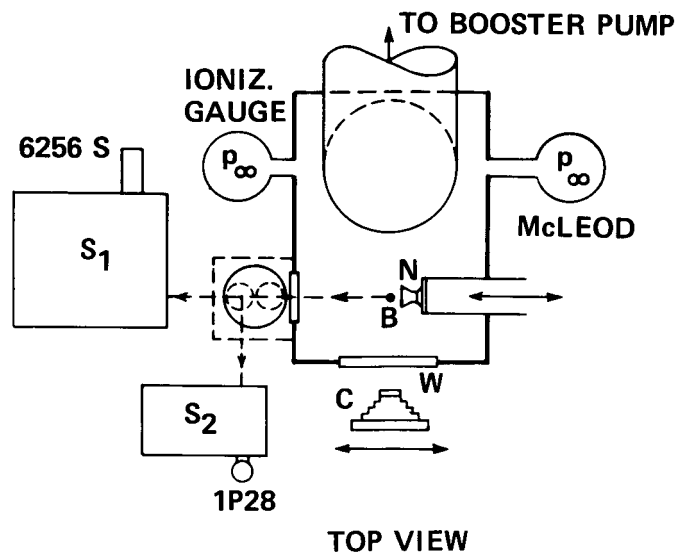


Figure 6 OUTLINE OF EXPERIMENTAL ARRANGEMENT

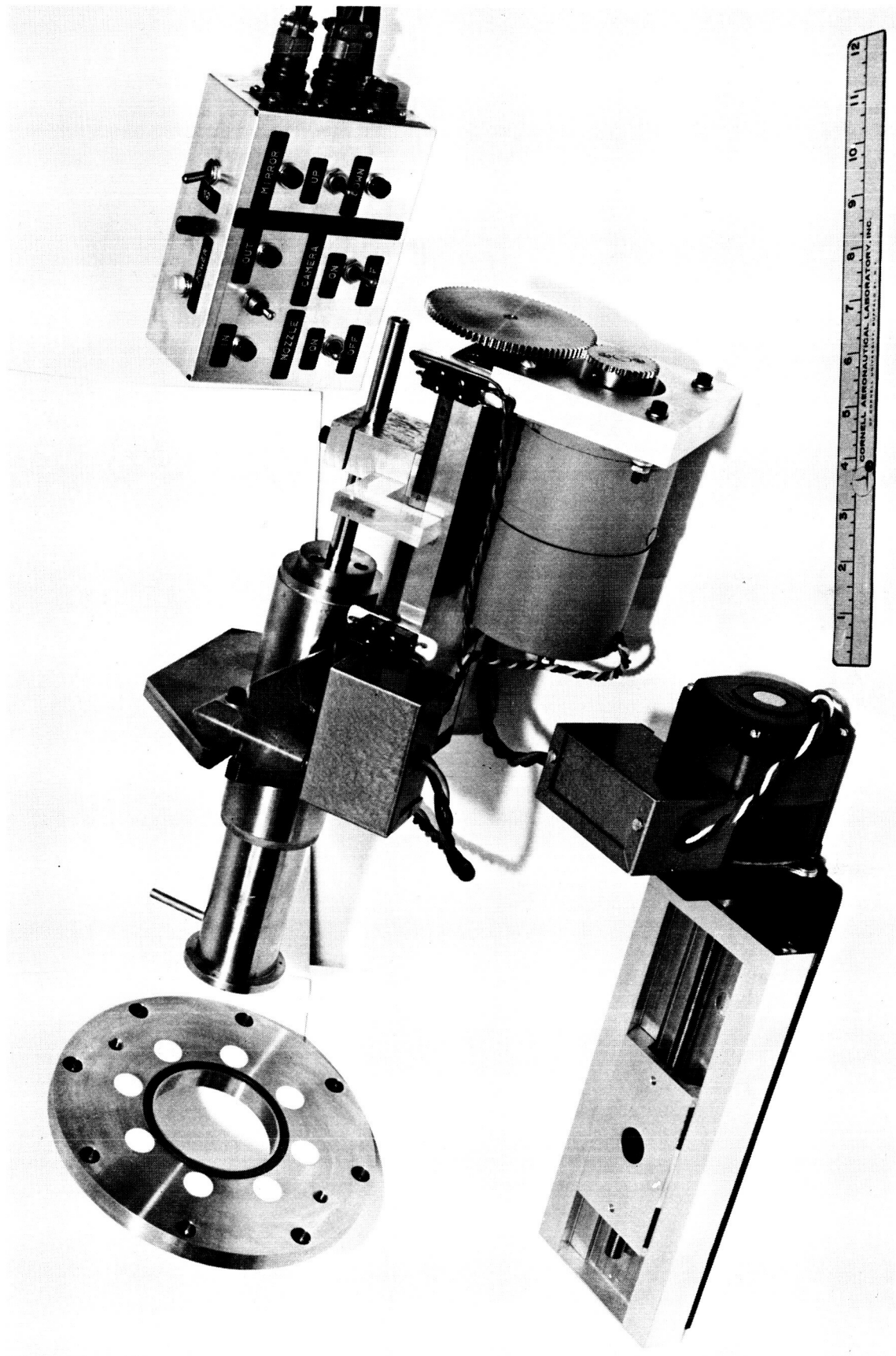


Figure 7 STAGNATION CHAMBER WITH MOUNTING FLANGE AND DRIVE MECHANISM (CENTER), AND  
MOTORIZED CAMERA PLATFORM (LEFT)

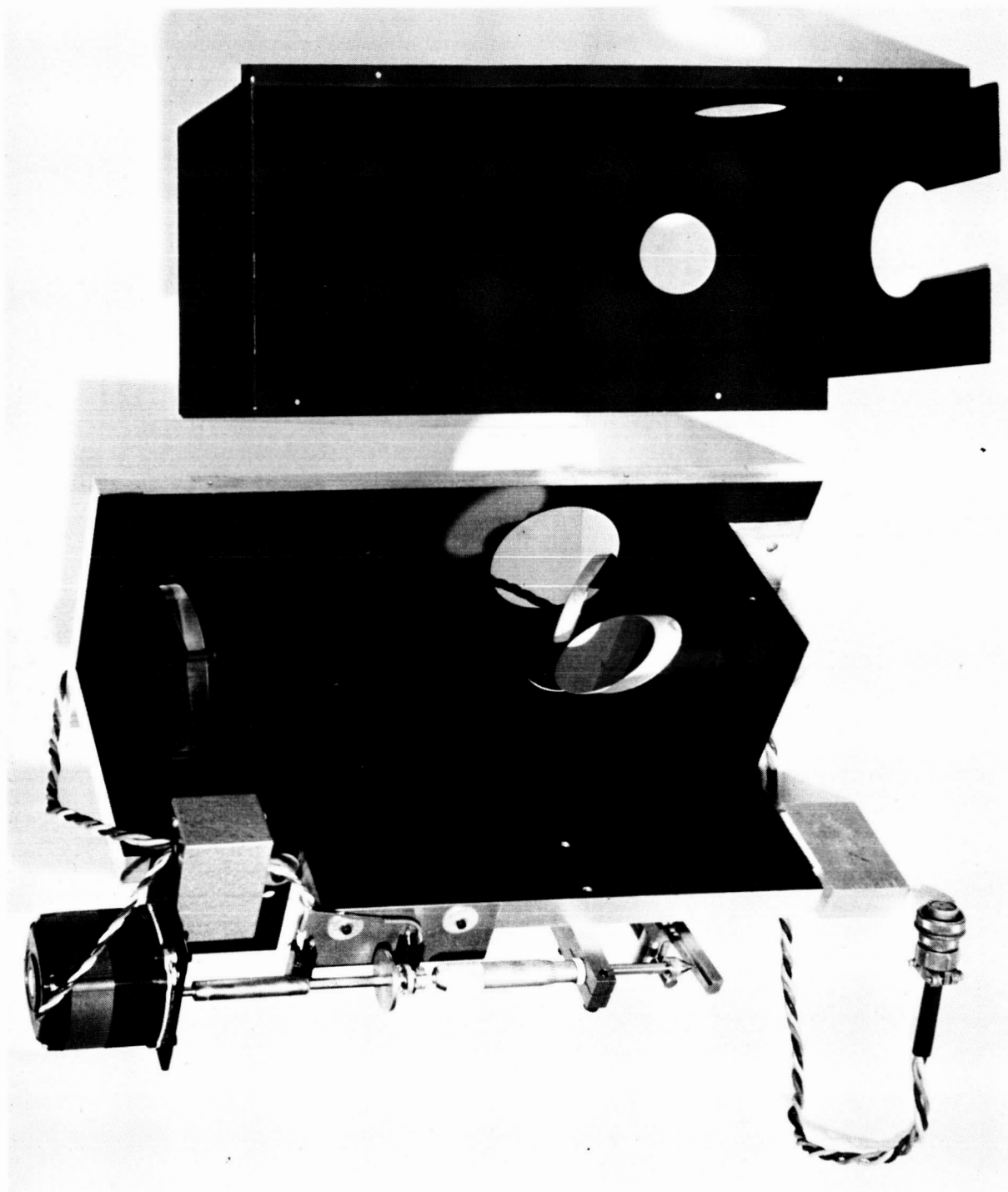


Figure 8 OPTICAL IMAGING AND SCANNING SYSTEM (INSIDE VIEW)

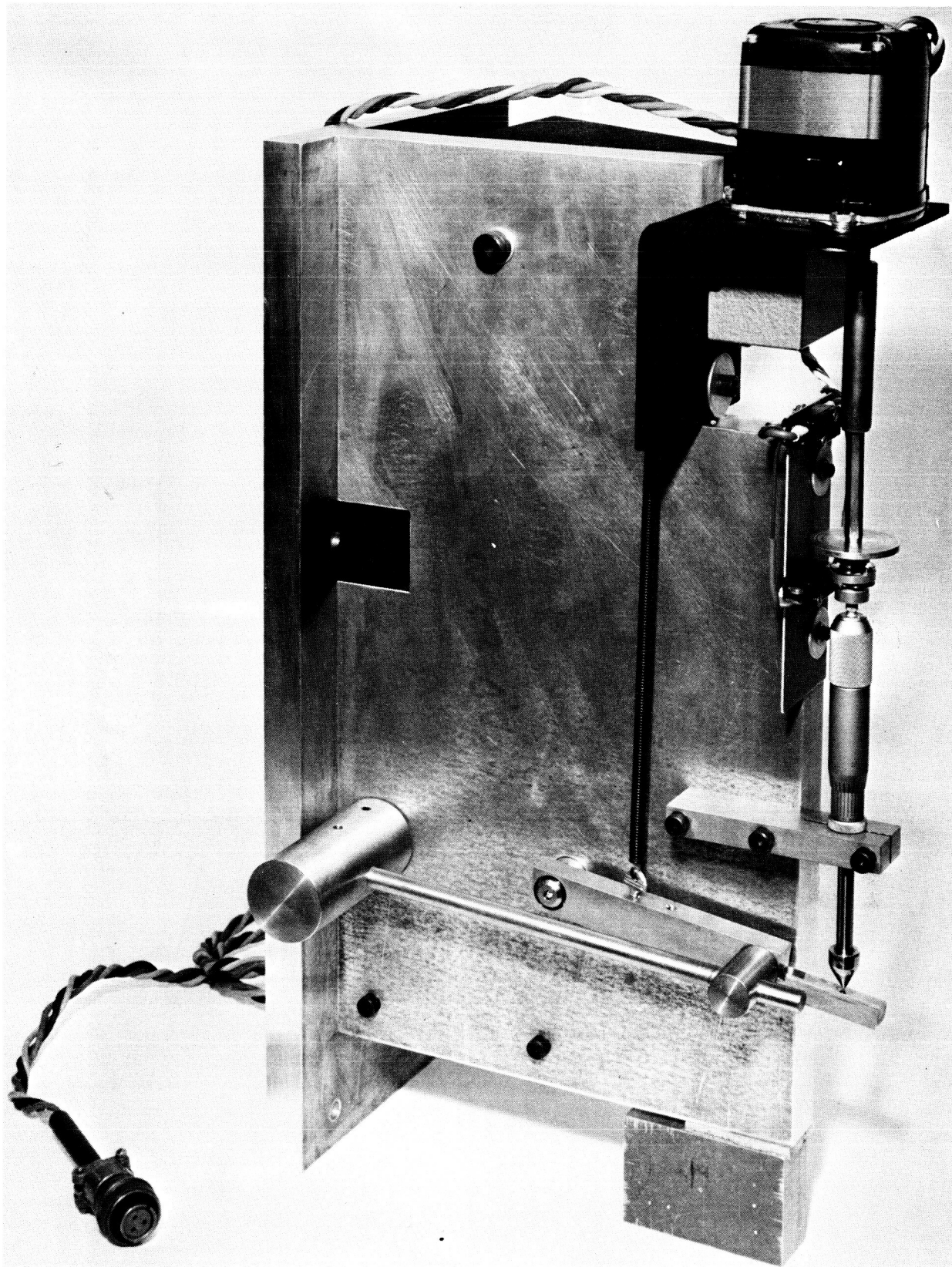
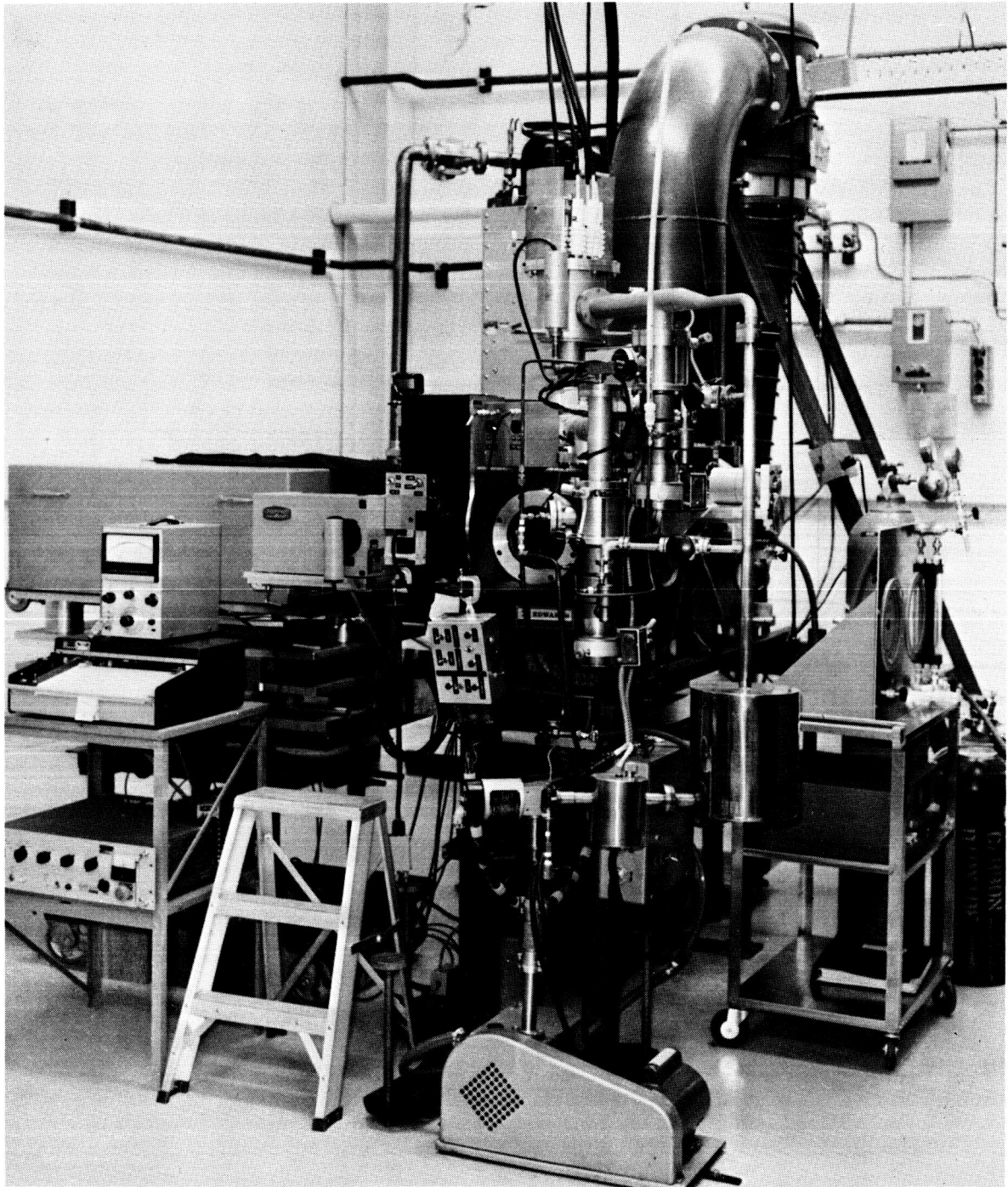
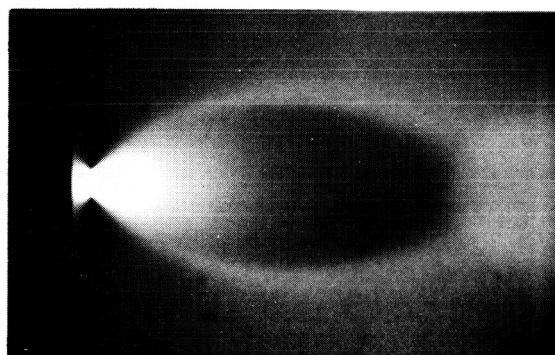


Figure 9 OPTICAL IMAGING AND SCANNING SYSTEMS (REAR VIEW SHOWING LINKAGE AND DRIVE MECHANISM FOR ROTATING MIRROR)

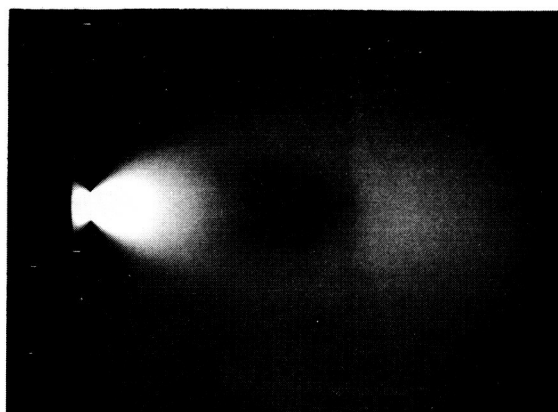




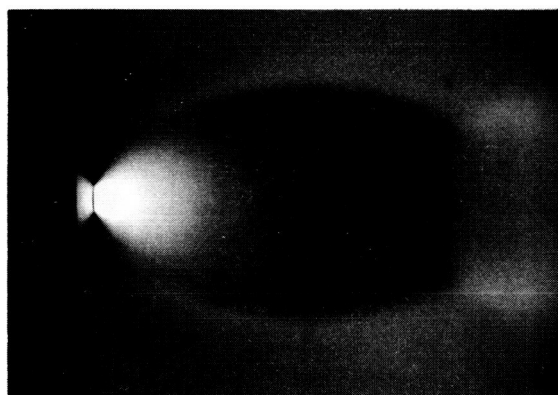
**Figure 10**    **LOW-DENSITY TUNNEL WITH ELECTRON GUN AND OPTICAL INSTRUMENTATION**



Ar  
 $p_{\infty} = 31 \mu \text{ Hg}$

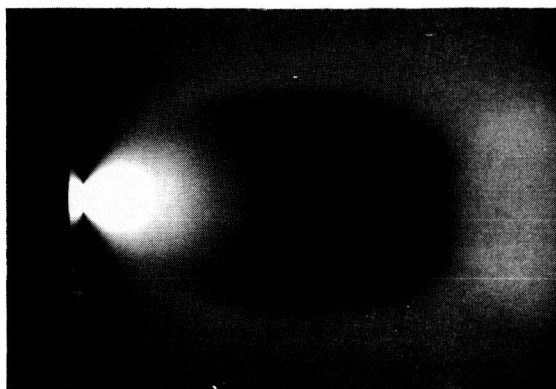


He  
 $p_{\infty} = 50 \mu \text{ Hg}$



CO<sub>2</sub>  
 $p_{\infty} = 27 \mu \text{ Hg}$

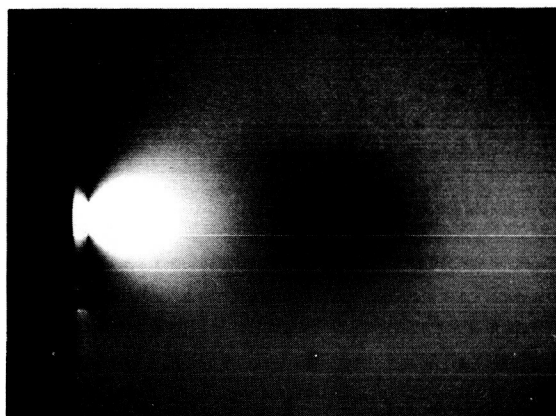
Figure 11 FREE JET PLUMES OF ARGON, HELIUM AND CARBON-DIOXIDE  
 $(p_0 = 9.8 \text{ Torr})$



A

$$p_0 = 9800 \mu \text{ Hg}$$

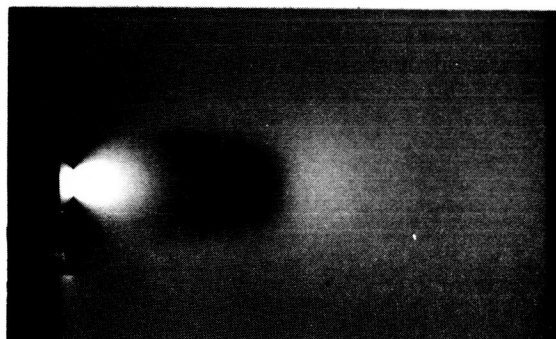
$$p_\infty = 29 \mu \text{ Hg}$$



B

$$p_0 = 4200 \mu \text{ Hg}$$

$$p_\infty = 13 \mu \text{ Hg}$$



C

$$p_0 = 4200 \mu \text{ Hg}$$

$$p_\infty = 42 \mu \text{ Hg}$$

Figure 12 NITROGEN FREE JETS



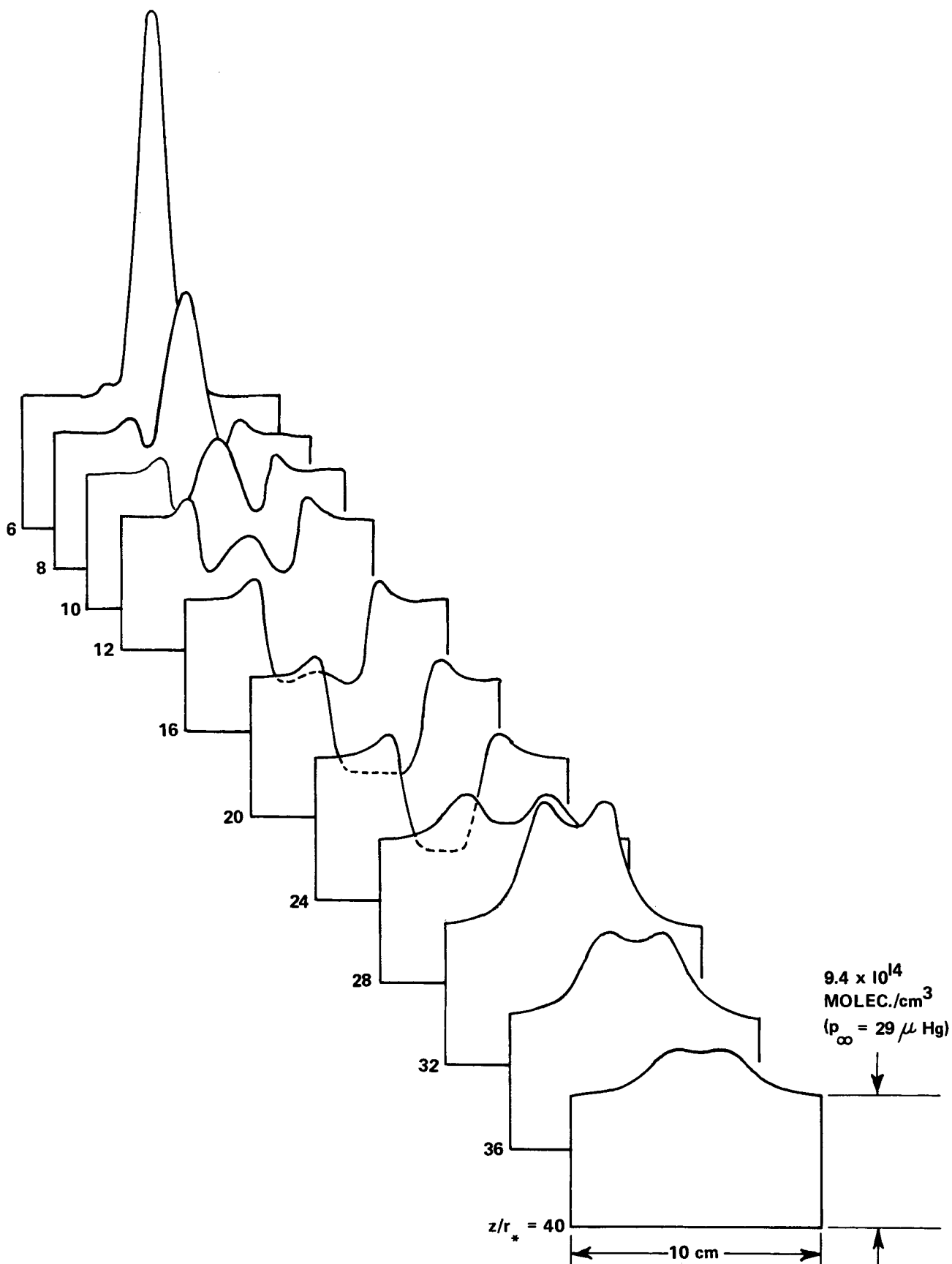
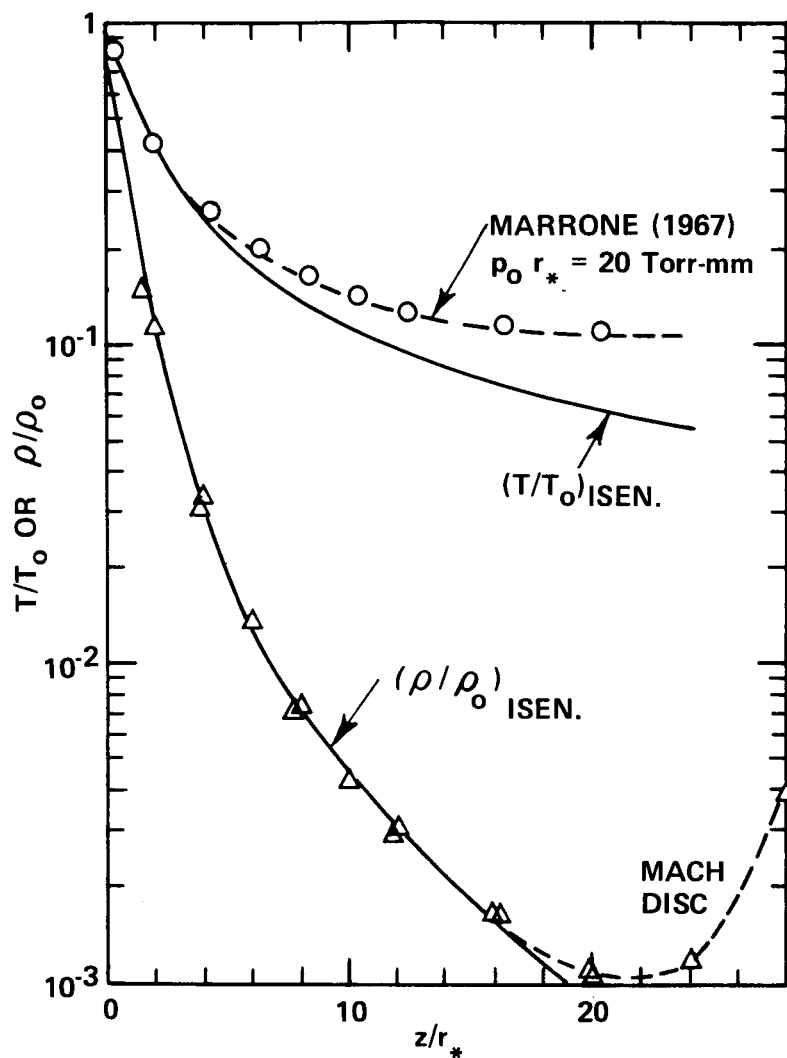


Figure 13 RADIAL DENSITY PROFILES AT VARIOUS AXIAL POSITIONS IN THE FREE-JET PLUME OF FIGURE 12A ( $r_* = 2.5 \text{ mm}$ )



**Figure 14 ELECTRON-BEAM MEASUREMENTS  
OF TEMPERATURE AND DENSITY  
ALONG THE CENTERLINE OF A  
FREE-JET ( $p_0 r_* = 23$  Torr-mm)**

$$T_0 = 300^\circ\text{K}$$

$$p_0 = 9.2 \text{ Torr}$$

$$r_* = 2.5 \text{ mm}$$

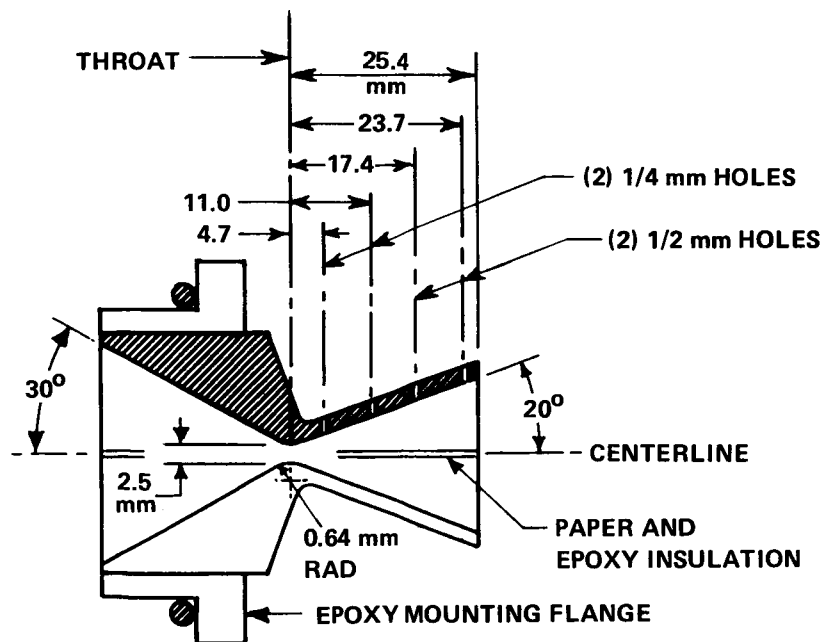
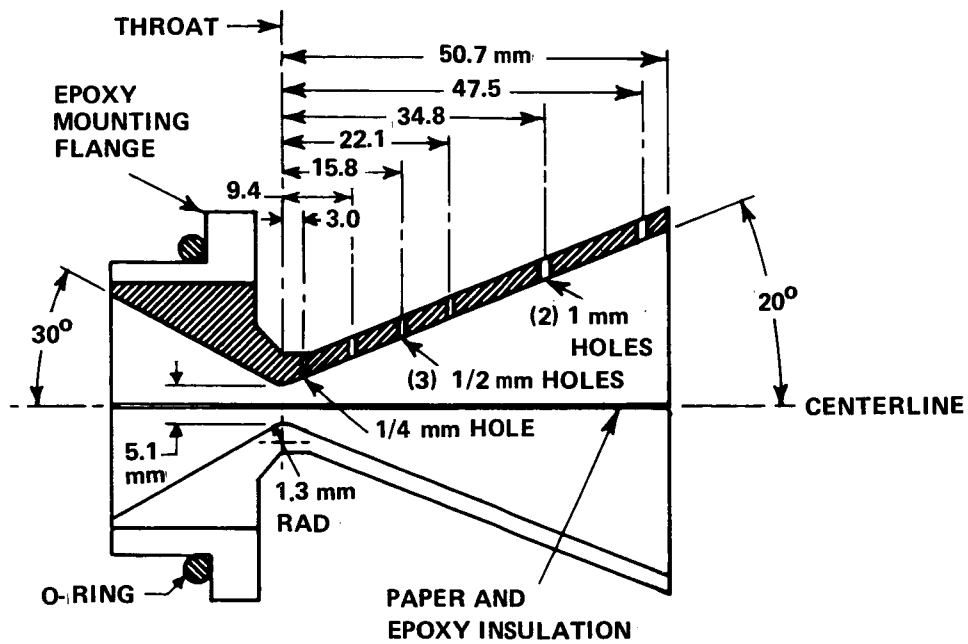


Figure 15 GRAPHITE NOZZLES WITH THROAT DIAMETERS OF 5 mm AND 2.5 mm

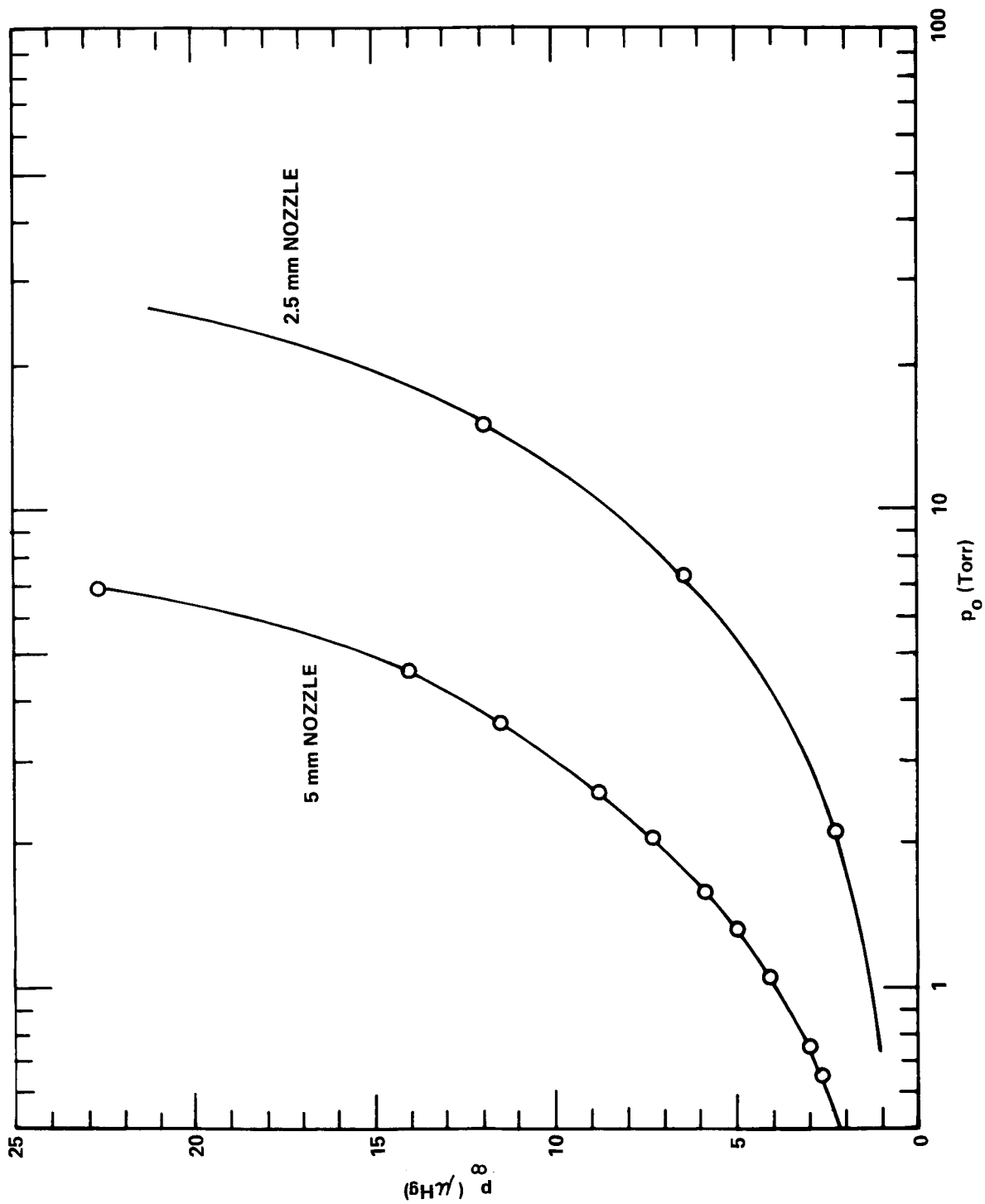
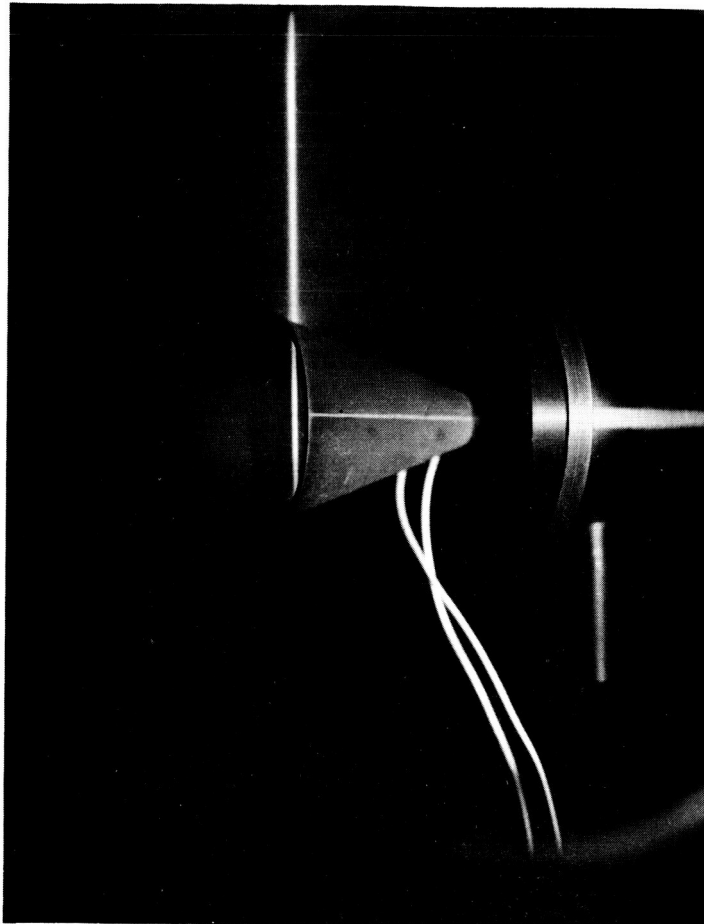
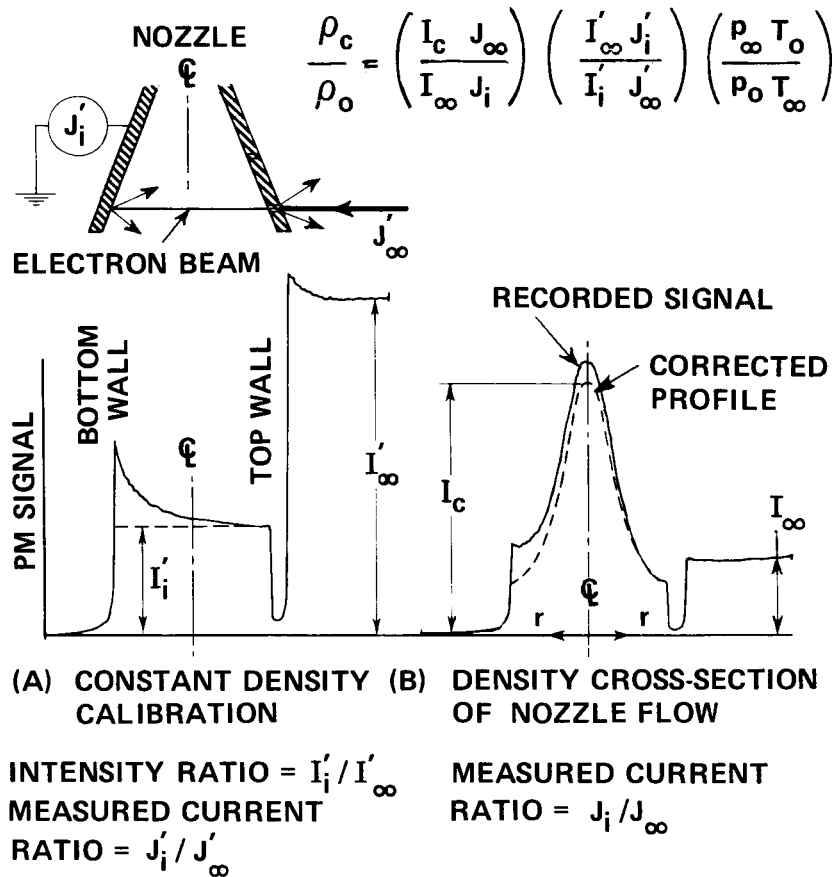


Figure 16 MINIMUM TEST SECTION PRESSURES,  $p_0$ , FOR THE TWO NOZZLES



**Figure 17 PHOTOGRAPH OF ELECTRON BEAM  
INSIDE NOZZLE**



**Figure 18 DETERMINATION OF RADIAL DENSITY PROFILES INSIDE NOZZLE (ACTUAL RECORD FOR  $B = 590$ ,  $z/r_* = 18.7$ )**

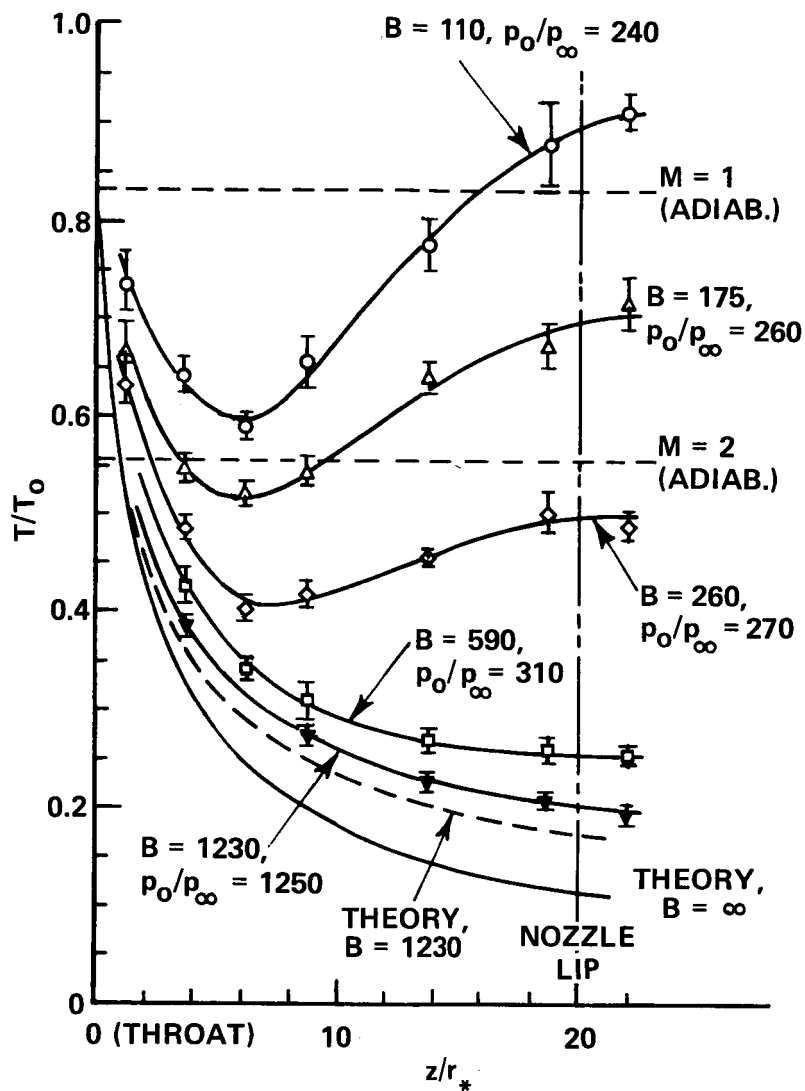


**Figure 19 MEASURED GAS TEMPERATURES  
ALONG NOZZLE AXIS FOR MAX-  
IMUM NOZZLE PRESSURE  
RATIOS ( $p_0/p_\infty$ )**  
OPEN SYMBOLS: 5 mm NOZZLE  
FILLED SYMBOLS: 2.5 mm NOZZLE

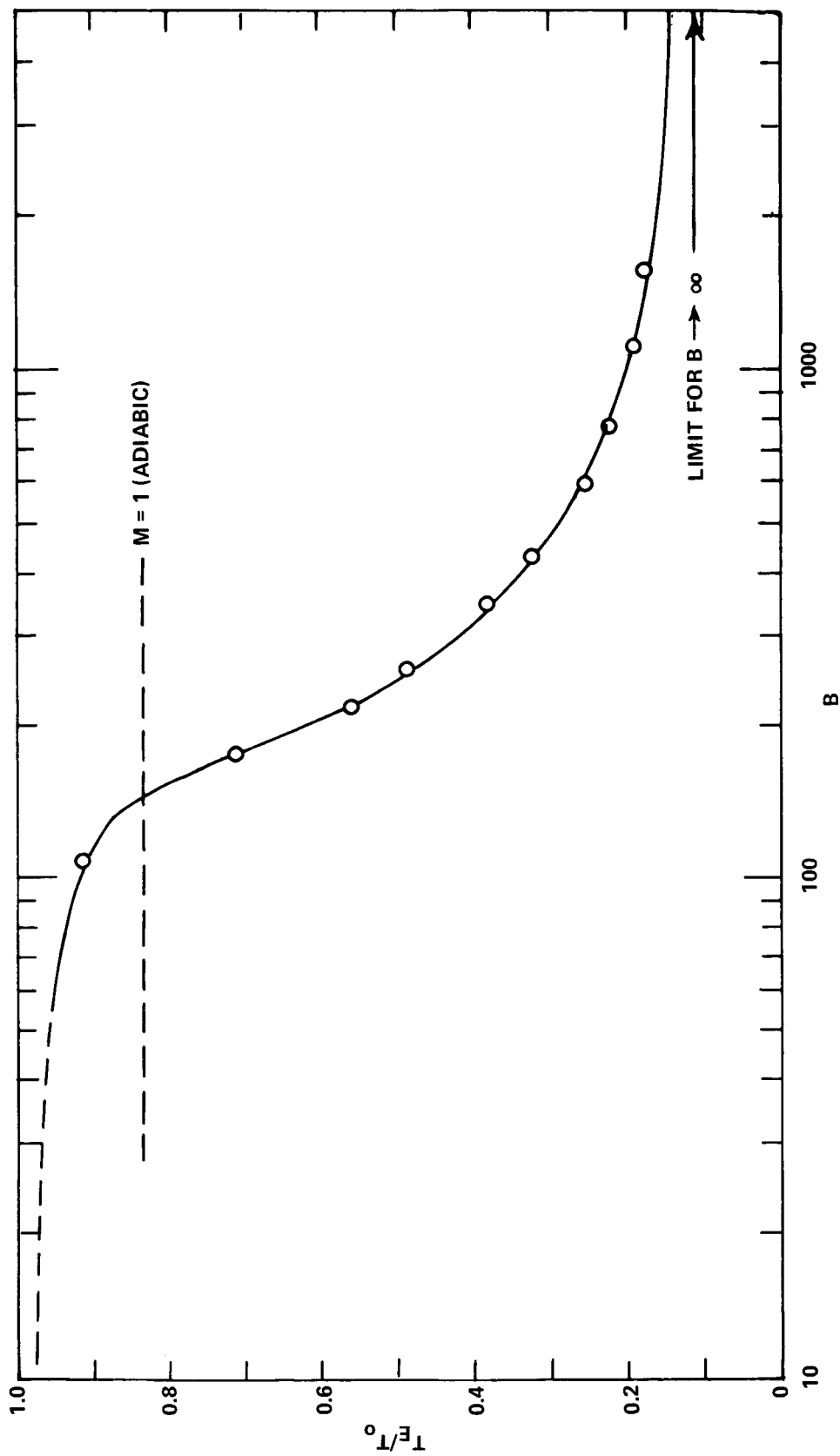
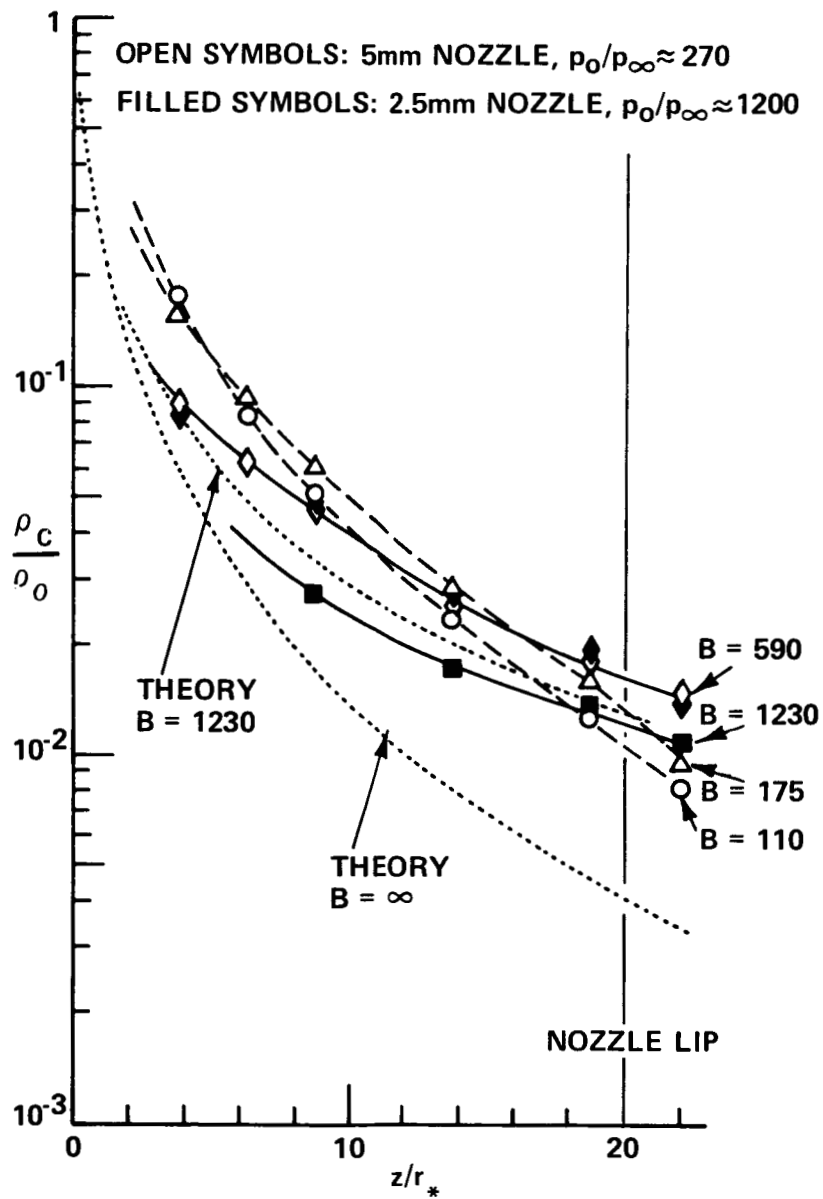


Figure 20 CENTERLINE TEMPERATURE JUST DOWNSTREAM OF NOZZLE EXIT AS A FUNCTION OF REYNOLDS NUMBER ( $p_o/p_\infty \approx 300$ )





**Figure 21 CENTERLINE DENSITIES AT MAXIMUM NOZZLE PRESSURE RATIOS**

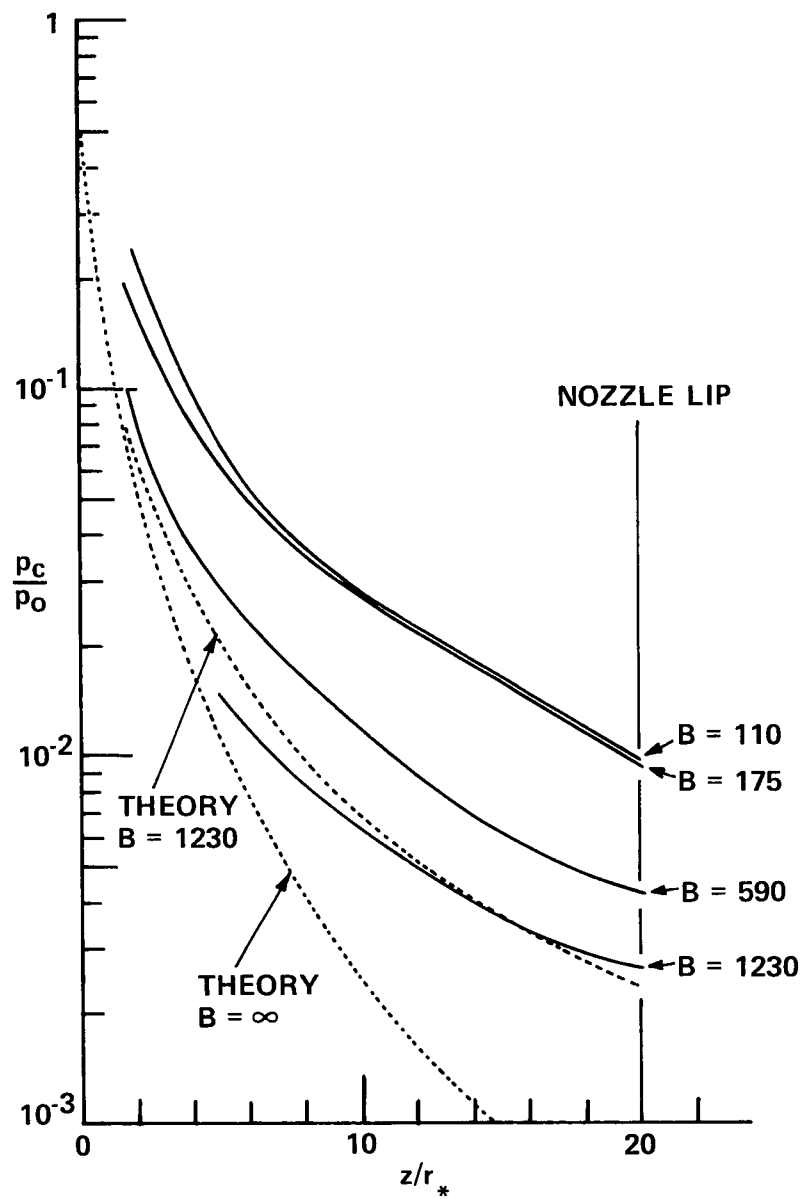


Figure 22 CENTERLINE PRESSURES DERIVED FROM MEASURED DENSITIES AND TEMPERATURES (FIGS. 19 AND 21)

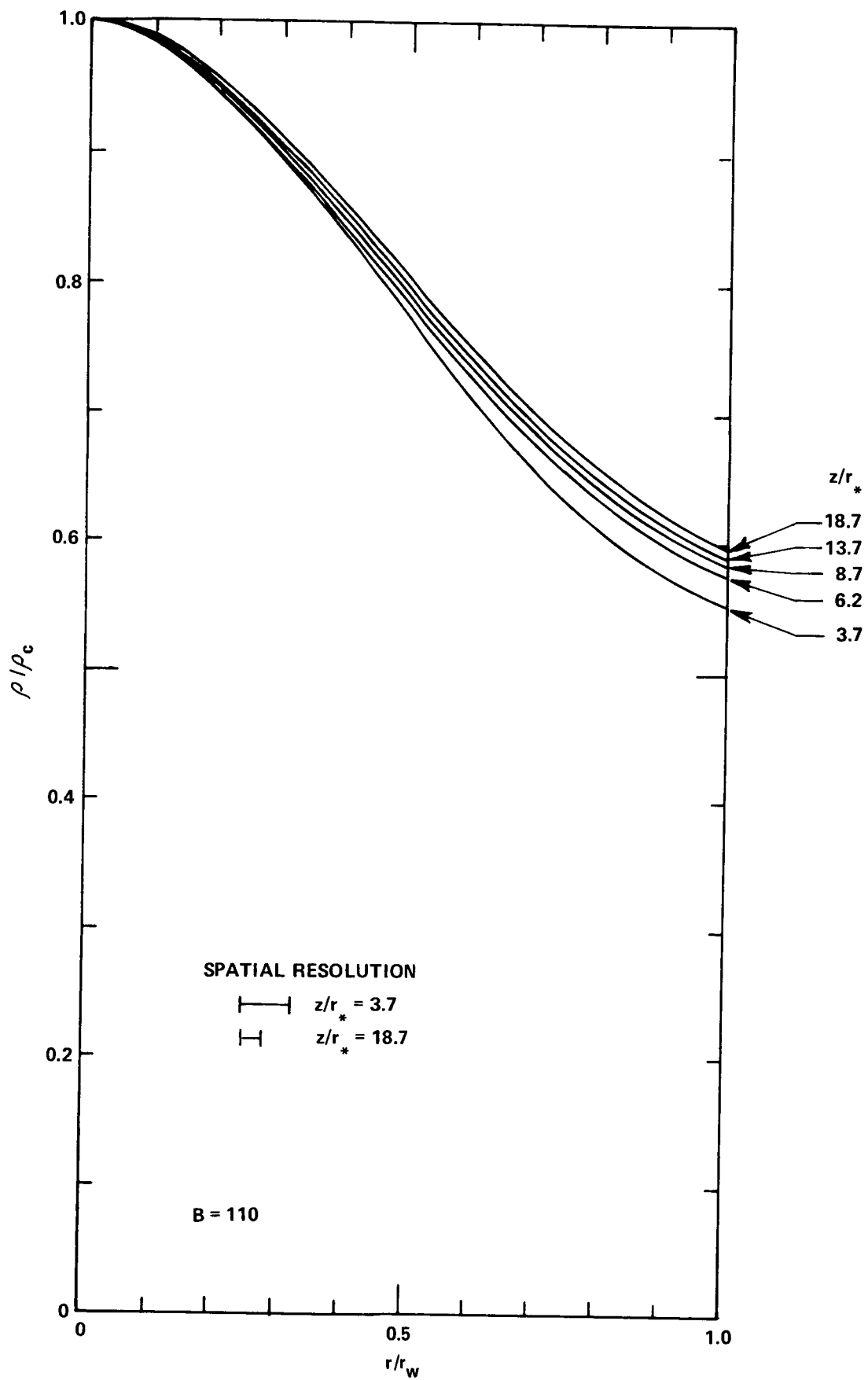


Figure 23 MEASURED RADIAL DENSITY PROFILES IN THE 5 mm NOZZLE AT  $B = 110$

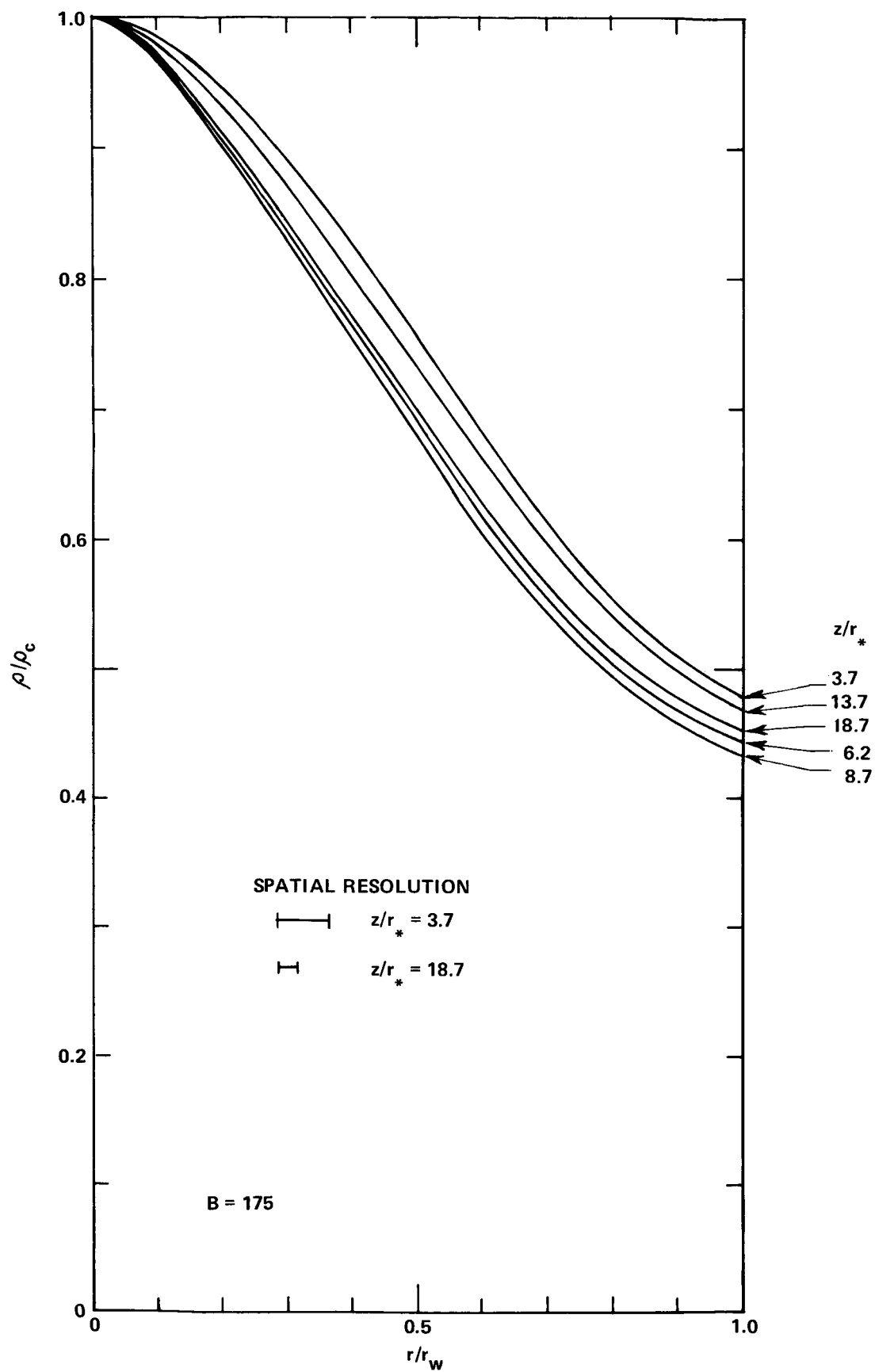


Figure 24 MEASURED RADIAL DENSITY PROFILES IN THE 5 mm NOZZLE AT  $B = 175$

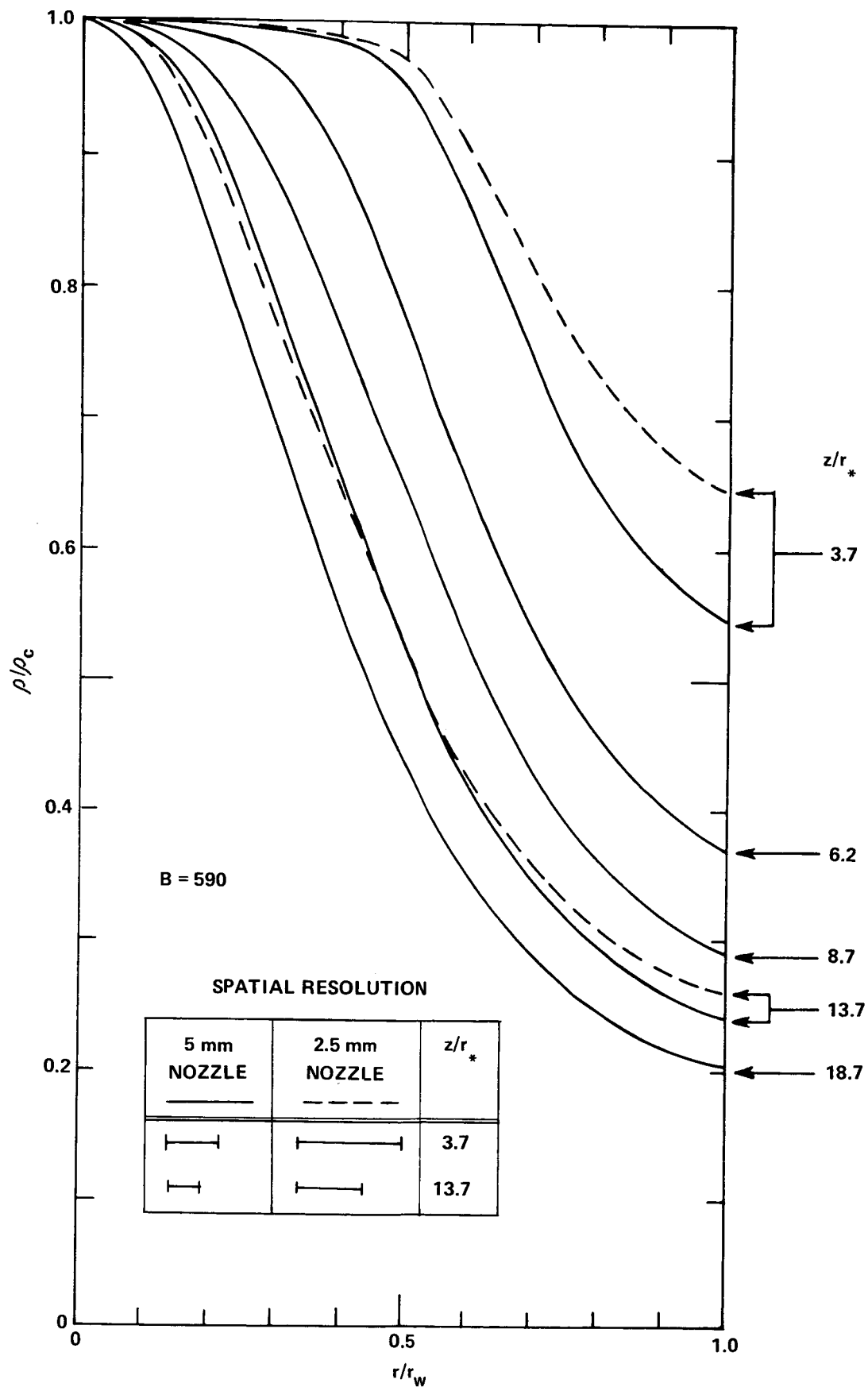


Figure 25 MEASURED RADIAL DENSITY PROFILES IN THE 5 mm AND 2.5 mm NOZZLES AT  $B = 590$

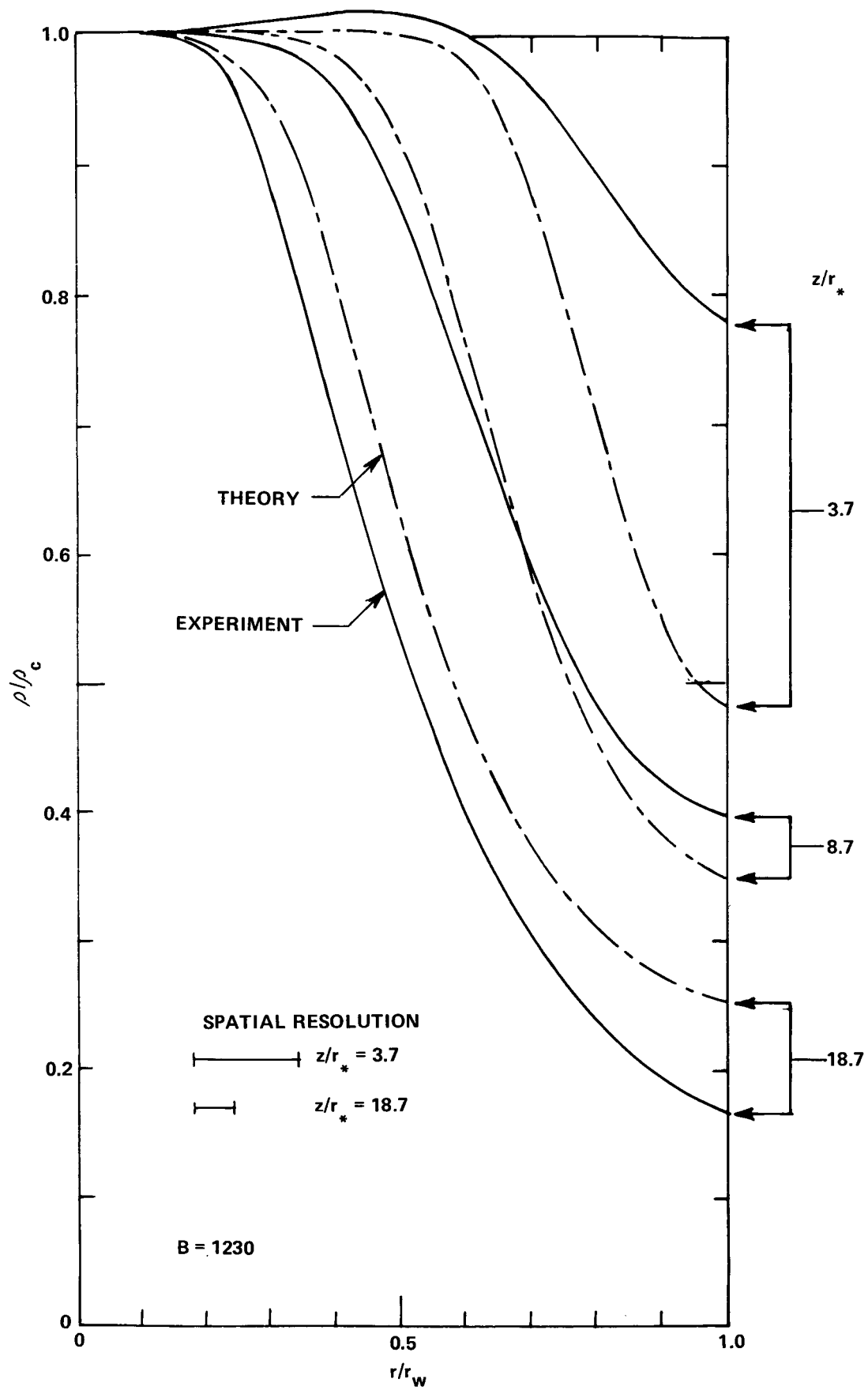


Figure 26 MEASURED AND CALCULATED RADIAL DENSITY PROFILES IN THE 2.5 mm NOZZLE AT  $B = 1230$

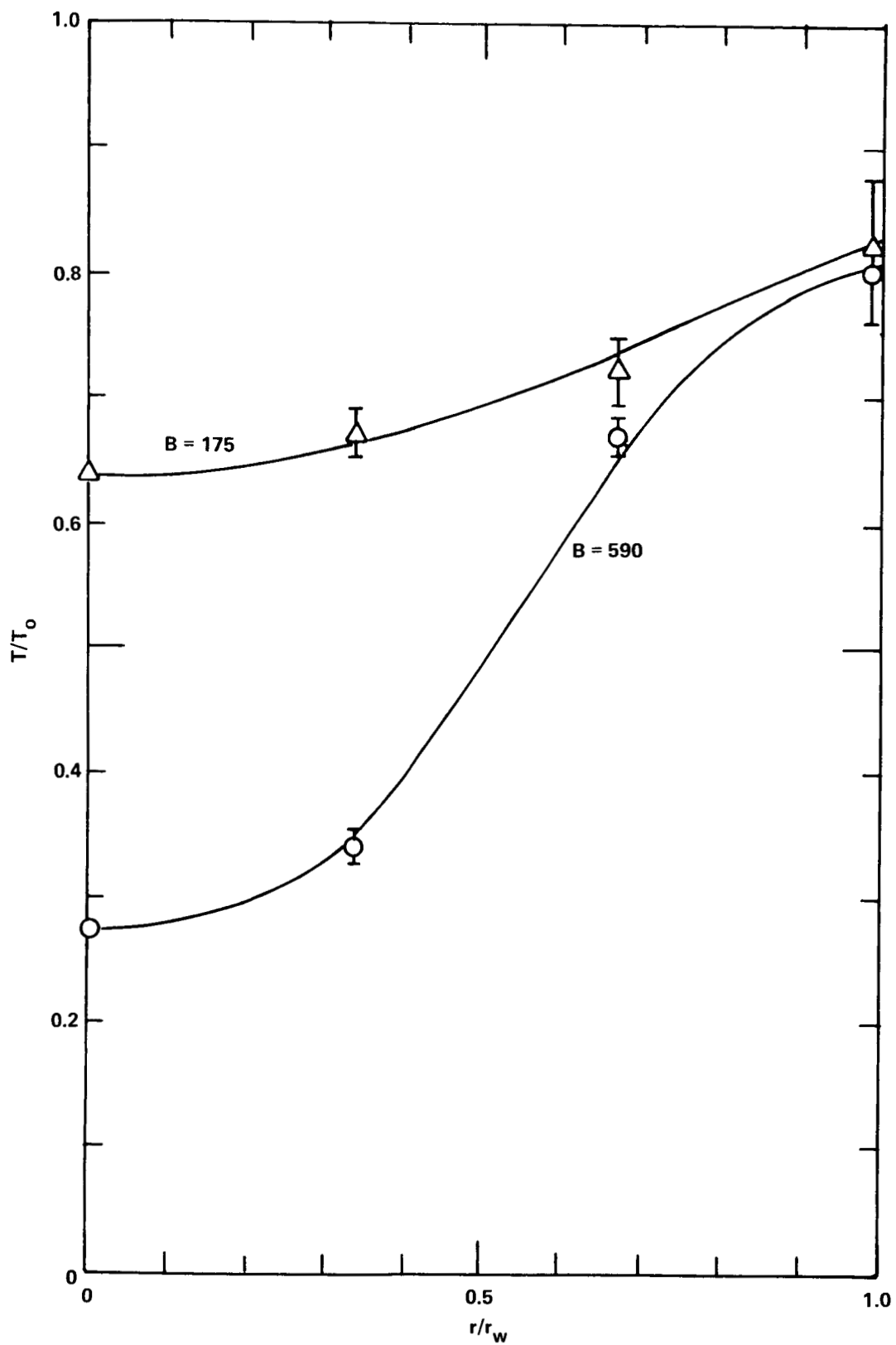


Figure 27 RADIAL TEMPERATURE PROFILES AT  $z/r_* = 13.7$  FOR TWO DIFFERENT REYNOLDS NUMBERS ( $p_0/p_\infty \approx 300$ )

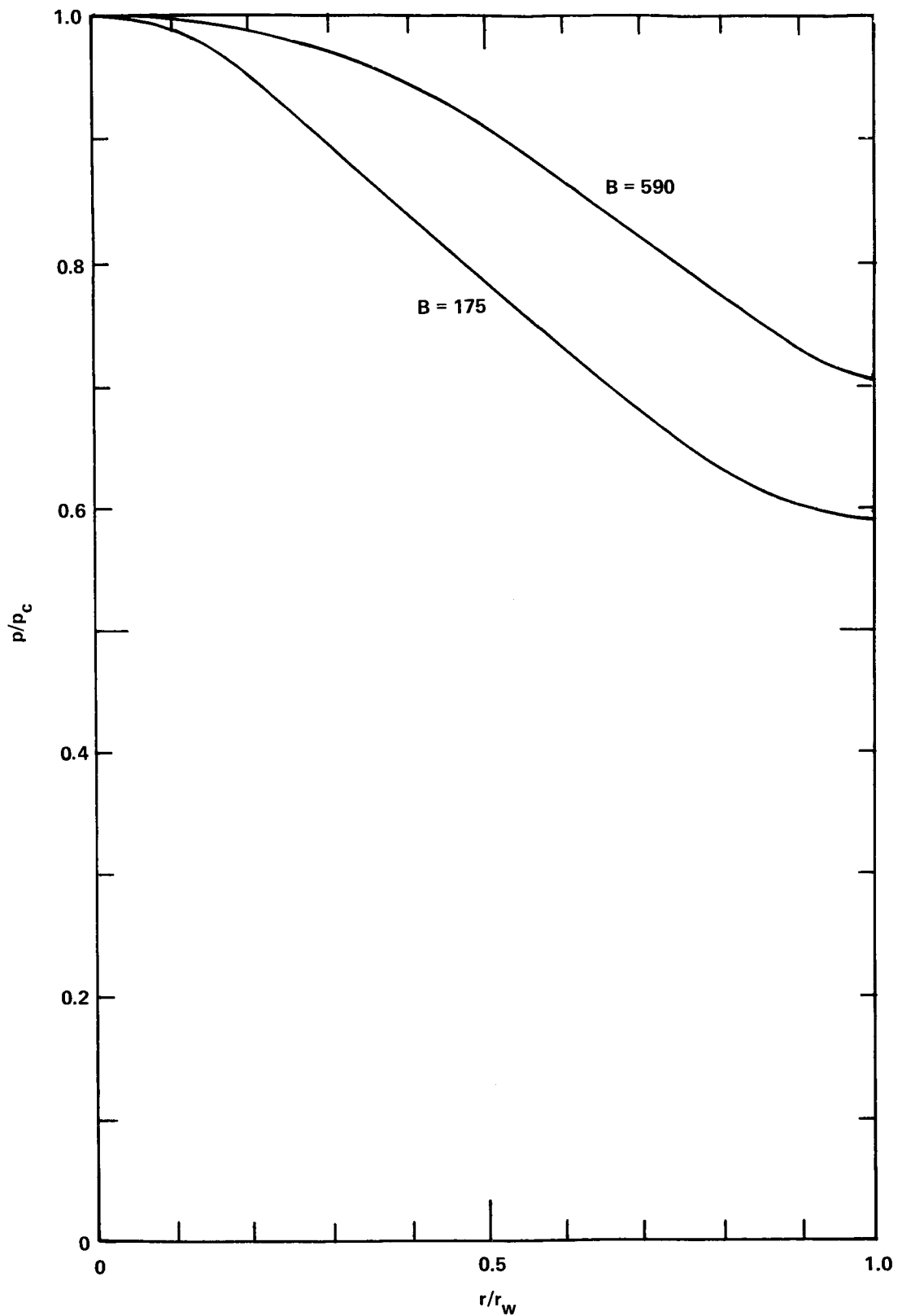


Figure 28 EXPERIMENTAL RADIAL PRESSURE PROFILES AT  $z/r_* = 13.7$  FOR TWO DIFFERENT REYNOLDS NUMBERS ( $p_0/p_\infty \approx 300$ ) \*



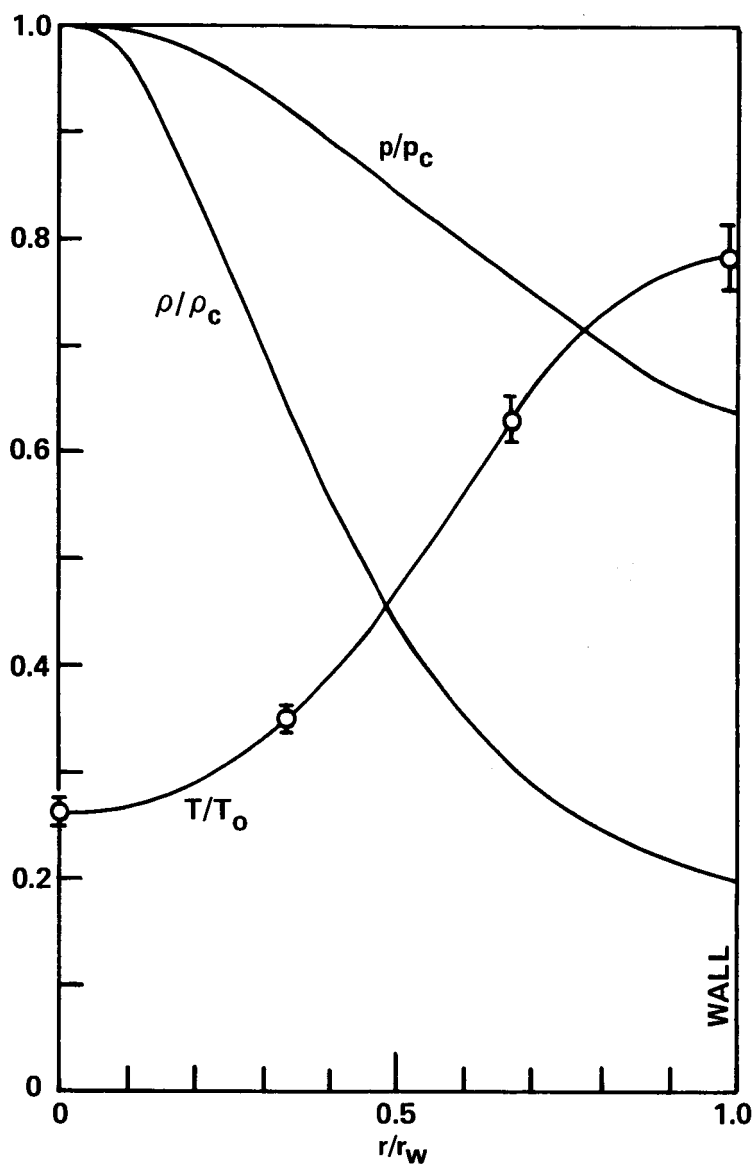


Figure 29 EXPERIMENTAL VARIATION OF  
NORMALIZED TEMPERATURE,  
DENSITY AND PRESSURE WITH  
RADIAL DISTANCE NEAR NOZZLE  
EXIT ( $z/r_* = 18.7$ ).  $B = 590$ ,  
 $p_0/p_\infty = 310$

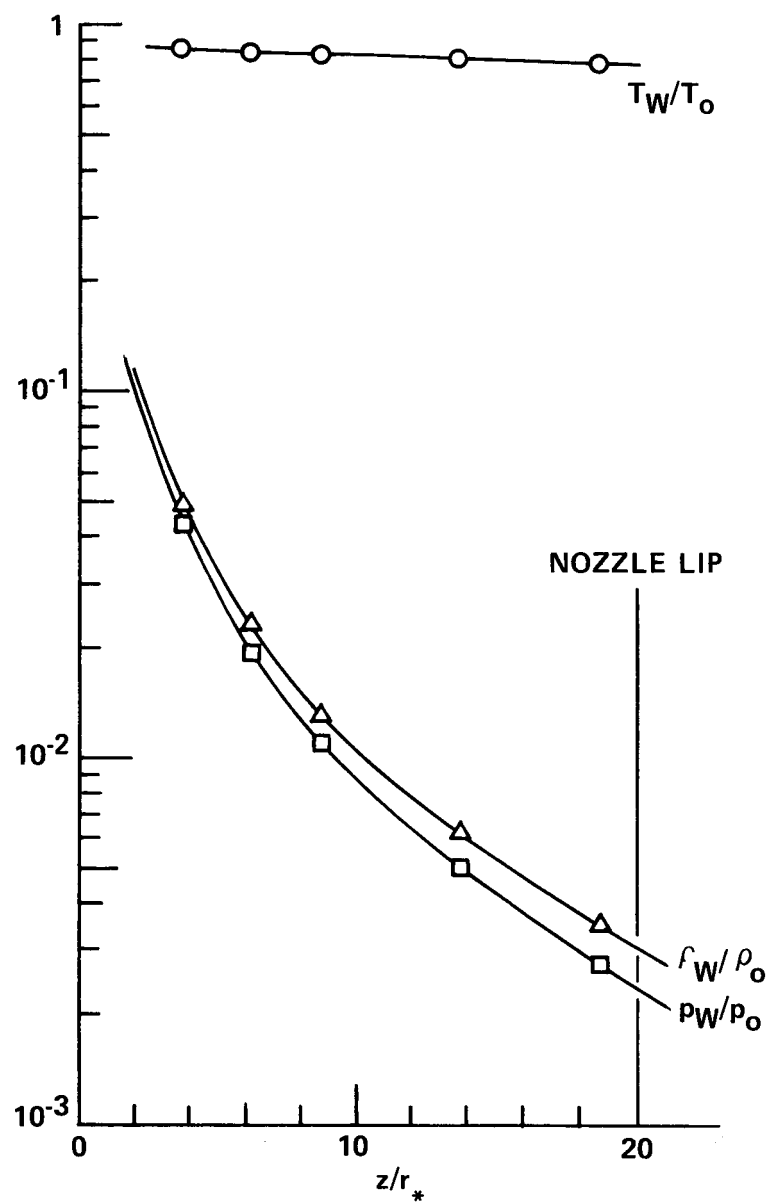
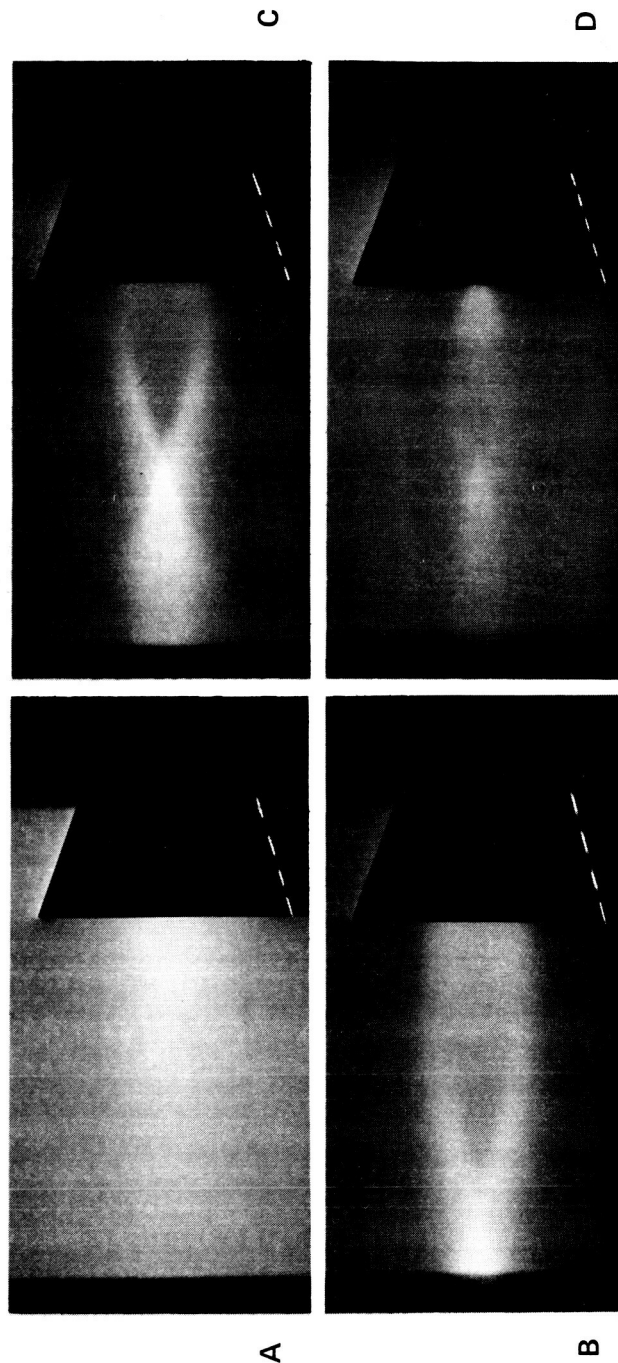


Figure 30 GAS PROPERTIES ALONG NOZZLE WALL FOR  $B = 590$ ,  $p_0/p_\infty = 310$



(A)  $B = 450, p_0/p_\infty = 310$   
 (B)  $B = 1550, p_0/p_\infty = 325$   
 (C)  $B = 1550, p_0/p_\infty = 185$   
 (D)  $B = 1550, p_0/p_\infty = 55$

Figure 31 FLOW-VISUALIZATION PHOTOGRAPHS  
 SHOWING FLOW SEPARATION AT LOW  
 $p_0/p_\infty$  (HIGH AMBIENT PRESSURE)

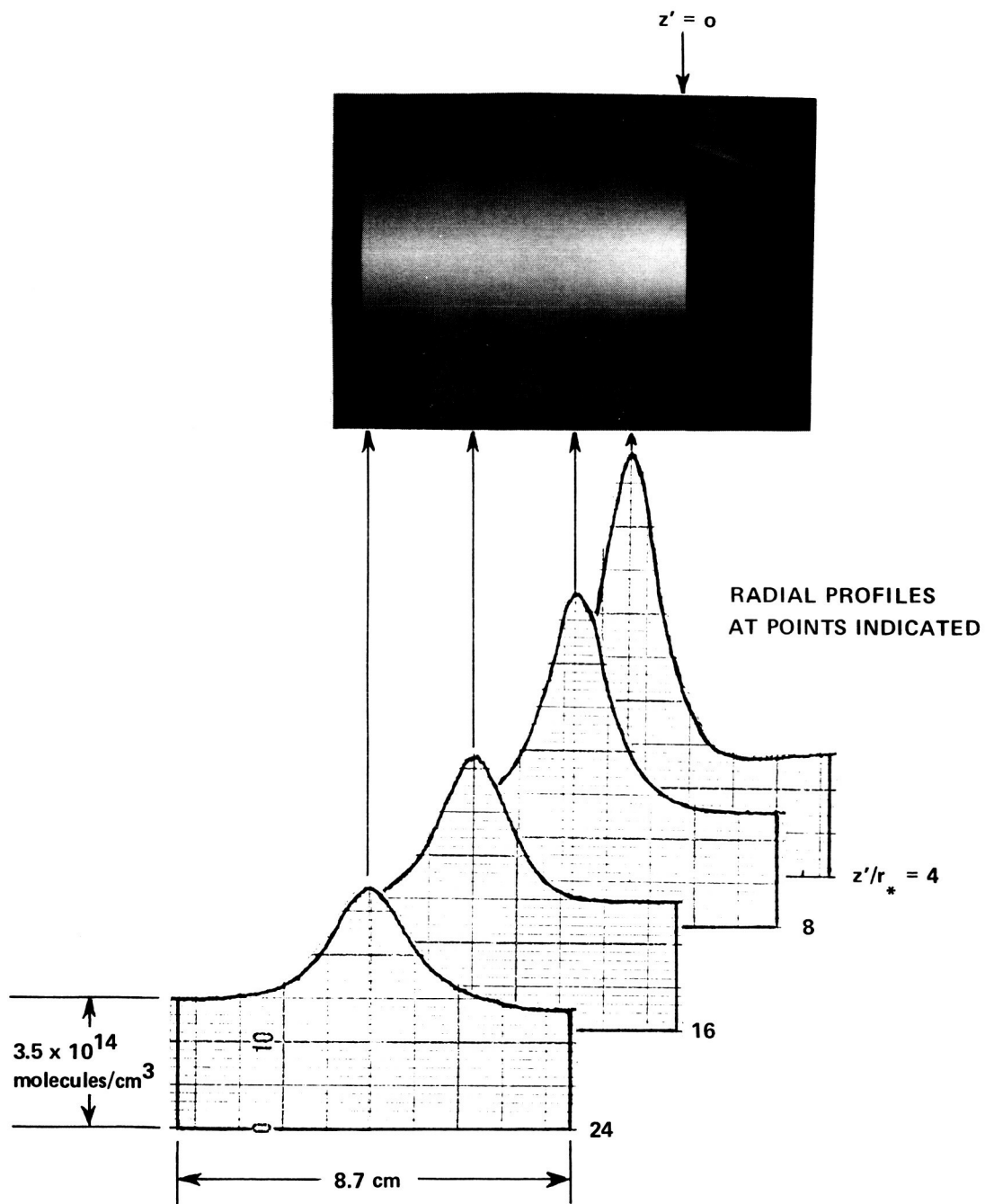


Figure 32 DENSITY PROFILES IN PLUME OF 5 mm NOZZLE FOR  $B = 590$   
AND  $p_0/p_\infty = 310$  ( $p_\infty = 11 \mu \text{ Hg}$ )

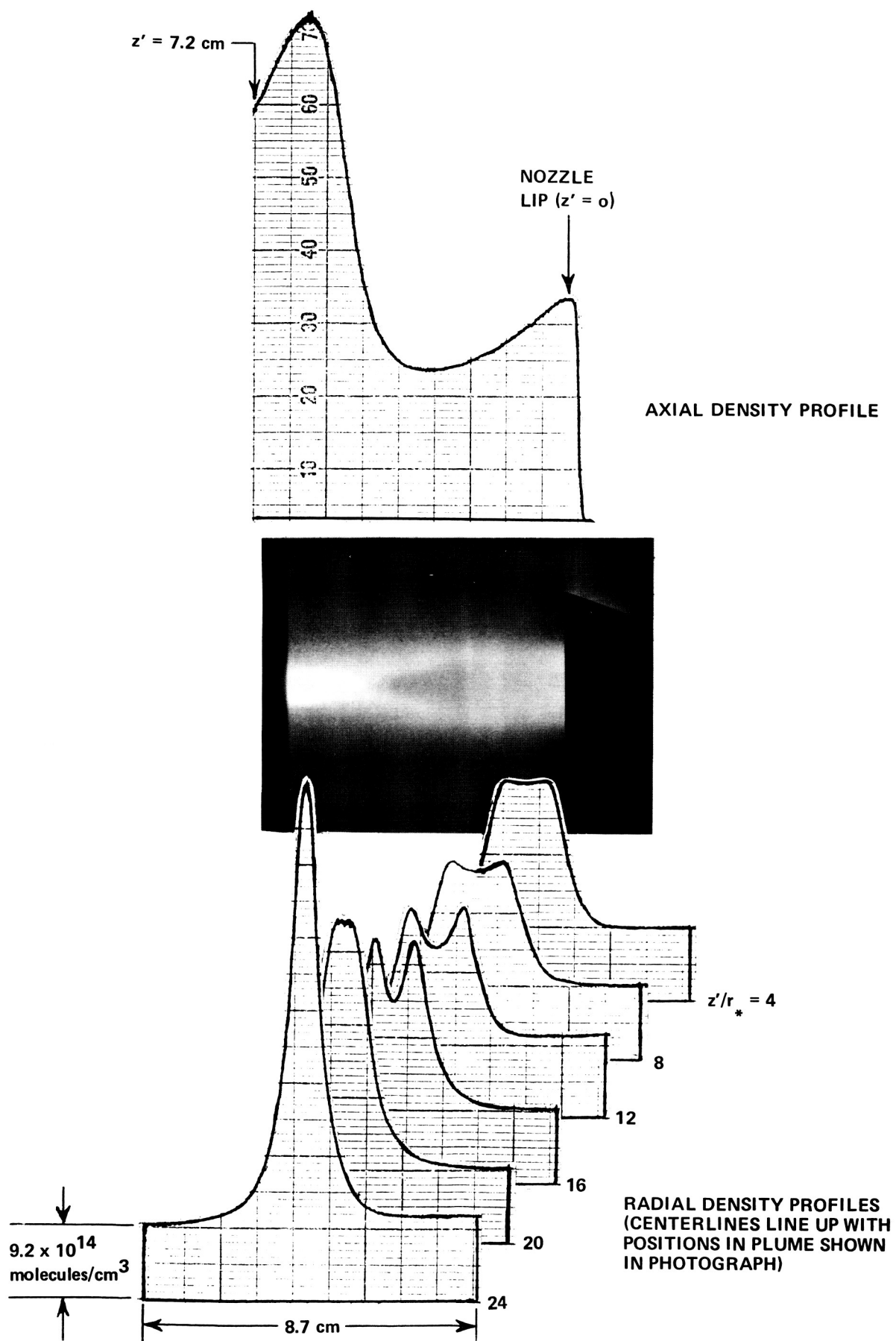


Figure 33 DENSITY PROFILES IN PLUME OF 5 mm NOZZLE FOR  $B = 1550$   
AND  $p_0/p_\infty = 325$  ( $p_\infty = 28.5 \mu \text{ Hg}$ )

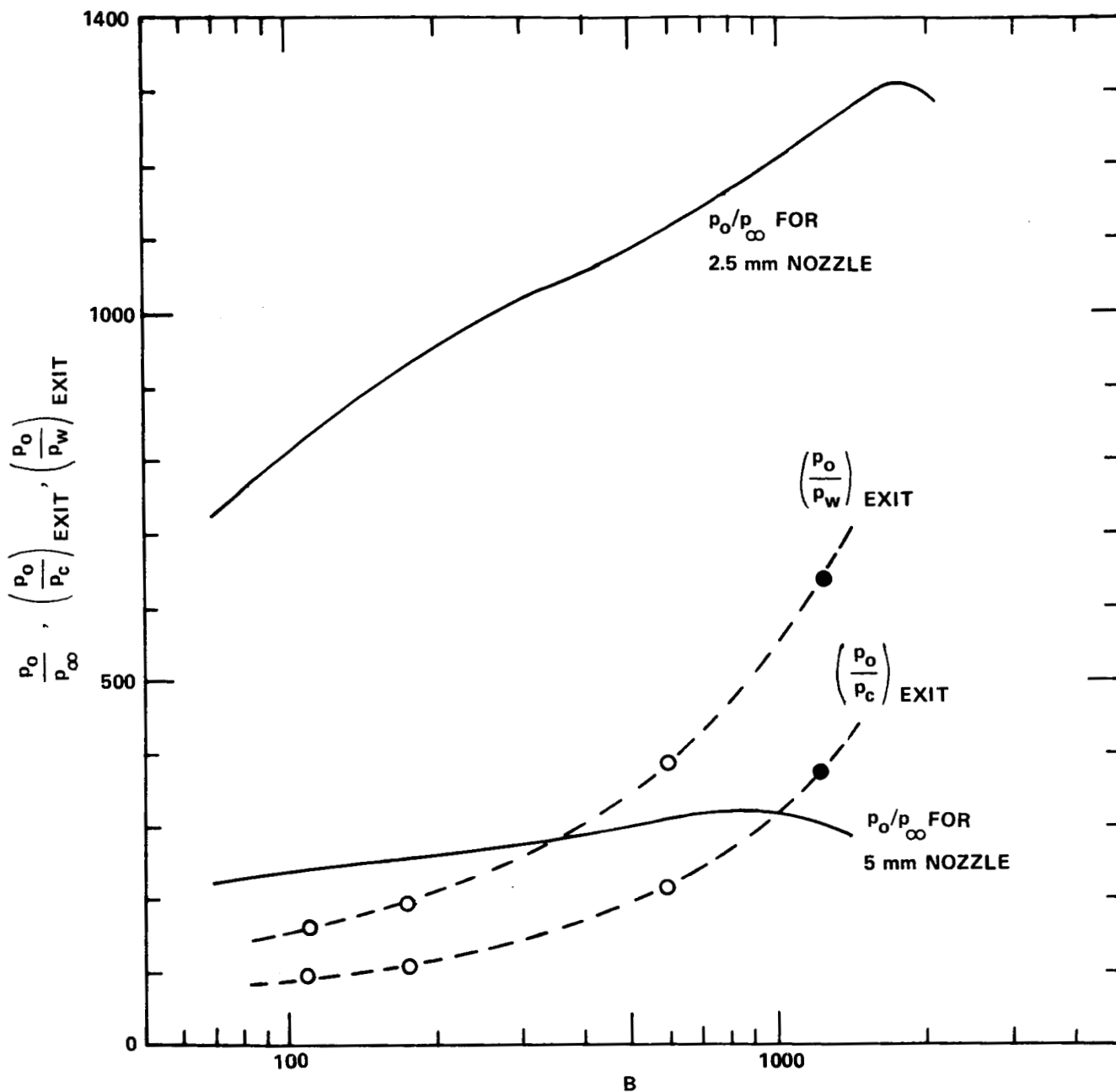
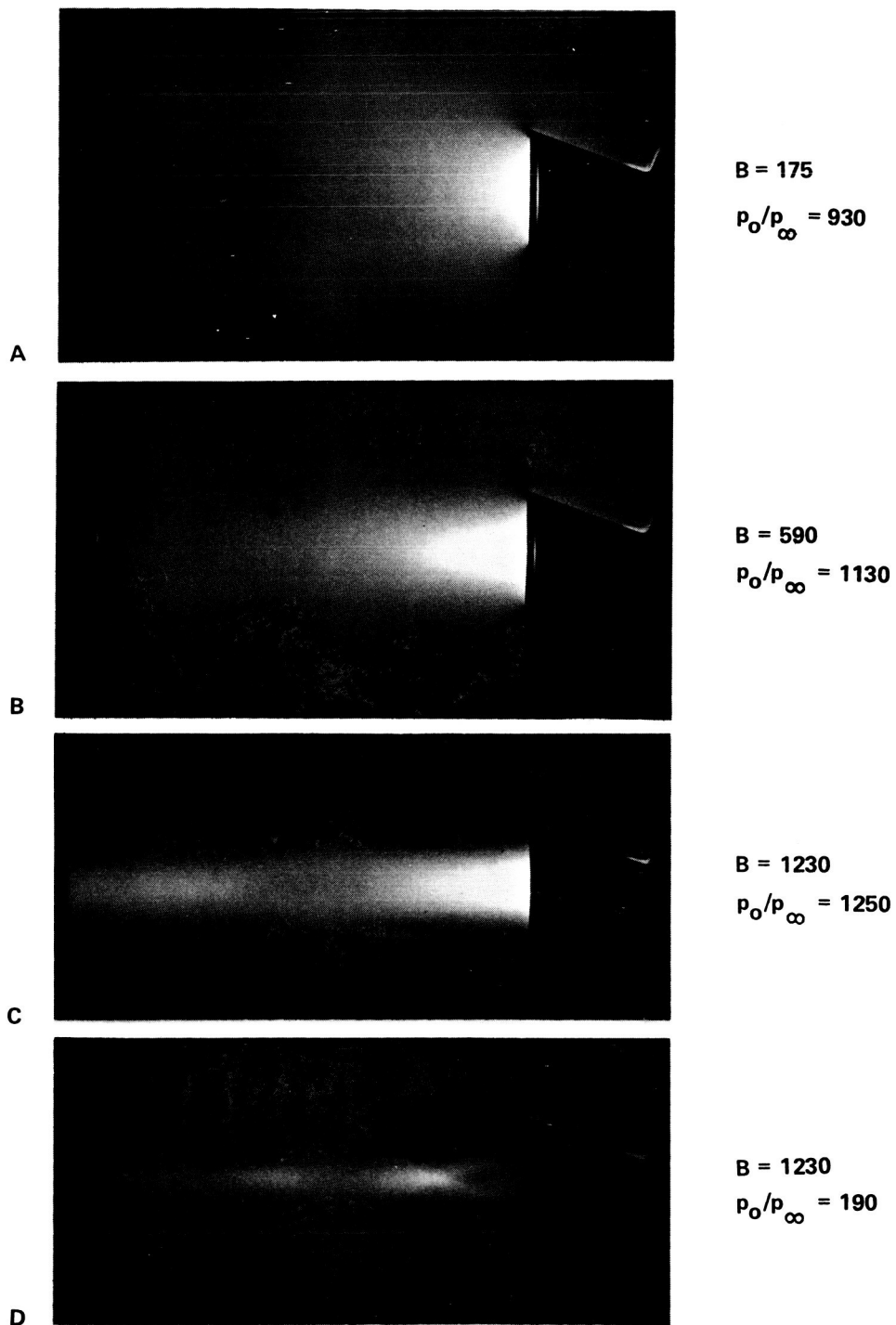
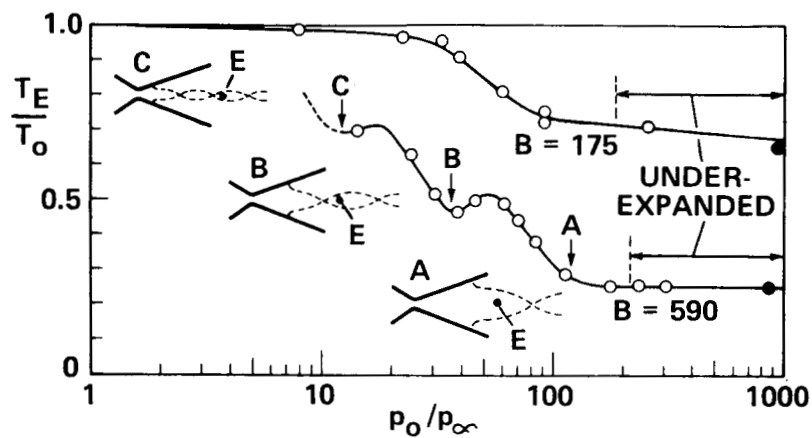


Figure 34 MAXIMUM NOZZLE PRESSURE RATIOS FOR THE TWO NOZZLES AS A FUNCTION OF REYNOLDS NUMBER, ALSO EXPERIMENTAL INTERNAL PRESSURE RATIOS  $(p_o/p_w)_{EXIT}$  AND  $(p_o/p_c)_{EXIT}$

- 5 mm NOZZLE
- 2.5 mm NOZZLE



**Figure 35** FLOW-VISUALIZATION PHOTOGRAPHS FOR 2.5 mm NOZZLE  
 AT VARIOUS VALUES OF  $B$  AND  $p_0/p_\infty$



**Figure 36** JET TEMPERATURE JUST DOWN-STREAM OF NOZZLE LIP AS A FUNCTION OF AMBIENT PRESSURE ( $p_\infty$ ) (POINT E IS ON AXIS AND  $2r_*$  BEYOND EXIT PLANE)

- 5 mm NOZZLE
- 2.5 mm NOZZLE



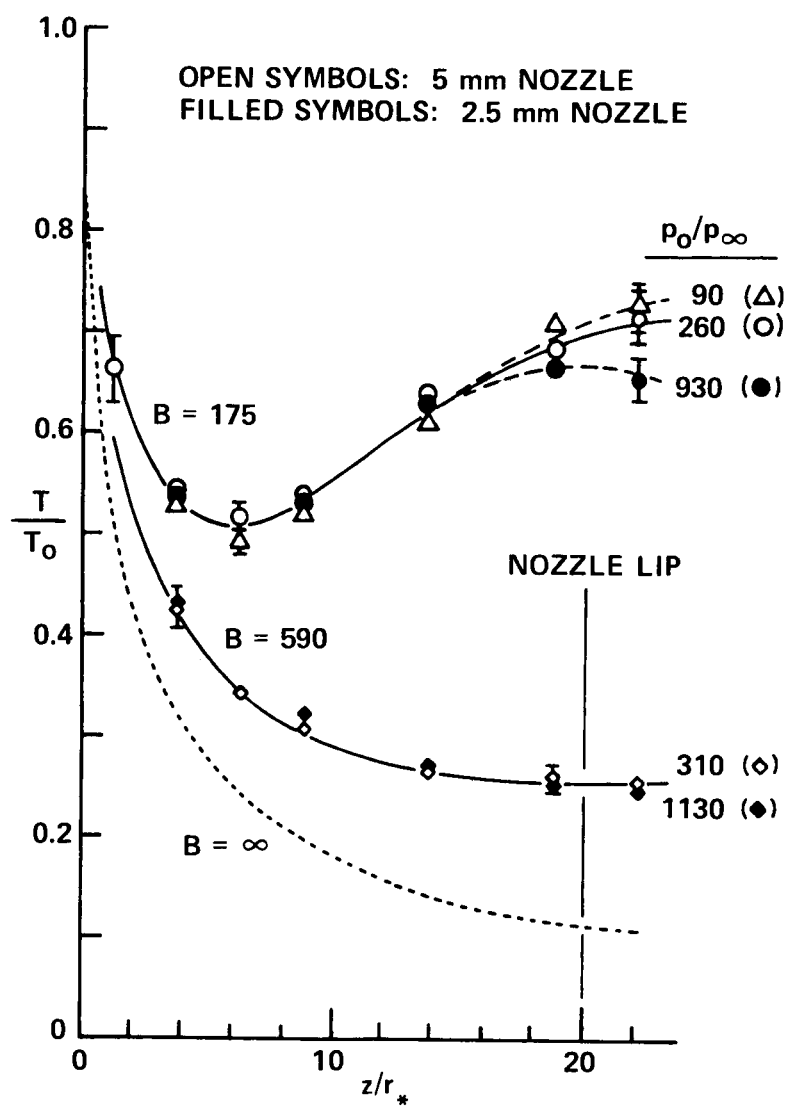


Figure 37 EFFECT OF AMBIENT PRESSURE  
 ON CENTERLINE TEMPERATURES

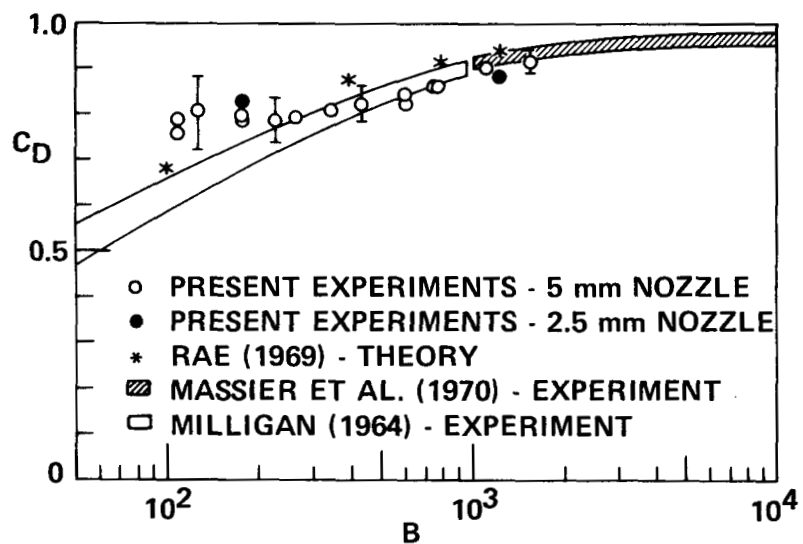


Figure 38 MEASURED DISCHARGE COEFFICIENTS  
COMPARED WITH PREVIOUS DATA -  
SEE ALSO TABLE 2

# DISTRIBUTION LIST

<u>COPIES</u>	<u>RECIPIENT</u>	<u>DESIGNEE</u>
	NASA Headquarters, Washington, D. C. 20546	
1	Contracting Officer, DHC	( )
1	Patent Office,	( )
	NASA Lewis Research Center	
	21000 Brookpark Road, Cleveland, Ohio 44135	
1	Office of Technical Information	( )
1	Contracting Officer	( )
1	Patent Office	( )
	NASA Marshall Space Flight Center	
	Huntsville, Alabama 35812	
2	Office of Technical Information, MS-IP	( )
1	Technical Library	( )
1	Purchasing Office, PR-EC	( )
1	Patent Office, M-PAT	( )
1	Keith Chandler, R-P&VE-PA	( )
1	Technology Utilization Office MS-T	( )
	NASA Pasadena Office	
	4800 Oak Grove Drive	
	Pasadena, California 91103	
1	Patents and Contracts Management	( )
	Western Support Office	
	150 Pico Boulevard	
	Santa Monica, California 90406	
1	Office of Technical Information	( )

<u>COPIES</u>	<u>RECIPIENT</u>	<u>DESIGNEE</u>
1	Technical Monitor	( )
4	Chief, Liquid Propulsion Technology Code: RPL Office of Advanced Research & Technology NASA Headquarters Washington, D. C. 20546	(X)
25	NASA Scientific and Technical Information Facility P.O. Box 33 College Park, Maryland 20740	(X)
1	Mr. Vincent L. Johnson Director, Launch Vehicles and Propulsion Office of Space Science and Applications NASA Headquarters Washington, D. C. 20546	(X)
1	Mr. George S. Trimble Director, Advanced Manned Missions Code: MT Office of Manned Space Flight NASA Headquarters Washington, D. C. 20546	(X)
1	Mr. A. Gessow Chief, Physics of Fluids Branch Office of Advanced Research and Technology NASA Headquarters Washington, D. C. 20546	(X)
1	Mr. Leonard Roberts Mission Analysis Division NASA Ames Research Center Moffett Field, California 24035	(X)

NASA FIELD CENTERS

<u>COPIES</u>	<u>RECIPIENT</u>	<u>DESIGNEE</u>
2	Ames Research Center Moffett Field, California 94035	H. J. Allen Mission Anal. Division
2	Goddard Space Flight Center Greenbelt, Maryland 20771	Merland L. Moseson Code: 620
2	Jet Propulsion Laboratory California Institute of Tech. 4800 Oak Grove Drive Pasadena, California 91103	Henry Burlage, Jr. J. H. Rupe
2	Langley Research Center Langley Station Hampton, Virginia 23365	Dr. Floyd Thompson Director
2	Lewis Research Center 21000 Brookpark Road Cleveland, Ohio 44135	Dr. A. Silverstein Director R. J. Priem E. W. Conrad
2	Marshall Space Flight Center Huntsville, Alabama 35812	Hans G. Paul R. J. Richmond
2	Manned Spacecraft Center Houston, Texas 77058	Dr. Robert R. Gilruth Director J. G. Thibodaux
1	Western Support Office 150 Pico Boulevard Santa Monica, California 90406	Robert W. Kamm Director
2	John F. Kennedy Space Center, NASA Kennedy Space Center, Florida 32899	Dr. Kurt H. Debus Director

# GOVERNMENT INSTALLATIONS

<u>COPIES</u>	<u>RECIPIENT</u>	<u>DESIGNEE</u>
1	Aeronautical System Division Air Force Systems Command Wright-Patterson Air Force Base Dayton, Ohio 45433	D. L. Schmidt Code: ASRCNC-2
1	Air Force Missile Development Center Holloman Air Force Base New Mexico	Maj. R.E. Bracken Code: MDGRT
1	Air Force Missile Test Center Patrick Air Force Base, Florida	L. J. Ullian
1	Air Force Systems Division Air Force Unit Post Office Los Angeles 45, California	Col. Clark Technical Data Center
1	Arnold Engineering Development Center Arnold Air Force Station Tullahoma, Tennessee	Dr. H. K. Doetsch
1	Bureau of Naval Weapons Department of the Navy Washington, D. C.	J. Kay RTMS-41
1	Chemistry Research Laboratory Building 450 Wright-Patterson Air Force Base Dayton, Ohio 45433	K. Scheller ARL (ARC)
1	Department of the Navy Office of Naval Research Washington, D. C. 20360	R. O. Jackel Code: 429
1	Headquarters U. S. Air Force Washington, D. C.	Col. C. K. Stambaugh AFRST

GOVERNMENT INSTALLATIONS

<u>COPIES</u>	<u>RECIPIENT</u>	<u>DESIGNEE</u>
1	Headquarters Research and Technology Division Air Force Systems Command Bolling Air Force Base, Washington, D. C. 20332	L. Green, Jr. (RTGS)
1	Picatinny Arsenal Dover, New Jersey 07801	I. Forsten, Chief Liquid Propulsion
1	Air Force Rocket Propulsion Lab. Research and Technology Division Air Force Systems Command Edwards, California 93523	RPRR
1	U. S. Atomic Energy Commission Technical Information Services Box 62 Oak Ridge, Tennessee	A. P. Huber Oak Ridge; Gaseous Diffusion Plant
1	U. S. Army Missile Command Redstone Arsenal Huntsville, Alabama 35808	W. W. Wharton AMSMI-RRK
2	U. S. Naval Ordnance Test Station China Lake, California 93555	E. W. Price D. Couch
1	Air Force Office of Scientific Research Propulsion Division 1400 Wilson Blvd. Arlington, Va. 22209	B. T. Wolfson

CPIA

2	Chemical Propulsion Information Agency Applied Physics Laboratory 8621 Georgia Avenue Silver Spring, Maryland 20910	Neil Safeer T. W. Christian W. G. Berl
---	---	--

## INDUSTRY CONTRACTORS

<u>COPIES</u>	<u>RECIPIENT</u>	<u>DESIGNEE</u>
1	Aerojet-General Corporation P. O. Box 296 Azusa, California 91703	L. F. Kohrs
1	Aerojet-General Corporation P.O. Box 15847 Sacramento, California 95809	R. J. Hefner R. Stiff
1	Aeronautronic Philco Corporation Ford Road Newport Beach, California 92663	D. A. Carrison
1	Aerospace Corporation 2400 East El Segundo Boulevard P.O. Box 95085 Los Angeles, California	O. W. Dykema W. C. Strahle
1	Astrosystems International, Inc. 1275 Bloomfield Avenue Fairfield, New Jersey 07007	A. Mendenhall
1	Atlantic Research Corporation Edsall Road and Shirley Highway Alexandria, Virginia 22314	R. Friedman
1	Beech Aircraft Corporation Boulder Division Box 631 Boulder, Colorado	J.H. Rodgers
1	Bell Aerosystems Company P.O. Box 1 Buffalo, New York 14205	Dr. Kurt Berman
1	Bendix Corporation Bendix Systems Division 3300 Plymouth Road Ann Arbor, Michigan	John M. Brueger



## INDUSTRY CONTRACTORS

<u>COPIES</u>	<u>RECIPIENT</u>	<u>DESIGNEE</u>
1	Boeing Company P.O. Box 3707 Seattle, Washington 98124	J. D. Alexander
1	Chrysler Corporation Missile Division P.O. Box 2628 Detroit, Michigan 48231	John Gates
1	Curtiss-Wright Corporation Wright Aeronautical Division Wood-Ridge, New Jersey 07075	G. Kelley
1	Dartmouth University Hanover, New Hampshire 03755	P. D. McCormack
1	Defense Research Corporation P.O. Box 3587 Santa Barbara, California 93105	B. Gray
1	Douglas Aircraft Company, Inc. Missile and Space Systems Division 3000 Ocean Park Boulevard Santa Monica, California 90406	R. W. Hallett Chief Engineer Advanced Space Tech.
1	Dynamic Science Corporation 1900 Walker Avenue Monrovia, California 91016	Dr. Kliegel R. J. Hoffman
1	Fairchild Hiller Corporation Aircraft Missiles Division Hagerstown, Maryland	J. S. Kerr
1	General Dynamics/Astronautics Library & Information Services Code: 128-00 P.O. Box 1128 San Diego, California 92112	Frank Dore
1	General Electric Company Re-Entry Systems Department 3198 Chestnut Street Philadelphia, Pennsylvania 19101	F. E. Schultz

## INDUSTRY CONTRACTORS

<u>COPIES</u>	<u>RECIPIENT</u>	<u>DESIGNEE</u>
1	General Electric Company Advanced Engine & Technology Dept. Cincinnati, Ohio 45215	D. Suichu
1	Geophysics Corporation of America Technical Division Burlington Road Bedford, Massachusetts 01730	A. C. Toby
1	Georgia Institute of Technology Aerospace School Atlanta, Georgia 30332	B. T. Zinn
1	Grumman Aircraft Engineering Corp. Bethpage, Long Island New York	Joseph Gavin
1	Ling-Temco-Vought Corporation Astronautics P.O. Box 5907 Dallas, Texas 75222	Warren C. Trent
1	Arthur D. Little, Inc. 20 Acorn Park Cambridge, Massachusetts 02140	E. Karl Bastress
1	Lockheed California Company 2555 North Hollywood Way Burbank, California 91503	G. D. Brewer
1	Lockheed Missiles and Space Company Attn: Technical Information Center P.O. Box 504 Sunnyvale, California 94088	Y. C. Lee
1	Lockheed Propulsion Company P.O. Box 111 Redlands, California 92374	H. L. Thackwell
1	The Marquardt Corporation 16555 Saticoy Street Van Nuys, California 91409	W. P. Boardman, Jr.

## INDUSTRY CONTRACTORS

<u>COPIES</u>	<u>RECIPIENT</u>	<u>DESIGNEE</u>
1	Martin Marietta Corporation Baltimore Division Baltimore, Maryland 21203	John Calathes Code: 3214
1	Martin Marietta Corporation Denver Division P.O. Box 179 Denver, Colorado 80201	J. D. Goodlette Code: A-241
1	Massachusetts Institute of Tech. Department of Mechanical Engineering Cambridge, Massachusetts 02139	T. Y. Toong
1	McDonald-Douglas Aircraft Company Astropower Division 2121 Paularino Newport Beach, California 92663	Dr. George Moc Director, Research
1	McDonnell Aircraft Corporation P.O. Box 516 Municipal Airport St. Louis, Missouri 63166	R. A. Herzmark
1	Multi-Tech. Inc. 601 Glenoaks Boulevard San Fernando, California	F. B. Cramer
1	North American Aviation, Inc. Space & Information Systems Div. 12214 Lakewood Boulevard Downey, California 90241	D. Simkin
1	North American Aviation, Inc. ROCKETDYNE 6633 Canoga Avenue Canoga Park, California 91304	E. C. Clinger R. B. Lawhead
1	Northrop Space Laboratories 3401 West Broadway Hawthorne, California	Dr. William Howard
1	The Pennsylvania State University Mechanical Engineering Department 207 Mechanical Engineering Boulevard University Park, Pennsylvania 16802	G. M. Faeth

## INDUSTRY CONTRACTORS

<u>COPIES</u>	<u>RECIPIENT</u>	<u>DESIGNEE</u>
1	Polytechnic Institute of Brooklyn Graduate Center Route 110 Farmingdale, New York	V. D. Agosta
1	Pratt and Whitney Aircraft (United Aircraft Corporation) Florida Research and Development P.O. Box 2691 West Palm Beach, Florida 33402	G. D. Lewis
1	Princeton University Forrestal Research Center Guggenheim Laboratories Princeton, New Jersey 08540	I. Glassman D. T. Harrje
1	Purdue University School of Mechanical Engineering Lafayette, Indiana 47907	J. R. Osborn
1	Ohio State University Department of Aeronautical & Astronautical Engineering Columbus, Ohio 43210	R. Edse
1	Radio Corporation of America Astro-Electronics Division Princeton, New Jersey 08540	S. Fairweather
1	Republic Aviation Corporation Farmingdale, Long Island New York	Dr. William O'Donnell
1	Sacramento State College Engineering Division 60000 J. Street Sacramento, California 95819	F. H. Reardon
1	Space General Corporation 9200 East Flair Avenue El Monte, California 91734	C. E. Roth

INDUSTRY CONTRACTORS

<u>COPIES</u>	<u>RECIPIENT</u>	<u>DESIGNEE</u>
1	Stanford Research Institute 333 Ravenswood Avenue Menlo Park, California 94025	G. Marxman
1	TRW Incorporated TRW Systems Group One Space Park Redondo Beach, California 90278	G. W. Elverum
1	TRW Incorporated TAPCO Division 23555 Euclid Avenue Cleveland, Ohio 44117	P. T. Angeli
1	Thiokol Chemical Corporation Huntsville Division Huntsville, Alabama	John Goodloe
1	Thiokol Chemical Corporation Reaction Motors Division Denville, New Jersey 07832	Arthur Sherman
2	United Aircraft Corporation Research Laboratories 400 Main Street East Hartford, Connecticut 06108	Erle Martin D. H. Utvick
1	United Technology Center 587 Methilda Avenue P.O. Box 358 Sunnyvale, California 94088	R. H. Osborn
1	University of California Department of Chemical Engineering 6161 Etcheverry Hall Berkeley, California 94720	A. K. Oppenheim
1	University of California Department of Mechanical Engineering Thermal Systems Berkeley, California 94720	E. Starkman

# INDUSTRY CONTRACTORS

<u>COPIES</u>	<u>RECIPIENT</u>	<u>DESIGNEE</u>
1	University of Michigan Aerospace Engineering North Campus Ann Arbor, Michigan 48104	J. A. Nicholls
1	University of Southern California Department of Mechanical Engineering University Park Los Angeles, California 90007	M. Gerstein
1	University of Wisconsin Department of Mechanical Engineering 1513 University Avenue Madison, Wisconsin 53705	P. S. Myers
1	Walter Kidde and Company, Inc. Aerospace Operations 567 Main Street Belleville, New Jersey 07109	R. J. Hanville Director Research Engineering
1	Warner-Swasey Company Control Instrument Division 32-16 Downing Street Flushing, New York 11354	R. H. Tourin
1	Rocket Research Corporation 520 South Portland Street Seattle, Washington 98108	Foy McCullough, Jr.
1	Illinois Institute of Technology 3300 S. Federal Street Chicago, Illinois 60616	T. P. Torda
1	Cetec Corporation 188 Whisman Road Mountain View, California	Dr. R. S. Channapragada
1	Technology Incorporated 6461 Edsall Road Alexandria, Virginia 22312	Donald A. Waters
1	Aerospace Division Library Mail Station R3679 Honeywell, Inc. 2600 Ridgway Parkway Minneapolis, Minnesota 55413	Mr. R. E. Michel